DESIGN AND CHARACTERIZATION OF SILICON MICROMECHANICAL RESONATORS

A Doctoral Dissertation
Presented to
The Academic Faculty

By

Gavin Kar-Fai Ho

In Partial Fulfillment
Of the Requirements for the Degree
Doctor of Philosophy in Electrical and Computer Engineering

Georgia Institute of Technology

August, 2008

Copyright © Gavin K. Ho 2008

DESIGN AND CHARACTERIZATION OF SILICON MICROMECHANICAL RESONATORS

Approved by:

Professor Farrokh Ayazi, Advisor
School of Electrical and Computer Engineering
Georgia Institute of Technology

Professor Oliver Brand
School of Electrical and Computer Engineering
Georgia Institute of Technology

Professor David R. Hertling
School of Electrical and Computer Engineering
Georgia Institute of Technology

Professor Paul A. Kohl
School of Chemical and Biomolecular Engineering
Georgia Institute of Technology

Professor Gary S. May
School of Electrical and Computer Engineering
Georgia Institute of Technology

Date Approved: June 24, 2008

DEDICATION

To my parents Wilson and Wendy, grandmother Nancy, and late grandfather T. H.

ACKNOWLEDGEMENTS

First and foremost, I thank my research advisor Professor Farrokh Ayazi, who gave me the opportunity to take on this research.

I thank my committee members, Professor David R. Hertling, Professor Oliver Brand, Professor Paul A Kohl, and Professor Gary S. May, who provided invaluable advice. I am especially grateful for Professor Hertling for his care and attention since my first day on the Georgia Tech campus.

The sponsors and supporters of this research must be acknowledged. This work was funded by Analog Devices, National Semiconductor, ST Microelectronics, NSF and DARPA/MTO through the NMASP program. This work would not be possible without Professor Clark T.-C. Nguyen of University of California at Berkeley and others in the field of resonators and frequency control.

I am grateful for the support from all my friends. Professor Siavash Pourkamali, Dr. Krishnakumar Sundaresan, and Professor Reza Abdolvand were the best teammates in the laboratory. Other colleagues, including Shweta Humad, John Perng, Abhishek Sivapurapu, and researchers from other institutions also contributed to this work. I also thank the people at Analog Devices, Inc. for providing a special opportunity while this dissertation was being completed. Last but not least, I thank my family.

TABLE OF CONTENTS

ACKNOWLEDGEMENTS iv

LIST OF TABLES vii

LIST OF FIGURES viii

NOMENCLATURE xv

SUMMARY iv

CHAPTER 1 INTRODUCTION 1
- 1.1 MOTIVATION AND ORIGIN 3
- 1.2 OSCILLATOR AND RESONATOR SPECIFICATIONS 5
- 1.3 QUALITY FACTORS IN RESONATORS 8
- 1.4 SILICON AS A RESONATOR MATERIAL 9
- 1.5 FABRICATION TECHNOLOGY 11

CHAPTER 2 RESONATOR CHARACTERISTICS 14
- 2.1 FREQUENCY TUNING 15
- 2.2 DEVICE LINEARITY 17
- 2.3 GENERALIZED CAPACITIVE COUPLING 19
- 2.4 FINITE ELEMENT MODELING 20
- 2.5 MANUFACTURABILITY 21
- 2.6 RESONATOR INTERFACING & EXPERIMENTAL SETUP 28

CHAPTER 3 CAPACITIVE VHF SiBARs 31
- 3.1 THIN ISOTROPIC PLATE ANALYSIS 33
- 3.2 THIN SIBARS ‹110› 36
- 3.3 QUARTER-WAVELENGTH-THICK SIBARS ‹110› 38
- 3.4 THICK SIBAR PLATES ‹110› 40
- 3.5 ANALYSIS AND CHARACTERIZATION 41
- 3.6 SECOND- AND HIGHER-ORDER MODES 48

CHAPTER 4 PIEZOELECTRIC LATERAL-MODE RESONATORS 49
- 4.1 FUNDAMENTAL MODE 51
- 4.2 HIGH-ORDER MODES 60

CHAPTER 5 CAPACITIVE TUNABLE HF IBARs 66
- 5.1 BASIC MODELING AND CLASSIFICATION 67
- 5.2 NORMALIZED STIFFNESS 69
- 5.3 MULTI-SECTION IBARS 70
- 5.4 ANALYSIS AND CHARACTERIZATION 71
- 5.5 IBAR DESIGN FOR MANUFACTURABILITY 75

CHAPTER 6 REFERENCE OSCILLATORS 82
6.1 100-MHz TEMPERATURE-CONTROLLED SIBAR OSCILLATOR 83
6.2 6-MHz TEMPERATURE-COMPENSATED IBAR OSCILLATOR 86

CHAPTER 7 CONCLUSIONS AND DISCUSSION 90
7.1 INITIAL FREQUENCY ACCURACY 91
7.2 FUTURE WORK 92

APPENDIX A. RESONATOR CHARACTERISTICS AND MODELING 93
A.1 CAPACITIVE RESONATOR FUNDAMENTALS 93
A.2 TWO-PORT CAPACITIVE RESONATOR 96
A.3 COMPLEX CAPACITIVE COUPLING 97
A.4 ELECTROSTATIC STIFFNESS 99
A.5 CHARACTERIZATION WITH A RESISTIVE DIVIDER TEST SET 100
A.6 RIGID-BODY RESONATOR DFM 102
A.7 FLEXURAL BEAM DFM 103
A.8 IBAR MODELING 106
A.9 IBAR DFM FOR QE AND CE DESIGNS 112
A.10 ELECTROSTATIC TEMPERATURE COMPENSATION 116
A.11 PIEZOELECTRIC RESONATOR MODELING 120

APPENDIX B. SUPPORTING DATA 126
B.1 SIBAR MEASUREMENTS 126
B.2 IBAR MEASUREMENTS 129
B.3 RIGID BODY RESONATORS 136

APPENDIX C. MATERIAL PROPERTIES 138

REFERENCES 139

LIST OF TABLES

Table 1.1 Typical specifications and estimated pricing of quartz oscillators in 2006..........5

Table 1.2 Summary of micromechanical resonator requirements. 6

Table 3.1 Linearity of a 107-MHz 232μm×40μm×20μm SiBAR. 47

Table 4.1 Fundamental-mode CBAR analysis and measurement summary..........55

Table 4.2 Fundamental-mode CBAR linearity data..........59

Table 5.1 6-MHz IBAR specifications. 72

Table 6.1 Specifications for the 103-MHz SiBAR oscillator. 85

Table 6.2 Specifications of the two-chip temperature compensated IBAR oscillator..........89

Table A.1 Summary of 10-MHz process-compensated IBARs..........112

Table C.1 Properties of silicon, Al, Au, and Cr at 298K..........138

Table C.2 Properties of piezoelectric films at 298K..........138

LIST OF FIGURES

Figure 1.1 Micromechanical resonators in the LF band to UHF band. 1

Figure 1.2 Simplified electrical equivalent circuit of a two-port symmetric resonator. 2

Figure 1.3 Quality factor vs. frequency of silicon micromechanical resonators. 2

Figure 1.4 Two-port configuration of a) an in-plane capacitive beam resonator and b) an out-of-plane piezoelectric beam resonator. 4

Figure 1.5 Dependence of single-sideband phase noise on Q and P_R. 7

Figure 1.6 HARPSS-on-SOI process flow for capacitive resonators. 12

Figure 1.7 Piezoelectric-on-SOI fabrication process flow. 13

Figure 2.1 Tuning mechanisms for a) two-port and b) one-port resonators. 15

Figure 2.2 Mapping of a capacitive resonator with complex mode shape into a parallel-plate equivalent. 19

Figure 2.3 Striations, bowing, and scalloping in deep reactive ion etching. 22

Figure 2.4 Design dimensions and resulting geometry from process bias on clamped-free and clamped-clamped beam resonators. 23

Figure 2.5 Clamped-free flexural beam with a generic profile along the length. 25

Figure 2.6 The locus of w_2/w_3 that satisfies the condition of zero frequency-sensitivity on process bias for a clamped-free beam. 26

Figure 2.7 Finite element model of a tapered 10-MHz clamped-free beam resonator. 27

Figure 2.8 Frequency sensitivity of a tapered process-compensated 10-MHz clamped-free beam resonator. 27

Figure 2.9 Experimental Apparatus A: Agilent N4395A with a resistive divider test set for transmission measurements. 28

Figure 3.1 SEM of a 388μm×40μm×20μm two-port fundamental-mode SiBAR with 225-nm gaps fabricated using the HARPSS-on-SOI process. 31

Figure 3.2 Extensional modes for a rectangular isotropic resonator. 33

Figure 3.3 Relative stiffness k_r and normalized frequency of the extensional modes of a thin isotropic plate. 34

Figure 3.4 Mode shape variation of the BE171 mode as aspect ratio varies between 3.5 and 4.8. 35

Figure 3.5 Uniform mode shape in a thin 3D anisotropic SCS plate (AR=3.7, $t = \lambda/10$). 36

Figure 3.6 Relative stiffness k_r and normalized frequency of the extensional modes of a thin ($t=\lambda/10$) SiBAR aligned to ‹110› on the (100) plane. 37

Figure 3.7 Uniform mode shape in a thin 3D anisotropic SCS plate (AR=3.8, $t = \lambda/4$). 38

Figure 3.8 Relative stiffness k_r and normalized frequency of the extensional modes of a thin ($t=\lambda/4$) SiBAR aligned to ‹110 › on the (100) plane.........39

Figure 3.9 Mode shape of a thick SiBAR with all regions in phase. 40

Figure 3.10 Frequency response of a 388μm×40μm×20μm SiBAR with 225-nm gaps showing an unloaded Q of 90000 with V_P=5V and P = 5 torr. 43

Figure 3.11 Frequency response of a 388μm×40μm×20μm SiBAR with 225-nm gaps showing an impedance of 3.3 kΩ and a loaded Q of 66000 with V_P = 25 V and P = 5 torr. 44

Figure 3.12 Measured and theoretical loaded Q of a 388μm×40μm×20μm 103-MHz SiBAR over a V_P range of 3 to 25 V..45

Figure 3.13 Theoretical and measured resistance of a 388μm×40μm×20μm SiBAR with 225-nm gaps at 5 torr pressure over a V_P range of 3 to 25 V. 45

Figure 3.14 Linearity characterization of a 107-MHz SiBAR. 47

Figure 3.15 a) Small-signal charge migration and b) mode shape of a second-order SiBAR resonator..48

Figure 4.1 Piezoelectric-on-silicon lateral bulk acoustic micromechanical resonator...49

Figure 4.2 SEM of a 240μm×40μm fundamental-mode CBAR. 52

Figure 4.3 Frequency response at 15 MHz with P=5torr showing Q≈11700 and a 50 dB peak above feedthrough. 53

Figure 4.4 Simulated mode shape and unidirectional strain for the resonator in the 15-MHz mode. 53

Figure 4.5 Frequency response of the 90-MHz width-extensional mode at 5 torr. 54

Figure 4.6 ANSYS modal analysis results for the width-extensional mode indicating a response in the anchor. 56

Figure 4.7 ANSYS results indicating coupling of the width-extensional mode with a flexural mode (end view). The strain at the top surface is of primarily importance. 56

Figure 4.8 Frequency response from dc to 100 MHz showing greatest transmission from the 90-MHz mode. 57

Figure 4.9 Response of the 15-MHz resonance in vacuum with various drive levels. 58

Figure 4.10 Response of the 90-MHz resonance in low vacuum with various drive levels. 59

Figure 4.11 High-order composite piezoelectric-on-silicon micro-mechanical bulk acoustic resonator. 60

Figure 4.12 Simulated mode shape of a fifth-order ZnO-on-SCS CBAR with a finger pitch of 10 µm. 61

Figure 4.13 SEM of a 90µm×160µm CBAR with L_P=10µm. 61

Figure 4.14 Frequency response of a ninth-order resonator with L_P=10µm at 1 atm. 62

Figure 4.15 Impedance of a ninth-order resonator with L_P=10µm at 1 atm. 63

Figure 4.16 SEM of a 640-MHz CBAR (L=75µm, w=80µm). 64

Figure 4.17 Frequency response of a 640-MHz CBAR with L_P=5µm at 1 atm. 64

Figure 4.18 Frequency response of a thickness mode resonator fabricated on the same substrate as the CBARs. 65

Figure 5.1 The I-shaped bulk acoustic resonator (IBAR) designed for high tunability and high Q, a) undeformed and b) in the desired mode. 66

Figure 5.2 2-DOF mechanical model of an IBAR. 67

Figure 5.3 a) A Q-enhanced IBAR, and b) a compliance-enhanced IBAR. 68

Figure 5.4 Relative compliance limit of CE IBARs with two electrodes to extensional resonators for w_f=[5,10,20,40] μm...69

Figure 5.5 Mode shape of a two-section 6-MHz CE IBAR. 70

Figure 5.6 SEM of a 10-μm thick two-section IBAR with conservative 180-nm gaps fabricated using the HARPSS-on-SOI process. 71

Figure 5.7 Frequency response of the 6-MHz two-section IBAR with V_P=3V and P=0.1torr. 72

Figure 5.8 Measured and theoretical tuning characteristic of the 6-MHz IBAR over a V_P range of 2 to 25 V. 73

Figure 5.9 Measured and theoretical impedance of the 6-MHz IBAR over a V_P range of 2 to 25 V. The dotted line represents the predicted impedance accounting for R_{SS} of 6.2 kΩ...74

Figure 5.10 Measured and theoretical loaded Q of the 6-MHz IBAR over a V_P range of 2 to 25 V. 74

Figure 5.11 Process compensated geometries of a) a 10-MHz QE IBAR and b) a 10-MHz CE IBAR...75

Figure 5.12 The frequency dependence of 10-MHz CE and QE process-compensated IBARs on process bias. 76

Figure 5.13 a) Process bias on a 10-MHz tapered IBAR, and b) the finite element model..77

Figure 5.14 Simulated frequency deviation for [-0.5,0.5] μm process bias on an optimized tapered IBAR. 77

Figure 5.15 SEM of a 10-MHz optimized IBAR patterned with e-beam lithography, d=500nm (SOI thickness is 10 μm).......................................79

Figure 5.16 Typical frequency response of an optimized 10-MHz process-compensated IBAR in low vacuum. 79

Figure 5.17 Measured frequency deviation from the ideal design and designs with skew. The deviation of the mean of each design is 25 ppm. 80

Figure 5.18 Histogram of natural frequency of the process-compensated IBARs. 81

Figure 5.19 Histogram of Q of the process-compensated IBARs in low vacuum (P=5torr). 81

Figure 6.1 System diagram for the open-loop oven-controlled SiBAR oscillator. 83

Figure 6.2 Temperature stability of a 103-MHz temperature-controlled SiBAR oscillator. 84

Figure 6.3 Single-sideband phase noise of a 103-MHz SiBAR oscillator. 85

Figure 6.4 Architecture of the temperature-compensated IBAR oscillator. 86

Figure 6.5 Typical temperature dependence of resonator natural frequency f_n, resonance frequency at minimum V_P, and the desired temperature-compensated characteristic. 87

Figure 6.6 Intrinsic, linearly-compensated, and parabolically-compensated temperature stability for a 6-MHz IBAR oscillator over a range of 100°C. 88

Figure 6.7 Single-sideband phase noise of the 6-MHz IBAR oscillator with a 3-V polarization voltage. 89

Figure A.1 Schematic of a capacitive resonator in two-port operation. 93

Figure A.2 Clamped-free flexural beam with a generic width-profile along the length. 103

Figure A.3 The locus of w_2/w_3 that satisfies the condition of zero-sensitivity of frequency on process bias. 105

Figure A.4 Lumped 2-DOF ¼-model of the one-section IBAR. 107

Figure A.5 Simulated Q versus frequency characteristic for IBARs with flange widths of [10,20,40] μm and flange lengths of [30,50,70,90,120,150] μm. 111

Figure A.6 Comparison between numerical results (solid line) and finite element results (□) for the relative compliance of IBARs with flange widths of [10,20,40] μm and flange lengths of [30,50,70,90,120,150] μm. Values of c_r for the DFM designs are also plotted (x). 111

Figure A.7 a) Dimensional dependency on process bias and b) mode shape from the anisotropic finite element model of a Q-enhanced IBAR. 114

Figure A.8 Simulated f_0 variation of 10-MHz QE and CE IBARs for δ=[-0.5,0.5]µm. 114

Figure A.9 a) Dimensional dependency on process bias and b) mode shape from the anisotropic finite element model of a tapered compliance-enhanced IBAR. 115

Figure A.10 Simplified model of the piezoelectric-on-silicon resonator. R_{pad}, C_{pad}, and C_0 are parasitic elements. C_s are inherent shunt capacitances. 120

Figure A.11 Free body diagram of an infinitesimal section of the resonator perpendicular to the direction of interest. 121

Figure B.1 Q dependence on V_P for several 100-MHz SiBARs in low vacuum. 126

Figure B.2 Measured impedance vs. V_P and resonator width for SiBARs with 225-nm gaps. 126

Figure B.3 Measured and theoretical tuning characteristic of the 103-MHz IBAR with 225-nm gaps over a V_P range of 3 to 25 V. 127

Figure B.4 Center frequency tuning by resistive heating of a SiBAR. 128

Figure B.5 SEM of a 20-µm thick HARPSS-on-SOI 6-MHz 3-section IBAR, d=180nm. 129

Figure B.6 Measured Q of 119000 from the 6-MHz three-section IBAR in vacuum. 129

Figure B.7 Lowest measured impedance of 655 Ω (R_1=218Ω) from the 6-MHz three-section IBAR (V_{Pi}=18V). 130

Figure B.8 Measured impedance and tuning characteristic of the 6-MHz three-section IBAR with 180-nm gaps. 130

Figure B.9 Measured tuning characteristic of IBARs with 270-nm gaps. 131

Figure B.10 Measured impedance dependence on V_P, showing existence of R_{SS} in IBARs. 132

Figure B.11 Measured quality factor dependence on V_P in IBARs. 132

Figure B.12 Tuning characteristic of a 10-MHz IBAR with 65-nm gaps over a voltage range of 1 to 4 V. 133

Figure B.13 SEM of a 20-MHz 10-µm-thick IBAR with 65-nm gaps. 134

Figure B.14 Impedance and tuning of a 20-MHz IBAR with 65-nm gaps. 134

Figure B.15 Highest *Q* measured from a QE IBAR. 135

Figure B.16 SEM of an SOI rigid-body resonator designed for low-power temperature-compensated real-time clock application. 136

Figure B.17 Measured response from a rigid-body parallel-plate resonator in vacuum. 137

NOMENCLATURE

(100)	crystal plane notation
{100}	crystal plane notation, family of equivalent
[100]	crystal direction notation
⟨100⟩	crystal direction notation, family of equivalent
α_L	linear coefficient of thermal expansion
γ_e	fractional frequency dependence on voltage, electrostatic tuning coefficient, [ppm/V^2]
γ_T	fractional frequency dependence on temperature, [ppm/K]
δ	process bias
ε	strain (also S)
ε_0	permittivity of free space, $1/(\mu_0 c^2)$=8.854187×10^{-12} F/m)
ε_r	relative permittivity
ε_{ij}	elastic strain (normal for i=j, shear for $i\neq j$)
ζ	damping ratio
η	electromechanical coupling coefficient, [N/V] or [C/m]
λ	wavelength
ν	Poisson ratio
ρ	electrical resistivity
ρ_e	dopant density
ρ_m	mass density
ρ_{w}	energy density
σ_{ij}	elastic stress (normal for i=j, shear for $i\neq j$)
τ_{i}	motional time constant, intrinsic to material
ω	angular frequency, see f
A_e	electrode area
A_V	transmission magnitude
C_0	capacitance parallel to the motional arm in the electrical equivalent circuit for a resonator
C_1	motional capacitance in the electrical equivalent circuit for a mechanical resonator
C_{ij}	elasticity coefficients
c_n	dynamic mechanical damping in mode n
c_r	relative dynamic compliance
d_{ij}	piezoelectric strain coefficient [C/N]
e_{ij}	piezoelectric stress coefficient
E	electric field intensity
E, E_i	elastic modulus (Young's modulus)
f	frequency
f_0, ω_0	oscillator or resonators center frequency
$f_{3\mathrm{dB}}$	3-dB bandwidth
Δf_e	frequency shift caused by electrostatic tuning
f_L	Leeson frequency
f_m, ω_m	modulation frequency
f_n, ω_n	mechanical natural frequency, undamped, mode n
$\Delta f_{n,T}$	shift in natural frequency caused by temperature change
$f_r \neq f_s$	resonance frequency (no imaginary part)
f_s, f_1, ω_s, ω_1	series resonance frequency
F	amplifier noise figure
F_e	electrostatic force
i, I	electrical current
I	area moment of inertia about the neutral axis
j	imaginary number
k_e	electrical stiffness
k_n	dynamic mechanical stiffness in mode n
k_r	relative dynamic stiffness
k_{tot}	total dynamic stiffness
l_e, L_e	electrode length
L	resonator length

L_1 motional inductance in the electrical equivalent circuit for a mechanical resonator
L_P resonator primary length, electrode finger pitch
m_n dynamic mechanical mass in mode *n*
M mass
n mode number
N_e number of electrodes
P pressure
P_1, P_S source (test port) power
P_R absorbed power in resonator
q, Q charge
Q quality factor
Q_L quality factor, loaded
Q_U quality factor, unloaded
Q^{-1}_{matl} energy loss intrinsic to material
Q^{-1}_{supp} energy loss through supports/anchors
Q^{-1}_{TED} energy loss by thermoelastic damping
Q^{-1}_{visc} energy loss by viscous damping
Q^{-1}_{other} energy loss by other phenomena
R_1 motional resistance in the electrical equivalent circuit for a resonator, "motional impedance"
R_L load resistance
R_S source resistance
R_{SS} small signal resistance
s complex frequency
S strain (also ε)
t time
t thickness
T stress (also σ)
T_0, T_{ref} ambient temperature
u mechanical displacement
U energy
U_m resonator displacement
V_{i0} dc potential between electrode *i* and resonator body
V_P dc potential of resonator body
V_{Pi} dc potential between resonator body and electrode *i*
v_a acoustic velocity
w resonator width
w_e piezoelectric resonator electrode width
$W_{\max}$ maximum elastic stored energy
Z electrical impedance
Z_t test impedance (of the device under test)

1D one-dimensional
3D three-dimensional
CBAR composite bulk acoustic resonator
CD critical dimension
CF clamped-free boundary condition
dc direct current
DOF degree of freedom
DFM design for manufacturability
DRIE deep reactive ion etching
FBAR film bulk acoustic resonator
FE finite element
FEA finite element analysis
GBW gain bandwidth
HARPSS high aspect ratio combined poly and single-crystal silicon process
IBAR I-shaped bulk acoustic resonator
OCXO oven-controlled crystal oscillator
PLL phase-locked loop
ppm parts per million
RIE reactive ion etching
SCS single crystal silicon
SEM scanning electron micrograph
SOI silicon on insulator (substrate)
SiBAR silicon bulk acoustic resonator
TC temperature compensation
TCXO temperature compensated crystal oscillator
VCXO voltage-controlled crystal oscillator
XO crystal oscillator
ZnO zinc oxide

Parameters are rms unless otherwise specified. 'pk' designates peak values.

SUMMARY

The need for miniaturized frequency-selective components in electronic systems is clear. The questions are whether and how micro-electro-mechanical systems (MEMS) can satisfy the need. This dissertation aims to address these questions from a scientific perspective. Silicon is the focus of this work, as it can benefit from scaling of the semiconductor industry. Silicon also offers many technical advantages. The characteristics of silicon resonators from 32 kHz to 1 GHz are described. The temperature stability and phase noise of a 6-MHz temperature-compensated oscillator and a 100-MHz temperature-controlled oscillator are reported.

Silicon resonators are discussed in the context of frequency references. Resonator design and characterization, with a focus on quality factor, linearity, and the electrical equivalent circuit, are included. Electrical tuning, electromechanical coupling, finite element modeling, and unexpected findings of these resonators are also described. A manufacturability technique employing batch process compensation is demonstrated.

The significance of this work will be unknown for some time. The frequency control and timing industry is not transparent to many researchers, suppliers, and end-users. The applications and their requirements vary across the gamut. The answer to whether MEMS is beneficial to the industry is a resounding 'Yes!' The aim of this research is to explore the fundamental limitations, provide a foundation for future work, and also paint a clearer picture on how micromechanical resonators can complement alternative technologies.

CHAPTER 1 INTRODUCTION

The objective of this research is to model and characterize silicon micromechanical resonators with potential for microelectronic integration throughout the LF, MF, HF, VHF, and UHF bands (Figure 1.1). The ultimate goal is to enable small-form-factor frequency references and enable new applications. Resonator performance metrics, including the equivalent circuit, quality factor, electrical tunability, linearity, and temperature stability are investigated. The effect of these metrics on oscillator performance is also studied. This work complements the fabrication and interface circuit research of my colleagues in advancing micromechanical resonator technology.

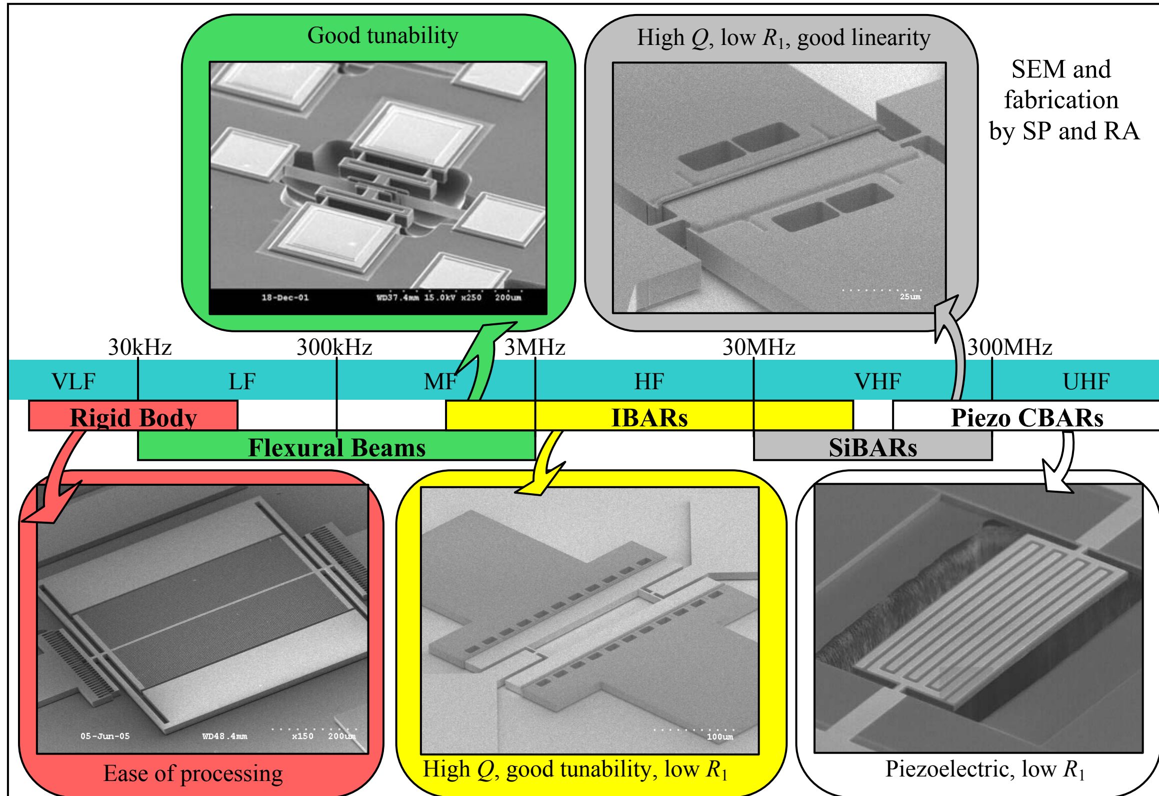

Figure 1.1 Micromechanical resonators in the LF band to UHF band.

Capacitive and piezoelectric silicon resonators are investigated. The majority of devices in this work are two-port and symmetric (Figure 1.2). One important resonator metric is the frequency and quality factor (*f*-*Q*) product. Measured quality factors are plotted over frequency in Figure 1.3. The optimal frequency range and maximum predicted *Q* for each resonator type is identified by the solid lines. The measured *f*-*Q* product of the SiBAR approaches the empirical limit of quartz.

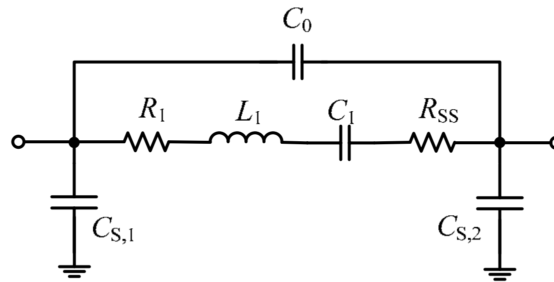

Figure 1.2 Simplified electrical equivalent circuit of a two-port symmetric resonator.

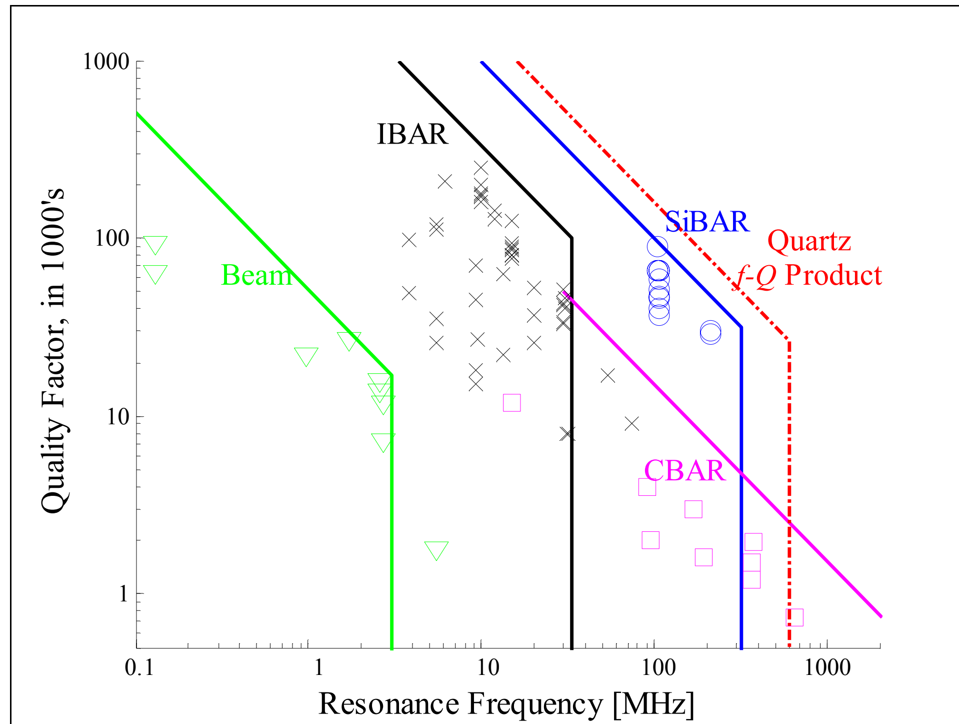

Figure 1.3 Quality factor vs. frequency of silicon micromechanical resonators.

1.1 Motivation and Origin

The frequency reference has eluded the trend of consolidation in silicon for many years.[*] A practical alternative to quartz is sought to enable greater functionality, performance, miniaturization, and efficiency. The alternative is the micromechanical resonator [1-7]. By the end of the 20th century, technologists began to demonstrate that this semiconductor dual of the quartz crystal [8,9] can be practical.

Early demonstrations of microresonators showed great potential and also signs of the challenges ahead. The smaller dimensions reflect into smaller signals to detect. Hopes were high that the new technology would reach beyond the frequency barrier of quartz. However, detecting "micro" responses beyond 1 MHz was challenging at the time.[†] For this reason, interfacing to microresonators is a major accomplishment. The performance was also inferior to the incumbent. Whereas high-quality quartz has a Q greater than 1×10^7 at 1 MHz, microresonators before the new millennia rarely had Q greater than 1×10^4. The mechanisms limiting the quality factor were not well understood.

The field was very exciting when this research began in 2001. There were many unknowns – the most motivating was unawareness of the limitations. The bottleneck was and continues to be process technology. Surface-micromachined polysilicon comb drives [5,6] and beam resonators were the norm in the early years. See Figure 1.4a. These capacitive resonators require polarization between the resonator and the electrode. Trench etching in bulk silicon was popularized when anisotropic plasma reactive ion etching (RIE) technologies were developed [10,11]. It was soon realized that resonators

---

[*] Here "silicon" refers to processing on a semiconductor-standard substrate.
[†] Some reported devices were observed with interferometric and unconventional means.

beyond 100 kHz required parallel-plate transduction [12] and gaps smaller than 1 μm [13,14]. One technology that embraces bulk silicon etching and enables sub-micrometer gaps is the high aspect ratio combined poly and single-crystal silicon (HARPSS) process [15]. Common criticisms of early capacitive resonators were the high device impedance and high polarization voltages (V_P) necessary for operation.

Piezoelectric micromechanical resonators (Figure 1.4b) are similar in structure to quartz crystal resonators. The difference is in thin-film deposition to create the piezoelectric stack.[‡] The challenge in micro-scale piezoelectrics is the deposition of a quality zinc oxide, aluminum nitride, or lead zirconium titanate film.[§] Since the electromechanical coupling from these materials is inherently greater than capacitive transduction, signals are larger and easier to detect. An additional advantage is that V_P is not necessary for piezoelectrics. However, the multi-layer structure may limit the quality factor to several thousand [16].

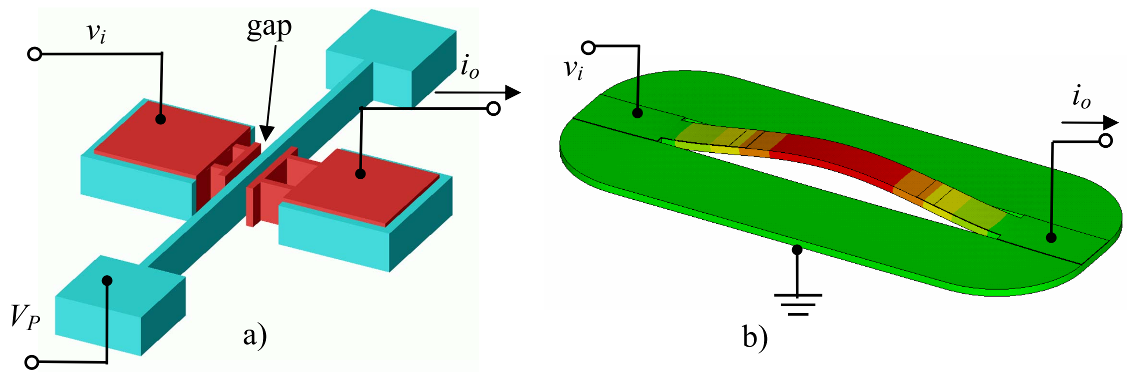

Figure 1.4 Two-port configuration of a) an in-plane capacitive beam resonator and b) an out-of-plane piezoelectric beam resonator.

[‡] The stack consists of a piezoelectric film between two conductive layers
[§] The emerging wireless handset market spurred strong research in film bulk acoustic resonators, which also comprise of a piezoelectric stack.

1.2 Oscillator and Resonator Specifications

Although reference oscillator specifications have many metrics, oscillators can generally be classified by their temperature stability. The specifications for typical quartz oscillators (XO) are shown in Table 1.1. Standard temperature-stable** XOs have 50 ppm or better stability over temperature. Temperature-compensation by frequency "pulling" enables TCXOs with 1 ppm stability. Other specifications include initial frequency accuracy, phase noise, long-term stability, and tuning range. For use in mobile applications, low power consumption and small package size are especially desirable.

Any emerging technology must enable similar specifications (Table 1.2). First and foremost, device impedances (R_1) in the range of mega-Ohms must be overcome for functionality. Reduction of V_P is desirable††. Since long-term stability is critical, material quality and encapsulation are paramount. The resonator must be temperature-stable or allow tuning for compensation. A means to manufacture a repeatable center frequency is necessary. A low R_1 is also desirable for lower power consumption.

Table 1.1 Typical specifications and estimated pricing of quartz oscillators in 2006.

	XO	VCXO	TCXO	OCXO
Frequency [MHz]	0.03-100	1-100	10-50	10-50
Frequency Accuracy and Temp. Stability, 125°C [ppm]	50	50	1-5	0.1
Tuning [ppm]	-	±100	-	-
Power [mW]	0.001-50	5-50	5-50	$1000\text{-}10^4$
Size [mm×mm]	3.2 x 2.5	3.2 x 2.5	3.2 x 2.5	20 x 20
Cost	$0.05-0.50	$0.50	$0.80	$10-50

** Temperature-stable quartz consists of the AT-, BT-, and SC-cuts.
†† Although high-voltage technologies (generating up to 100 V) are available, they are a specialty rather than a standard.

Table 1.2 Summary of micromechanical resonator requirements.

Oscillator Specification	Resonator Requirement
Frequency accuracy	Repeatable f_0, fine tuning or trimming
Temperature stability	Temperature stable, fine tuning for compensation
Phase noise	High Q, good linearity, low sensitivity to external excitation
Power consumption	Low R_1
Long-term stability	Material quality, reliable packaging
Voltage control	Fine electrical tuning

The phase noise determines the quality of the oscillator. With a slight modification to Leeson's model [17], the single-sideband phase noise can be expressed as [18,19]

$$L = \left[1 + \left(\frac{f_0}{2Q_L}\right)^2 \frac{1}{f_m^{\ 2}}\right]\left[b_1 f_m^{\ -1} + \frac{Fk_BT}{P_R}\right] \tag{1.1}$$

where f_0 is the carrier (center) frequency, f_m is the modulation frequency, F is the noise figure of the amplifier, k_BT is the thermal noise (-174 dBm/Hz), Q_L is the loaded Q of the feedback resonator, and P_R is the signal power at the input of amplifier. The typical phase noise obtained using a high-Q resonator in feedback is illustrated in Figure 1.5. Greater linearity in the resonator enables a lower noise floor. High Q is imperative as it reduces the Leeson frequency, given by

$$f_L = \frac{f_0}{2Q_L}, \tag{1.2}$$

and enables low close-to-carrier noise.

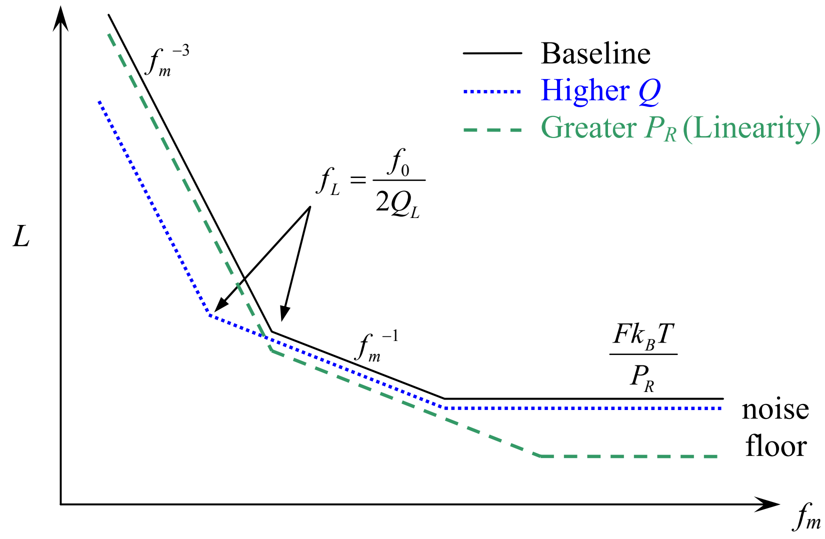

Figure 1.5 Dependence of single-sideband phase noise on Q and P_R.

1.3 Quality Factors in Resonators

The unloaded quality factor Q_U of a resonator is a metric of its frequency stability. Q_U of a mechanical resonator is determined by number of dissipation mechanisms.

$$Q_U = \left(\frac{1}{Q_{matl}} + \frac{1}{Q_{supp}} + \frac{1}{Q_{TED}} + \frac{1}{Q_{visc}} + \frac{1}{Q_{other}} \right)^{-1} \tag{1.3}$$

In (1.3), Q_{matl}^{-1} is attributed to intrinsic losses in the material [20], Q_{supp}^{-1} represents energy loss through the anchor [21-23], Q_{TED}^{-1} is the thermoelastic dissipation [24-27], and Q_{visc}^{-1} is caused by viscous damping [28] and squeeze-film damping [29] of the surrounding medium. Q_{other}^{-1} includes dissipation at material interfaces, losses relating to surface effects, and any other dissipation mechanisms.

For an ideal mechanical resonator, in which the only dissipation is intrinsic (*i.e.*, material dissipation), constancy of frequency-Q product exists [20]. The intrinsic losses can generally be described by a motional time constant τ_i of the material, which defines the intrinsic Q as

$$Q_i = \frac{1}{\omega \tau_i}. \tag{1.4}$$

Generally, τ_i is 1–10^3 femto-seconds for low-loss crystalline materials. For AT-cut quartz at room temperature, τ_i is ~10 fs and the intrinsic f-Q product is 1.6×10^{13}.

Micromechanical resonators are generally susceptible to the aforementioned loss mechanisms [30-32] more than their macroscopic counterparts. The increased surface-to-volume ratio of the resonators increases their sensitivity to surface-related dissipation, such as viscous damping and adsorption-desorption [33]. A high-Q resonator requires a balance of material selection, process, encapsulation, and design.

1.4 Silicon as a Resonator Material

Single-crystal silicon (SCS) is attractive as a structural material since it is well characterized, its material quality is tightly controlled, it is intrinsically low-loss, and the crystalline nature has potential for excellent linearity. Capacitive resonators formed in SCS can be monolithic (*i.e.*, not a composite of materials). They have potential to meet the tightest aging specification for any mechanical device. Furthermore, it will be shown that capacitive resonators fabricated from SOI substrates have higher performance than those fabricated from deposited thin-films. The primary challenge in using silicon, however, is the temperature dependence of its elastic properties.

The natural frequency of a resonator can be expressed as

$$f_n = \frac{A_n}{L_{gen}} v_a \tag{1.5}$$

in which L_{gen} is a generalized frequency-defining dimension, A_n is a dimensionless parameter, and v_a is the acoustic velocity of the mode. Defining γ_T as the fractional frequency dependence on temperature,

$$\gamma_T \equiv \frac{1}{f_n}\frac{\partial f_n}{\partial T} = -\alpha_L + \frac{1}{v_a}\frac{dv_a}{dT} \tag{1.6}$$

in which α_L is the linear thermal expansion coefficient. Quartz is unique in that α_L and $\frac{1}{v_a}\frac{dv_a}{dT}$ have equal values at certain temperatures depending on directionality [8].[‡‡] In other materials, however, the effect of temperature change must be compensated to provide a stable f_n.

[‡‡] The stability for temperature-compensated cuts can be as good as 20 ppm over 125°C.

For a one-dimensional (1D) approximation, $v_a = (E_i \rho_m^{-1})^{0.5}$, where E_i is the elastic modulus in direction i, and ρ_m is the mass density. By defining α_E as the temperature dependence of the elastic modulus, γ_T simplifies to[§§]

$$\gamma_T = \frac{1}{2}(\alpha_L + \alpha_E). \tag{1.7}$$

The linear thermal expansion coefficient α_L for SCS is temperature-dependent and is 2.3 to 2.6 ppm/K at 300 K [34-36]. α_L increases from 0 ppm/K at 100 K to 3 ppm/K at 400 K. α_E is dependent on the mode, directionality, doping, and temperature and is approximately -60 ppm/K. Therefore, the expected temperature coefficient is -27 to -31 ppm/K for various modes [35,36].

[§§] The fractional mass density dependence on temperature is $-3\alpha_L$. Both α_L and α_E are temperature dependent.

1.5 Fabrication Technology

The fabrication technology is presented to complement discussions on design and characterization. In total, three fabrication technologies were used in this work. All are based on reactive ion etching on silicon-on-insulator (SOI) substrates.[***]

The capacitive resonators presented in this work were fabricated using two fabrication technologies. In the first technology, transduction gaps were defined by deep reactive ion etching (DRIE) of trenches in device silicon [10]. A single lithography can be used to define all necessary features for a functional resonator on SOI. Devices have been patterned using both optical lithography and electron-beam lithography [37]. Removal of buried silicon dioxide (oxide) releases the device.

The majority of capacitive resonators in this work were fabricated using the three-mask HARPSS-on-SOI process [38]. See Figure 1.6. Trenches are etched in the device silicon. Oxidation follows to create a sacrificial oxide liner. The thickness of the oxide defines the gap. Polysilicon is then deposited to fill the trench and create the electrode. Patterning for isolation follows. Devices are finally released by removing the buried oxide and sacrificial oxide. This process is unique in creating very thick silicon devices, up to 100μm thick, with sub-μm gaps. Devices with gaps as small as 65 nm have been fabricated [39].

[***] Although encapsulation and packaging may be the most undervalued element of a micromechanical system, issues relating to these topics are not discussed.

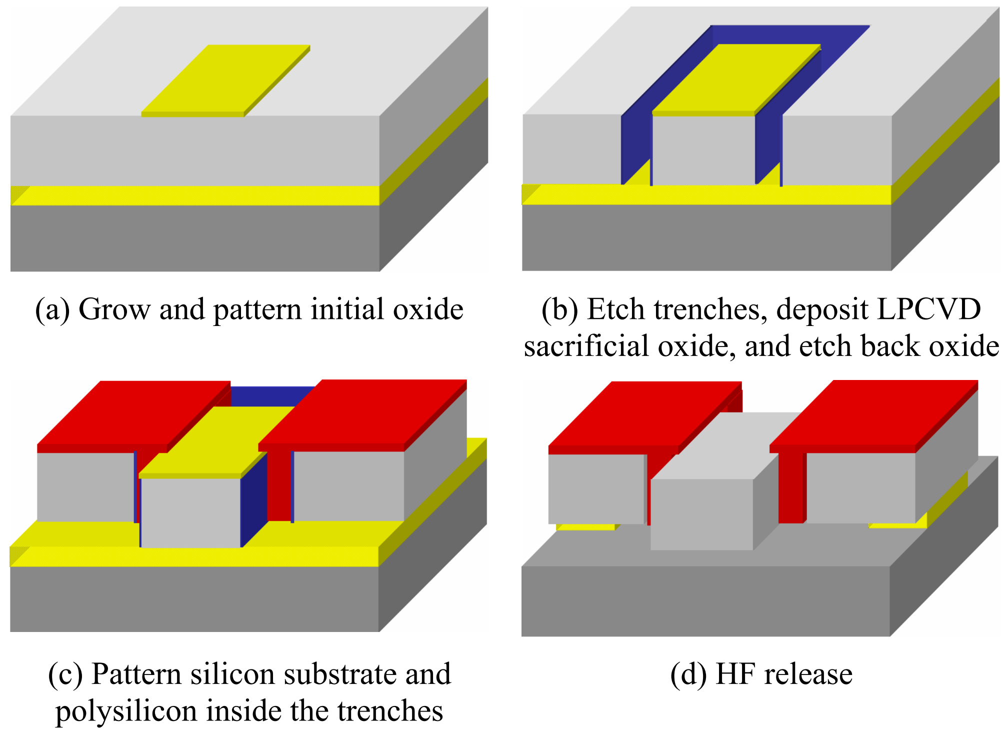

Figure 1.6 HARPSS-on-SOI process flow for capacitive resonators.

Piezoelectric resonators were fabricated using a low-temperature five-mask piezoelectric-on-SOI process [40,41]. See Figure 1.7. A zinc-oxide (ZnO) piezoelectric stack is created on the device silicon (which may be high-resistivity). Typical substrates have a 5-µm thick device layer. Devices are aligned to ‹110›. To create the stack, 100-Å chromium adhesion layer and a 1000-Å gold film are evaporated and patterned. Next, a 0.5-µm thick zinc oxide film is sputtered. The quality of sputtered ZnO on gold-coated silicon was much higher than the quality of ZnO on aluminum or platinum. The full-width half-maximum of the rocking curve was approximately 5°. Next, a 1000-Å aluminum film is evaporated and patterned by liftoff for the top electrode. There are two variations of this process for release. The first calls for backside etching of handle silicon

[40]. The other process requires buried oxide to be removed before creating the piezoelectric stack [41].

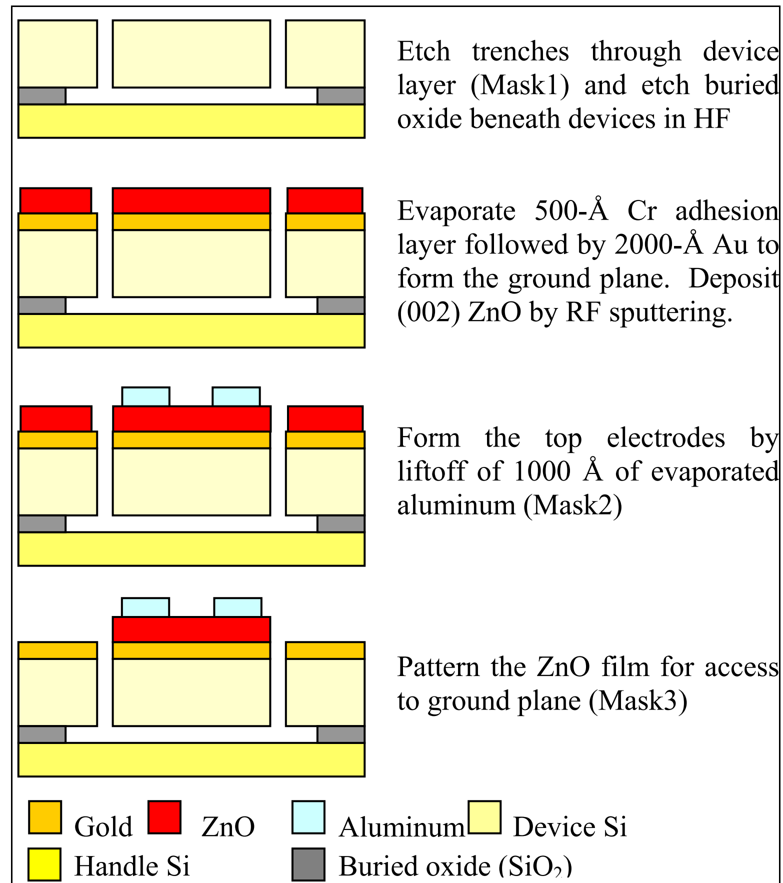

Figure 1.7 Piezoelectric-on-SOI fabrication process flow.

CHAPTER 2 RESONATOR CHARACTERISTICS

Characteristics of capacitive and piezoelectric silicon resonators, their models, and the analysis tools and apparati for their characterization are described. The significance of the normalized dynamic stiffness (k_n/A_e) of a capacitive resonator is presented. A simple numerical technique for capacitive coupling is developed. Voltage-sensitivity of a resonator is described and proposed for tuning. The linearity limits of a resonator are also investigated. The highlight of this chapter is a manufacturability technique for repeatable center frequency.

The investigated resonators are the symmetric two-port variety, for which the simplified electrical equivalent circuit in Figure 1.2 suffices in most scenarios. One should refer to [42] for a complete model of a two-port resonator. This dissertation focuses on designing resonators such that their electrical equivalent circuit containing the RLC elements enables a high-performance oscillator.

$$R_1 = \frac{k_{tot}}{\omega_n Q \eta^2}, \ L_1 = \frac{m_n}{\eta^2}, \ C_1 = \frac{\eta^2}{k_{tot}}, \qquad (2.1,2.2,2.3)$$

In these expressions, k_{tot} is the total dynamic stiffness, m_n is the dynamic mass, ω_n is the angular natural frequency, and η is the coupling coefficient. For a capacitive resonator, the linearized coupling at port i is given by

$$\eta_i = V_{Pi} \frac{\partial C}{\partial u_y} \approx \frac{V_{Pi} \varepsilon A_e}{d^2}. \qquad (2.4)$$

where d is the gap and V_{Pi} is the bias potential between the resonator body and electrode i. Since R_1 is inversely proportional to electrode area A_e, devices formed in thick SOI are superior to devices formed in thin deposited films.

2.1 Frequency Tuning

Electrical tuning is desirable in resonators for trimming and frequency control. Electrical trimming is advantageous over alternative techniques such as material removal processes for its reversible nature and applicability at the end-of-line. Dynamic frequency control is also desirable in voltage-controlled oscillator applications. Increased frequency control, however, typically leads to undesired sensitivity to the control parameter. Since micromechanical resonators are inherently stable, they are most suitable for applications requiring 1% tuning or less.

Two options are available for tuning the operational frequency of a resonator: tuning the elements in the motional arm (Figure 2.1a) and the use of external elements as done traditionally with quartz crystals (Figure 2.1b). It will be shown that C_1 tuning is possible by varying the polarization (bias voltage) on a resonator. The degree to which C_1 can tune the series resonance is explained in depth. Tuning of the parallel resonance by an external C_L is limited to piezoelectric resonators, since C_1 for capacitive resonators is typically less than 1 fF.

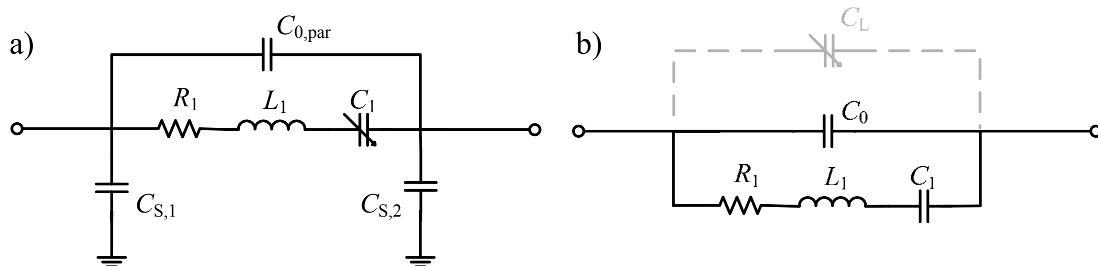

Figure 2.1 Tuning mechanisms for a) two-port and b) one-port resonators

The inherent electrostatic tuning of parallel-plate transduction is one of the attractive features of capacitive resonators. The total dynamic stiffness is given by

$$k_{tot} = k_n + N_e k_e . \tag{2.5}$$

From Appendix A.4, the displacement-linearized k_e from electrode i is given by

$$k_{ei,0} = -\frac{V_{Pi}^{2} \varepsilon A_e}{d^3} . \tag{2.6}$$

For a device with two electrodes, the relationship between the series resonance frequency $f_s = 1/2\pi \cdot (L_1 C_1)^{-1/2}$ and the natural frequency $f_n = 1/2\pi \cdot (k_n/m_n)^{1/2}$ simplifies to

$$\frac{f_s}{f_n} \approx 1 - \frac{\varepsilon A_e}{k_n d^3} V_{Pi}^{2} \tag{2.7}$$

in which $k_{e0} << k_n$ and A_e is the area of one electrode. By varying V_{Pi}, f_s can be tuned. Defining $\Delta f_s \equiv f_s' - f_s$,

$$\frac{\Delta f_s}{f_n} \approx -\frac{\varepsilon A_e}{k_n d^3} \left(V_{Pi}'^{2} - V_{Pi}^{2} \right) \tag{2.8}$$

For tuning and R_1, the normalized stiffness k_n/A_e is of utmost importance rather than k_n or k_{tot}. Since k_n/A_e and gap size vary between designs, the electrostatic tuning coefficient is introduced.

$$\gamma_e \equiv \frac{\Delta f_s}{f_n} \frac{1}{\Delta V_{Pi}^{2}} = -\frac{\varepsilon A_e}{k_n d^3} \quad \left[\mathrm{V}^{-2} \right] \tag{2.9}$$

In defining γ_e, tunability of various resonator topologies can be easily evaluated. The square dependence of Δf_s on V_{Pi} is evident. To increase electrostatic tuning, the gap size and normalized stiffness must be minimized.

2.2 Device Linearity

Optimization of linearity is essential for the noise floor of an oscillator. Linearity is typically represented as an output current to a reference impedance. Since resonators can have a wide range of impedances, specification of the resonator absorbed power is more suitable.* Deliverable power can then be found using the ratio of the load impedance to the device impedance.

The absorbed power in the resonator is expressed in the mechanical domain as

$$P_{\mathrm{R,max}} = \frac{W_{\max}\omega}{Q} \tag{2.10}$$

in which maximum stored energy is given by

$$W_{\max} = \frac{1}{2} k_{tot} u_{\mathrm{max,pk}}^{2} \tag{2.11}$$

where $u_{\text{max-pk}}$ is the maximum peak displacement amplitude.†

The nonlinearities observed in the measured devices originate from material limitations [43] and not due to geometric effects, electrostatic stiffness nonlinearities, or transduction nonlinearities. This is especially convenient for understanding fundamental limitations. The linearity of the material is defined by the maximum strain or the maximum energy density. For a 1D extensional resonator, the dynamic stiffness is

$$k_n = \frac{n^2 \pi^2 E_i A_x}{2L}. \tag{2.12}$$

---

* As in any lossy element, absorbed power leads to self-heating. In most cases, the resonator body is a sufficiently good thermal conductor so that localized temperature gradients are minimal.

† Throughout this document, harmonic signals are rms values unless otherwise specified. For example, $u_{\max}$ is the maximum rms displacement, whereas $u_{\mathrm{max,pk}}$ is the maximum peak displacement.

The energy density $\rho_w = W/(Lwt)$ for a 1D extensional resonator is given by

$$\rho_{\mathrm{W,max}} \approx \frac{n^2\pi^2 E_i}{4}\left(\frac{\overline{U_m}_{,\mathrm{max\text{-}pk}}}{L}\right)^2 \tag{2.13}$$

Since the peak strain occurs at the center of the structure, where $S = n\pi\overline{U_m}L^{-1}$,

$$\rho_{\mathrm{W,max}} \approx \frac{E_i S_{\mathrm{max}}{}^2}{4} \tag{2.14}$$

Reported maximum energy densities for bulk acoustic wave quartz crystal units and capacitive silicon micromechanical resonators are 190 J/m^3 and 180 kJ/m^3, respectively [44].[‡] Since stored energy loosely determines the noise floor of an oscillator, a quartz resonator and a silicon resonator with 1/1000 of the volume will enable the same noise floor.

The maximum rms output current is the product of η and the maximum rms velocity. Simplifying, $I_{2,\mathrm{max}}$ becomes an expression of η and material properties.

$$I_{2,\mathrm{max}} = \eta\sqrt{\frac{W_{\mathrm{max}}}{m_n}} = \sqrt{2}\eta\sqrt{\frac{\rho_{\mathrm{W\,max}}}{\rho_m}} \tag{2.15}$$

Increasing the electromechanical coupling will increase $I_{2,\mathrm{max}}$. The absorbed power, however, remains constant since $P_{\mathrm{R,max}}$ is defined by material limits.

[‡] For the ‹110› direction in silicon, a maximum strain S_{max} of ~0.21% is expected at the elasticity linearity limit.

2.3 Generalized Capacitive Coupling

In the expressions for the motional parameters, the dynamic mass and stiffness are given by

$$m_n = \rho \frac{\int_V u^2(x,y,z)dV}{{u_a}^2}, \text{ and} \tag{2.16}$$

$$k_n = \omega^2 m_n \tag{2.17}$$

Assuming a capacitive resonator has a uniform displacement along the electrode, u_a is evaluated at any point on the resonator surface. This assumption is used in deriving η for parallel-plate resonators (2.4). Some devices, however, do not have uniform displacement along the electrode (Figure 2.2). The objective is to take the mode shape of a general resonator and map into a parallel-plate equivalent. It is shown in Appendix A.3 that the average displacement along the electrode $\overline{u_y}$ is the proper value for u_a. The parameters m_n and k_n are modified and (2.4) remains valid for the complex mode shape.

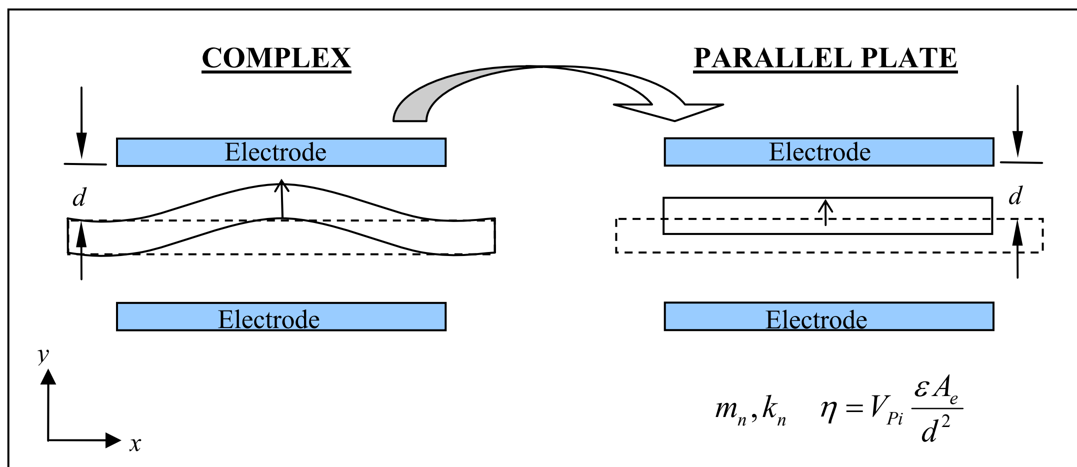

Figure 2.2 Mapping of a capacitive resonator with complex mode shape into a parallel-plate equivalent.

2.4 Finite Element Modeling

Analysis by the finite element method is useful especially for anisotropic materials. Although recent modeling tools also include the ability to model transduction, the analyses in this work are purely structural. By doing so, complexity of the models and computational requirements are kept at a minimum.

ANSYS was selected as the analysis platform. All models of single crystal silicon in this work are meshed with SOLID186 elements. The element axes are rotated to align to specific orientations in SCS. Mapped meshing is done for all models. Verification and mesh-dependency analyses were performed to validate the models. The majority of the models are used in three-dimensional (3D) modal analyses. Some nonlinear static analyses were also completed to understand resonator characteristics. Preloaded stress analysis in ANSYS also provided the ability to model the effect of external vibrations on resonator behavior.

The numerical models in this work, particularly the capacitive coupling analyses utilize results generated by ANSYS. Data is extracted from ANSYS output files and are subsequently processed in MATLAB.

2.5 Manufacturability

The minute dimensions, for which micromechanical resonators are attractive, also raise manufacturability challenges. Precision and repeatability in the operating frequency are critical for most applications. A variety of techniques have been suggested to address the manufacturability issue [45]. Post-fabrication trimming techniques including laser ablation [45,46] and selective material deposition by localized heating [47,48] have been proposed. However, these serial and possibly iterative processes may limit throughput. Selection of one device in a large fabricated array is also plausible, albeit at the cost of increased die area. Programmable fractional-N phase-locked loops (PLL) have also been demonstrated as a solution to obtain initial accuracy [49,50].

The proposed approach is based on design for manufacturability (DFM). Single crystal silicon is again attractive since its mechanical properties are deterministic. In contrast, DFM is difficult with deposited structural materials since their elasticity may vary by several percent. Since the density and elasticity of silicon is dependent on doping and directionality, sufficiently accurate quantification of doping profiles and alignment to crystal axes are critical for repeatability.

2.5.1 DFM for Capacitive Resonators

High-performance capacitive resonators must have large transduction area. This requirement calls for deep reactive ion etching (DRIE) of thick devices, whether trenches are used for transduction [43,51] or used in defining sacrificial gaps [15,38]. Trench etching has non-ideal characteristics such as scalloping, striations, footing, and non-

vertical profiles (Figure 2.3). The first two phenomena and can be controlled to within 50 nm with respectable etch rates. Footing is minimized with good process control. Although trench tapering and tilt can be as high as ±5° across substrates, their effect is minimal since the resonators operate in lateral modes along the substrate (further discussed in Section 5.5).

Other than etch, lithography and pattern transfer account for the majority of micromachining variations. They limit the dimensional accuracy of micromechanical resonators, which typically compromises center frequency accuracy. Although these variations are temporally random, they are spatially systematic (*i.e.*, all features on a single device can be assumed to have equal bias). Figure 2.4 shows the effect of process bias on uniform clamped-free and clamped-clamped beams.

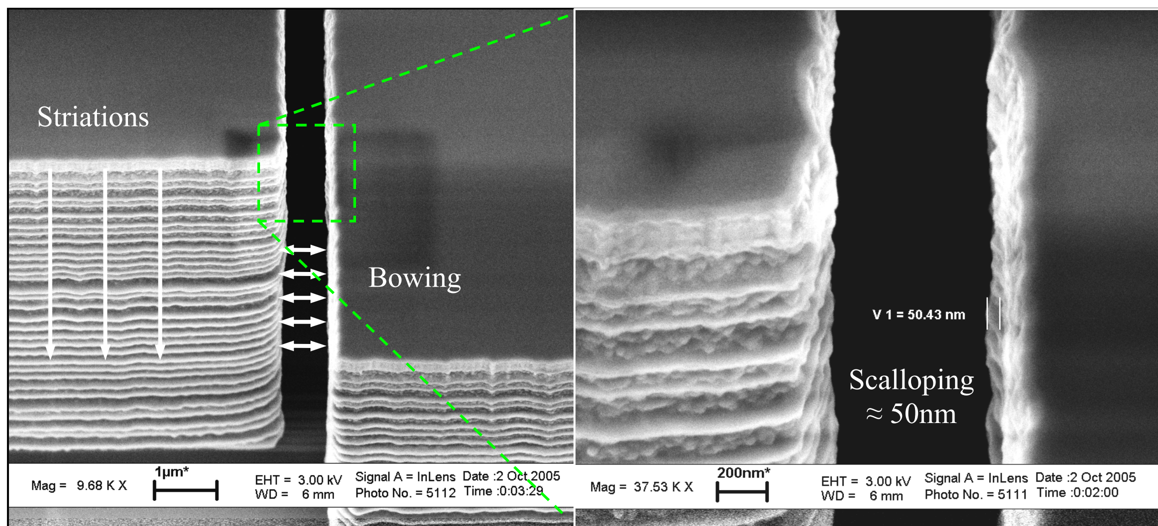

Figure 2.3 Striations, bowing, and scalloping in deep reactive ion etching.

Process compensation of center frequency is conceptually straightforward. Since critical dimension (CD) variations lead to deviations from the modal stiffness k_n and mass m_n, the natural frequency given by

$$f_n = \frac{1}{2\pi}\sqrt{\frac{k_n}{m_n}} \tag{2.18}$$

may also deviate from the ideal design value. A robust design ensures that variations in k_n are proportional to variations in m_n such that f_n has zero-sensitivity to process bias δ.

$$\frac{\partial f_n}{\partial \delta} = 0 \tag{2.19}$$

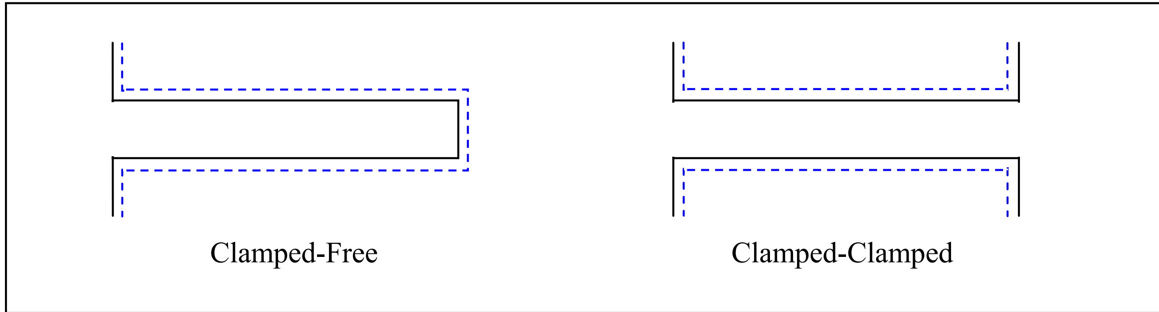

Figure 2.4 Design dimensions and resulting geometry from process bias on clamped-free and clamped-clamped beam resonators.

2.5.2 Starting Material Considerations

The DFM approach is contingent on a repeatable acoustic velocity. Assuming a one-dimensional mode, v_a is given by

$$v_a = \sqrt{E_i / \rho_m} \tag{2.20}$$

Since f_n is linearly dependent on v_a, the acoustic velocity must be repeatable. Although the elastic moduli E_i and mass density ρ_m of silicon are known only to within ±200 ppm for a limited number of dopant concentrations [52], we can make qualitative conclusions from the data.

The acoustic velocities vary by less than 1% between pure ($\rho_e \approx 10^{13}$) and heavily phosphorus-doped ($\rho_e = 2\times10^{19}$) silicon. Heavily-doped silicon grown by the Czochralski method typically has dopant uniformity better than 5:1 throughout the ingot and over time. Substrates doped by implantation have greater dopant uniformity. From this, it is plausible that the variation of v_a due to dopant concentration variation is 100 ppm or less.

Since silicon is anisotropic, wafer alignment to crystallographic directions is required. On the (100) plane, the directional elasticity varies 15 ppm and 90 ppm for ±0.2° and ±0.5° offset from ‹110›, respectively [53]. Thus, the ability to align features accurately to ‹110› and to align the substrate normal to ‹100› also dictates the v_a repeatability.

2.5.3 DFM of a Clamped-Free Beam

Although each process has unique process bias characteristics, a generic DFM approach is presented. The process bias on the critical dimensions (CD) and other features on any single resonator are assumed to be systematic. For example, the effect of process bias on clamped-free and clamped-clamped resonators is shown in Figure 2.4.

Clearly, the uniform beam geometries in Figure 2.4 cannot be process compensated. However, it is analytically proven in Appendix A.6 that the tapered profile in Figure 2.5 can satisfy (2.19). The mode shape of the CF beam can be approximated by $u_y = (x/l)^a$, where a is typically bound by [1.4,2.0]. Depending on the value of a, ratios between the width at the free end w_2 and at the clamped-end w_3 exist which allow process compensation. The locus satisfying (2.19) for a range values for a is shown in Figure 2.6. The solution requires that w_2 be 10–20% of w_3.

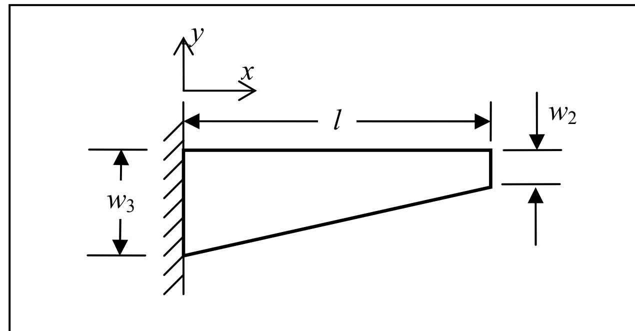

Figure 2.5 Clamped-free flexural beam with a generic profile along the length.

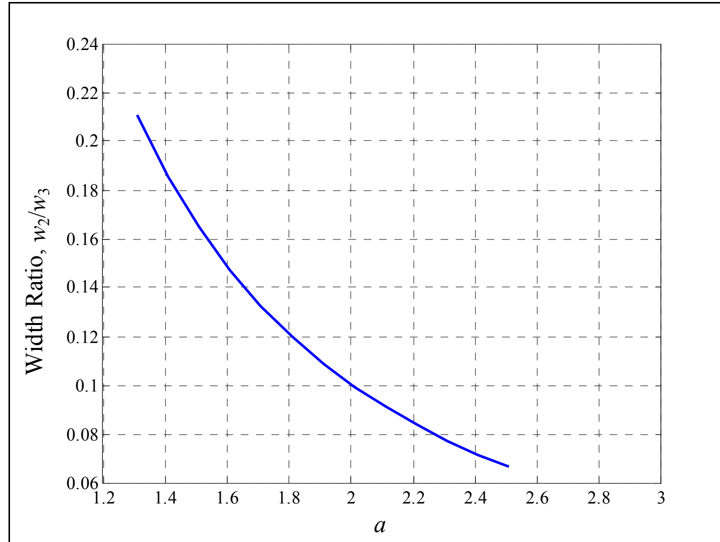

Figure 2.6 The locus of w_2/w_3 that satisfies the condition of zero frequency-sensitivity on process bias for a clamped-free beam.

For verification, finite element analysis was performed. The FE model of a 10-MHz process-compensated clamped-free beam and its frequency sensitivity are shown in Figure 2.7. The frequency variation over a process bias window of ±0.5 μm is 800 ppm. Since extensional mode resonators have the largest dimensions, the frequency variation for an extensional resonator at the same frequency is also shown (as a blue dotted line) in Figure 2.7. The predicted frequency variation for the beam is less than half the variation for the 10-MHz extensional resonator.[§]

Considering all the factors contributing to variations in frequency, it is conceivable that micromechanical resonators can be manufactured to within 1000 ppm of the target f_0 as-fabricated. To further improve accuracy for exacting frequency specifications, frequency tuning using a bias voltage is a viable option.[**]

[§] In Section 0, another process-compensated resonator design is discussed. The predicted frequency variation is within 1 ppm for the process bias range of ±0.5 μm.
[**] Elaboration on this topic is continued in the Conclusions, page 91.

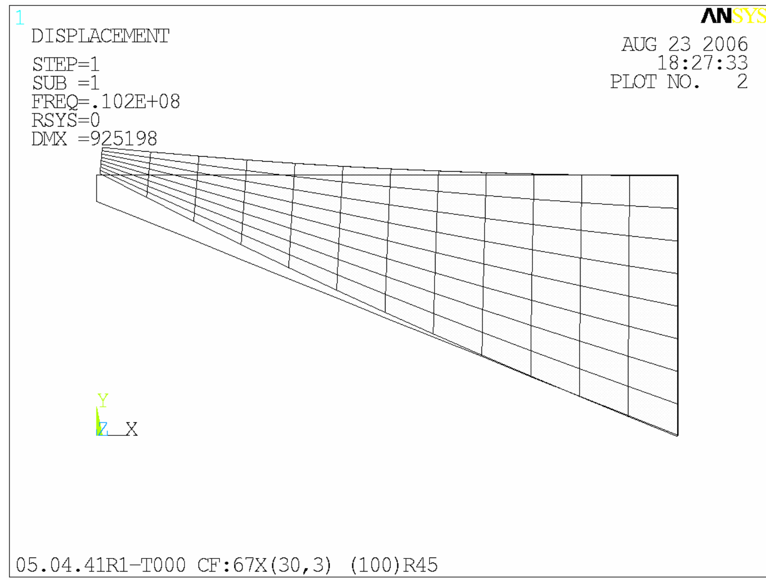

Figure 2.7 Finite element model of a tapered 10-MHz clamped-free beam resonator.

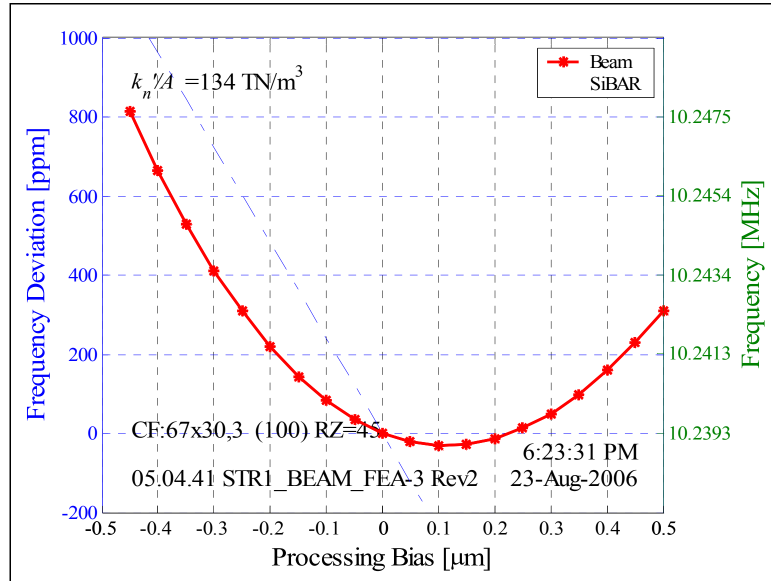

Figure 2.8 Frequency sensitivity of a tapered process-compensated 10-MHz clamped-free beam resonator.

2.6 Resonator Interfacing & Experimental Setup

Two experimental apparati were used in collecting the reported data. The majority of the data was collected using an Agilent 4395A network analyzer with a resistive divider (Figure 2.9). Resonators were often characterized in vacuum, either in a Desert Cryogenics vacuum probe station or in a custom vacuum chamber (*i.e.*, wire-bonded on a PCB). As research progressed, an Agilent E5071B network analyzer with an *s*-parameter test set was acquired. High-frequency piezoelectric resonator measurements reported in Section 4.2 were made on a Suss RF probe station with GSG probes at atmospheric pressure. SOLT calibration was performed on the Agilent E5071B network analyzer.

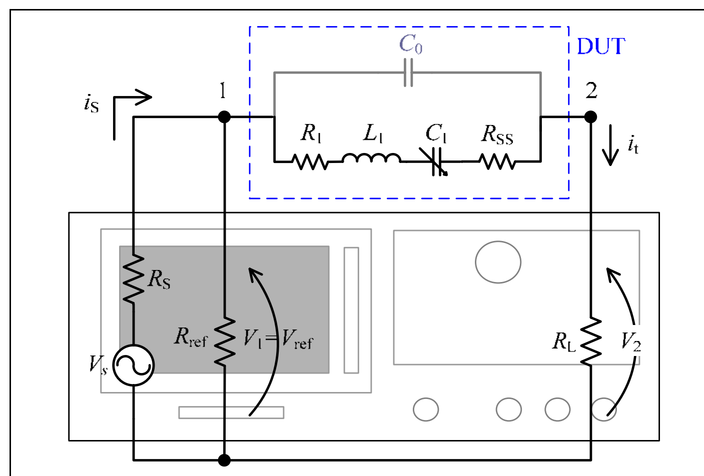

Figure 2.9 Experimental Apparatus A: Agilent N4395A with a resistive divider test set for transmission measurements.

2.6.1 Device Impedance and Quality Factor

Low motional impedance has been difficult to achieve in capacitive resonators until recently. For devices measured using the resistive divider test set, the test impedance R_t is given by

$$R_t = R_L \left(\frac{1}{A_V} - 1 \right) \tag{2.21}$$

where R_L is the termination and A_V is the transmission level at series resonance. With an *s*-parameter test set, R_t is given by

$$R_t \approx 2 \cdot R_L \left(\frac{1}{s_{21}\big|_{f_s}} - 1 \right) \tag{2.22}$$

where s_{21} is taken at series resonance (*i.e.*, the insertion loss). R_t is the sum of the motional resistance R_1 and any small signal resistance R_{ss} in the device.

$$R_t = R_1 + R_{ss} \tag{2.23}$$

Quality factors are evaluated in the equipment using the expression

$$Q = \frac{f_0}{f_{3\text{dB}}} \tag{2.24}$$

where $f_{3\text{dB}}$ is the 3-dB bandwidth. Since the unloaded and loaded Q are given by

$$Q_U = \frac{\omega L_1}{R_1} \text{ and } Q_L = \frac{\omega L_1}{R_t + R_S + R_L} \tag{2.25,2.26}$$

respectively, the motional resistance can be found from Q_L and Q_U (*i.e.*, at small V_P). R_S is the source impedance.

$$R_1 = \frac{Q_L}{Q_U} \left(R_t + R_S + R_L \right) \tag{2.27}$$

To obtain the unloaded Q in the Agilent 5071B, smaller R_S and R_L can be simulated.

2.6.2 Linearity

In Section 2.2, the justification for expressing resonator linearity as absorbed power was presented. Nonlinearities in the mechanical frequency response are easily observed with the network analyzer. For the measurement taken with the resistive divider, the absorbed power is approximated by

$$P_{\mathrm{R}} \approx P_1 + \frac{A_V}{2} \quad [\mathrm{dB}] \tag{2.28}$$

for R_1>>100Ω (see Appendix A.5).

CHAPTER 3 CAPACITIVE VHF SiBARs

The rectangular* silicon bulk acoustic mode resonator (SiBAR) is ideally suited for low-phase-noise oscillators in the VHF and UHF bands. A scanning electron micrograph (SEM) is shown in Figure 3.1. The longitudinal mode is similar to that of a film bulk acoustic resonator [54-56]. The large lateral dimensions and the potential for high Q are favorable over beam [13,57] and disk [14] resonators. The natural frequencies are given by

$$\omega_n = \frac{\pi n v_a}{L} \text{ or } f_n = \frac{n v_a}{2L}. \tag{3.1}$$

in which n is the mode number and L is the dimension along the longitudinal direction.

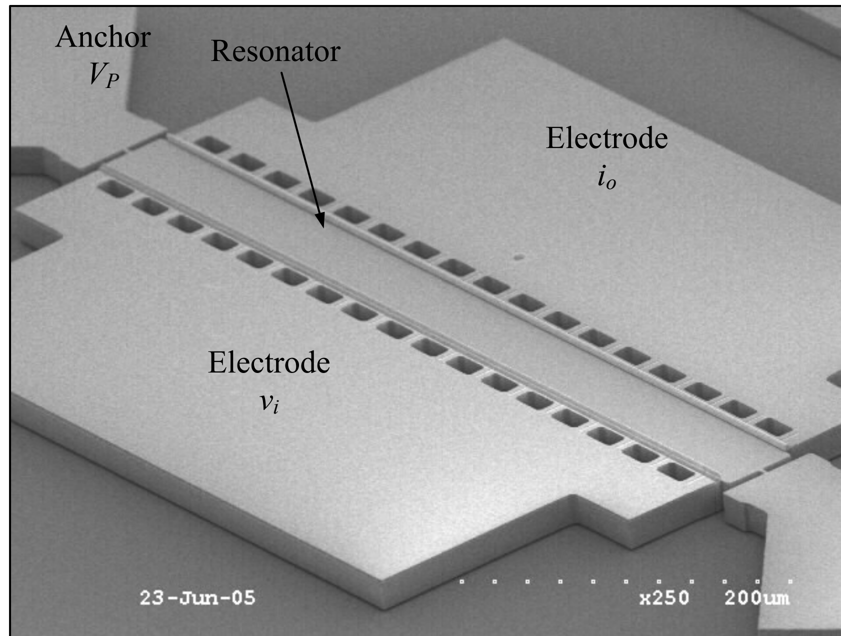

Figure 3.1 SEM of a 388μm×40μm×20μm two-port fundamental-mode SiBAR with 225-nm gaps fabricated using the HARPSS-on-SOI process.

* Other geometries for bulk extensional modes, including conical rings and rectangular "window frames", have also been considered. Conical rings have good mode shapes in isotropic materials and on (111) substrates.

To evaluate the mode shapes in isotropic materials and anisotropic materials conveniently, a numerical approach based on 3D finite element analysis was used. The aspect ratios were varied to observe the effect of geometry on the modes. From the analysis results, the following naming convention has been adopted for the modes.

BEN_1.N_2.N_3.A/B

The **BE** represents bulk extension, as opposed to shearing, flexing, or torsion. N_1 is the mode order along the primary frequency defining dimension, N_2 is the mode order along the other dimension in the plane of the substrate, and N_3 is the mode order along the height. The A/B designates the characteristics of the modes since there are two for each N_2 mode.

The metric in the optimization for low impedance is the relative stiffness k_r. The relative stiffness is simply a comparison between the actual dynamic stiffness (2.17) and the stiffness of an ideal 1D resonator. A value of unity suggests the contribution of length-extension to the modal energy is 100%. As k_r increases, the deformation along the electrode may not be uniform. In modes where regions along the electrode are out of phase, k_r is very large. The inverse of k_r is the relative compliance c_r.[†] A smaller value of k_r (and k_n) results in a lower motional resistance.

$$k_r \equiv \frac{k_n}{k_{n,\mathrm{1D}}} = \frac{1}{c_r}. \tag{3.2}$$

[†] Modes along the direction of interest may be coupled to shear, flexural, torsional, or bulk-extensional modes along other directions. If energy is attributed to deformation in any form other than the mode of interest (*i.e.*, deformations not normal to the surface of the electrode), the increase in modal energy will result in a larger dynamic stiffness k_n. Physically, charge cancellation occurs at the output when regions have out-of-phase displacement.

3.1 Thin Isotropic Plate Analysis

In the fundamental LE11 mode, the relative stiffness is approximately unity when the width (*i.e.*, the *x*-dimension) is less than half of the length (Figure 3.2a). As the width is increased, k_r increases since the deformation along the electrode deviates further from uniformity. See Figure 3.3a. For w/*L*=1, a Lamé mode exists, for which k_r=2. As the aspect ratio (AR) is increased, the frequency of the LE11 mode decreases. Figure 3.3b contains the dispersion curves of the normalized frequency for each mode as AR is varied. Many modes exist in these resonators. "High-order" modes are more prominent and more suitable as the lateral dimensions increase. The k_r versus AR profile of the BE13 mode is illustrated by a wide trough and reaches a minimum of 1.2 for w/L = 1.6. Other bulk-extensional modes, such as the BE15, BE17, and BE19 modes also exhibit k_r minima for *AR* equal to 2.8, 4.3, and 7.0 respectively. This is especially encouraging since greater transduction area (*i.e.*, wider devices) provides better coupling.

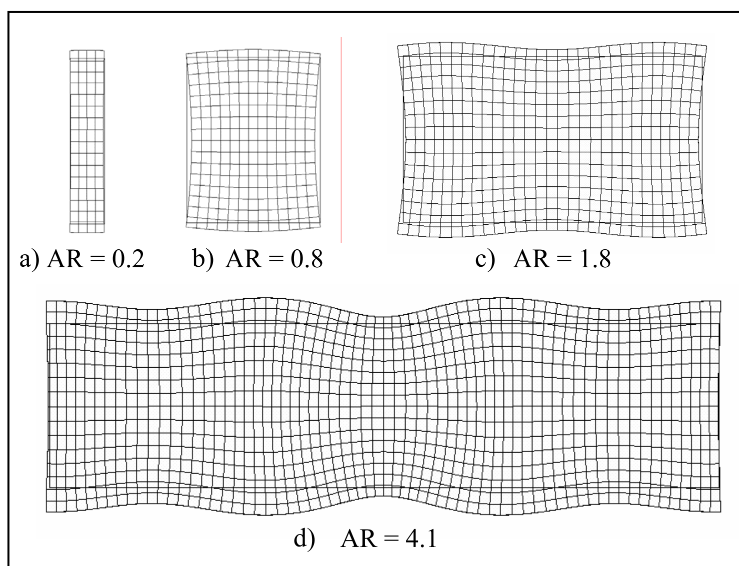

Figure 3.2 Extensional modes for a rectangular isotropic resonator.

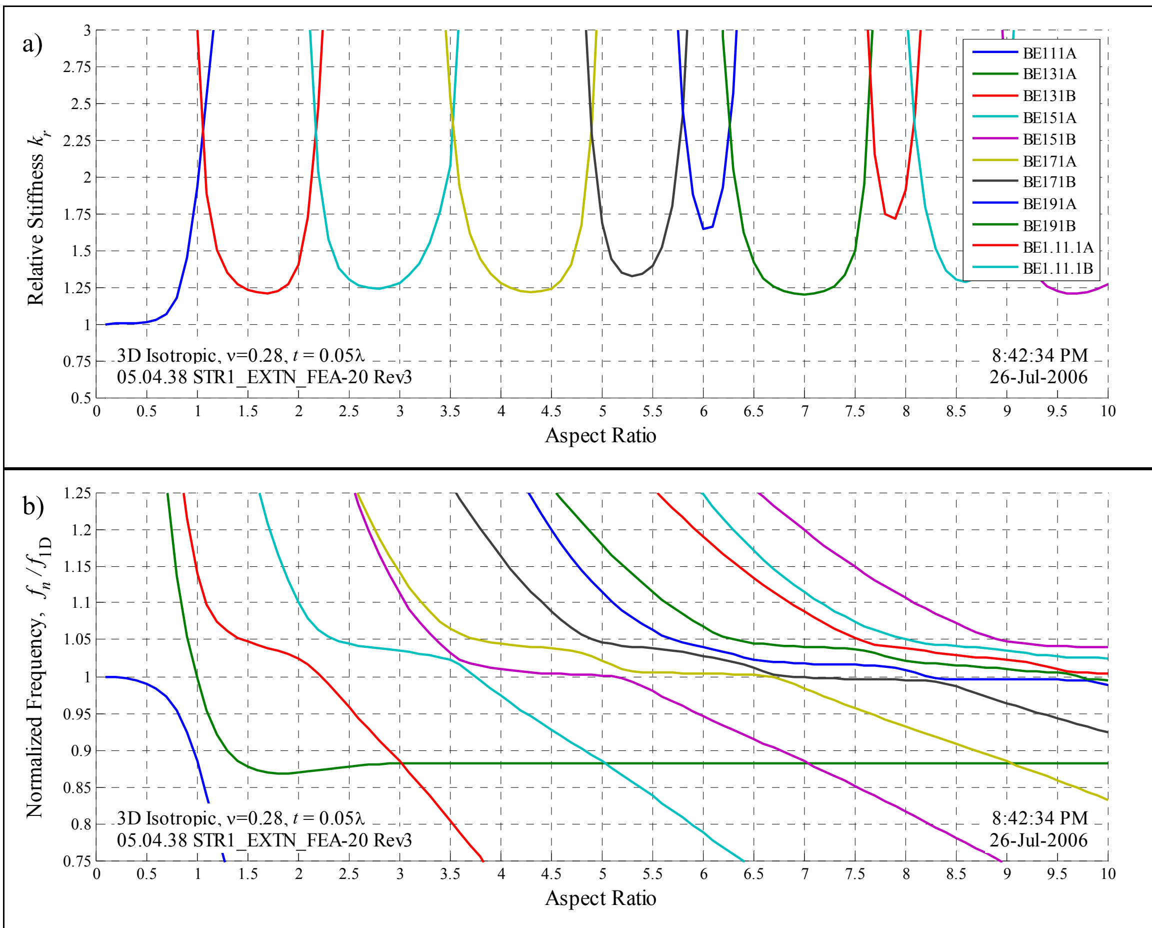

Figure 3.3 Relative stiffness k_r and normalized frequency of the extensional modes of a thin isotropic plate.

Figure 3.4 shows the BE171A mode for four geometries. In Figure 3.4a, w/L=3.5 and some periodicity is observed in the mode shape. Figure 3.4b shows the w/L=4.1 geometry in which there is minimal lateral displacement at the anchor location. The mode in Figure 3.4c (w/L=4.3) is optimally coupled, for which k_r=1.25. As the aspect ratio is further increased to 4.8 (Figure 3.4d) coupling is reduced and k_r is large. These four plots correlate to the olive-colored line in Figure 3.3a.

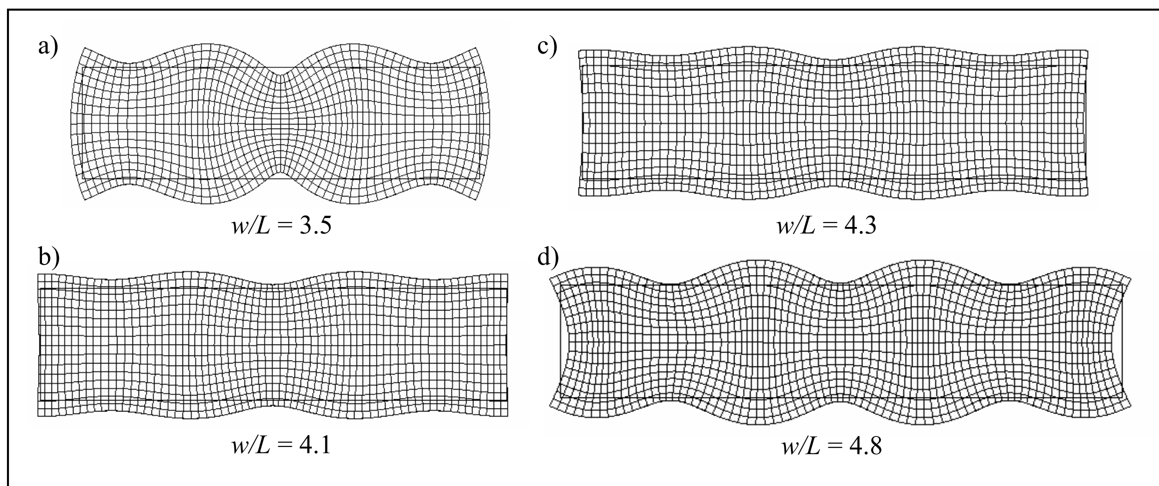

Figure 3.4 Mode shape variation of the BE171 mode as aspect ratio varies between 3.5 and 4.8.

3.2 Thin SiBARs ‹110›

A similar analysis was performed for thin SiBARs aligned to ‹110›. The thickness t is one-tenth of the wavelength λ. The optimal mode shape for the BE151A mode is shown in Figure 3.5 for a 40μm long resonator. In comparison to the mode shapes in Figure 3.2 and Figure 3.4, the displacement is substantially uniform. The w/L aspect ratio is 3.7 and the predicted frequency is 106 MHz. In the analysis summary (Figure 3.6a), the advantage in using anisotropic resonators is evident. There is a large range of aspect ratios in which the minimum relative stiffness is unity (compared to k_r=1.25 for an isotropic plate).

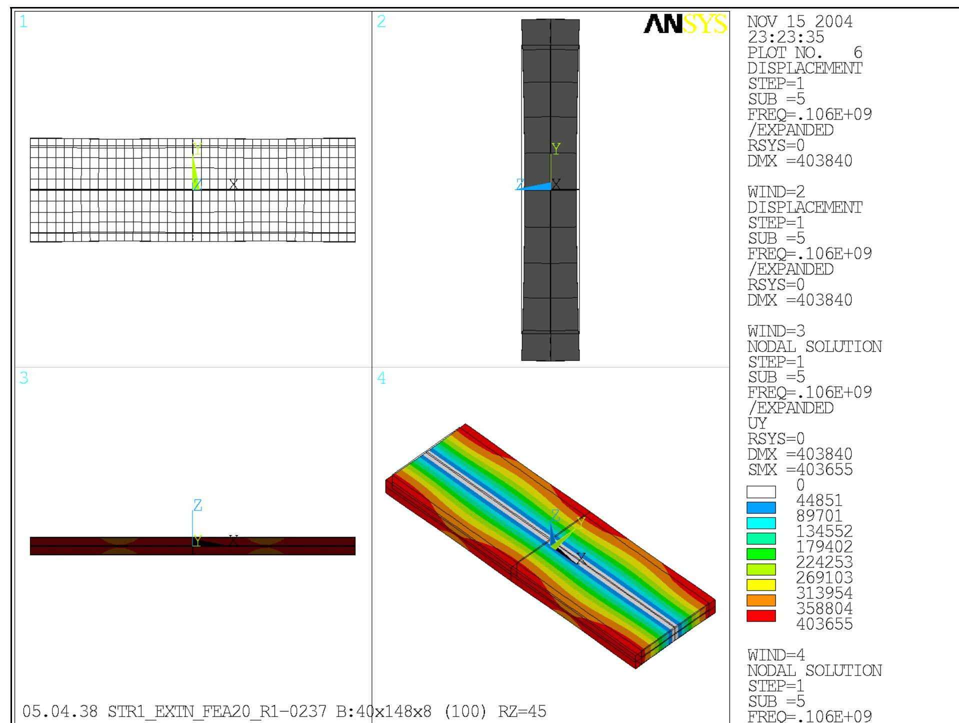

Figure 3.5 Uniform mode shape in a thin 3D anisotropic SCS plate (AR=3.7, $t = \lambda/10$).

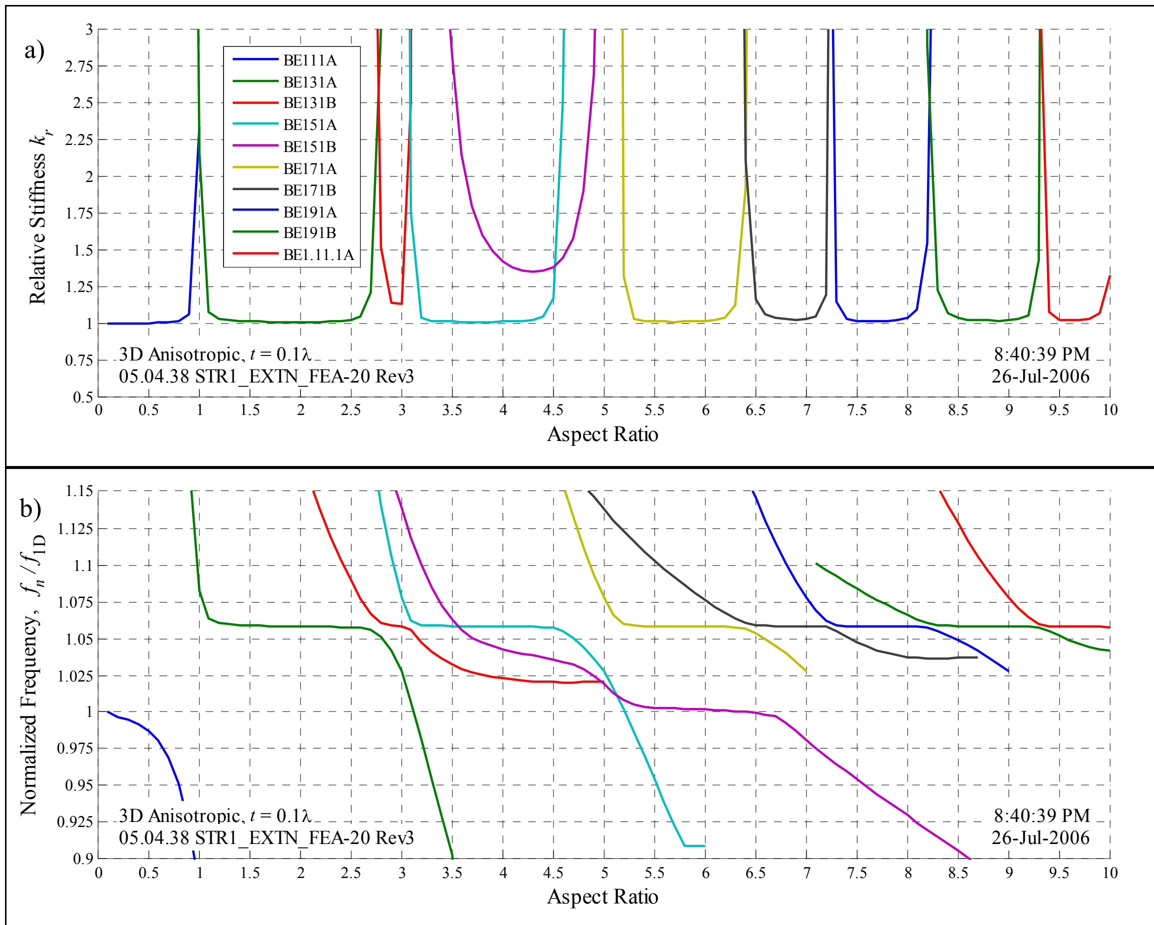

Figure 3.6 Relative stiffness k_r and normalized frequency of the extensional modes of a thin (t=λ/10) SiBAR aligned to ‹110› on the (100) plane.

3.3 Quarter-Wavelength-Thick SiBARs ‹110›

A greater thickness is desired for lower impedance and greater linearity. However, characteristics of the mode shapes change as device thickness is increased. The analysis results for quarter-wavelength-thick SiBARs is presented. The optimal aspect ratio for the BE151A mode for minimal lateral displacement is 3.8 (Figure 3.7). The minimum relative stiffness (Figure 3.8a) is 1.02 and the troughs are wider than in Figure 3.6 for thin plates. Periodicity in the k_r curves and dispersion curves is evident.

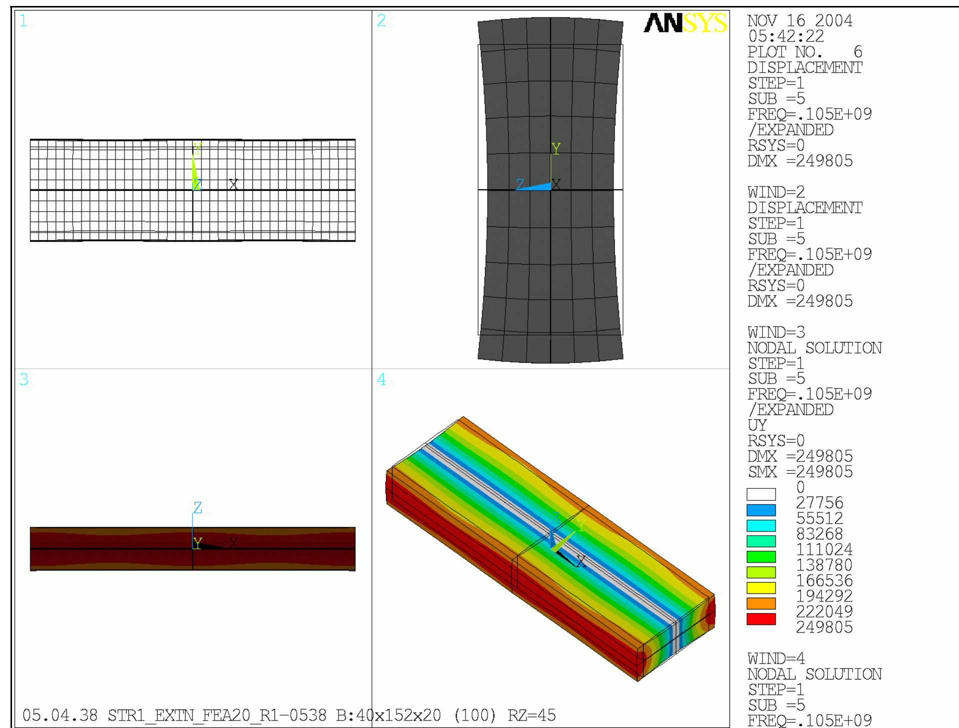

Figure 3.7 Uniform mode shape in a thin 3D anisotropic SCS plate (AR=3.8, $t = \lambda/4$).

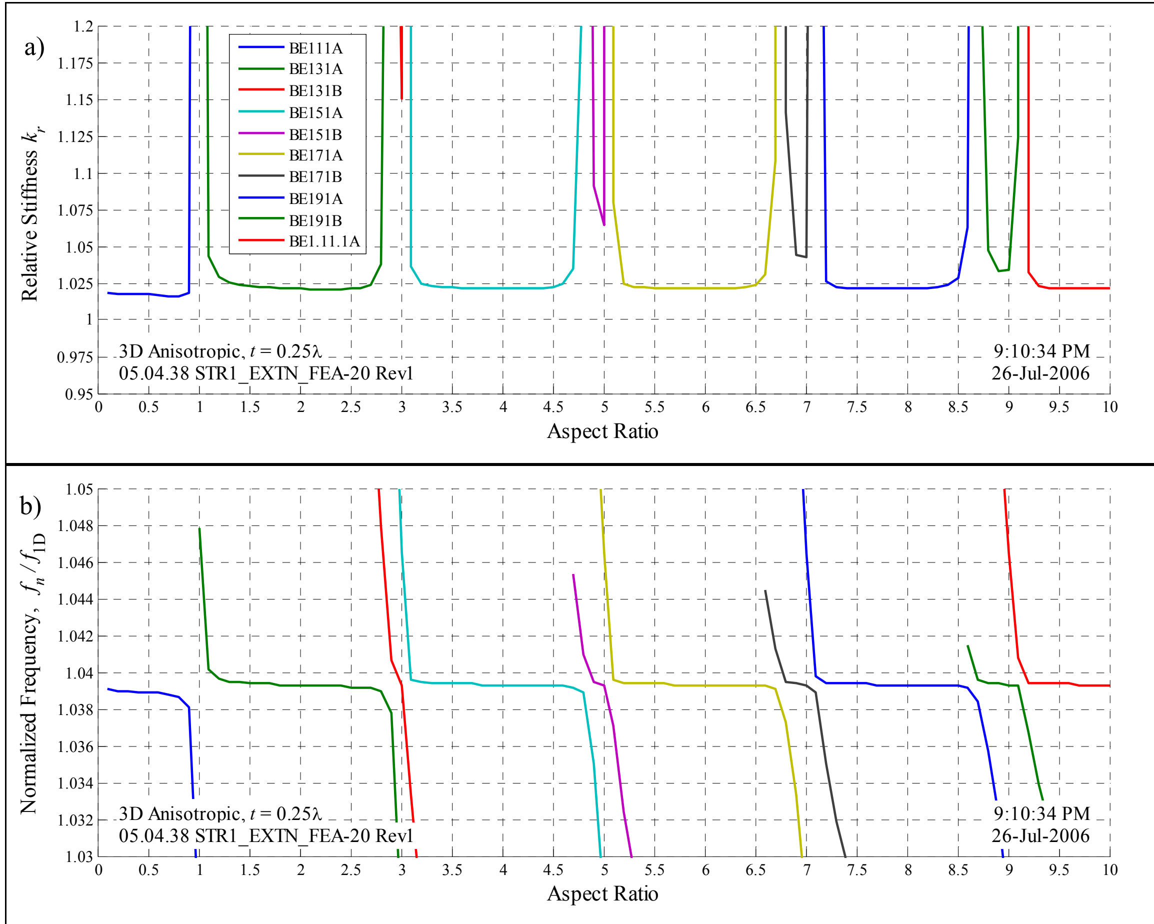

Figure 3.8 Relative stiffness k_r and normalized frequency of the extensional modes of a thin (t=λ/4) SiBAR aligned to ‹110 › on the (100) plane.

3.4 Thick SiBAR Plates ‹110›

As the third dimension of a SiBAR is increased, wave-like characteristics are present in all three dimensions. The two-dimensional (*i.e.*, planar mode) assumption only holds up to a thickness of 0.3 λ. In general, regions along the transduction surface may be out-of-phase in any given mode and poor coupling will result. As with increasing the lateral dimension, there are aspect ratios for which the coupling is optimal. Some thick SiBARs have modes with all regions in-phase, although they are not uniform as in thin (*i.e.*, $t \leq 0.3\lambda$) devices. One of these geometries is shown in Figure 3.9, for which the relative stiffness is 1.38. Although an exhaustive analysis has not been completed on thick structures, one can presume plots similar to Figure 3.6 and Figure 3.8 could be generated to identify optimal geometries.

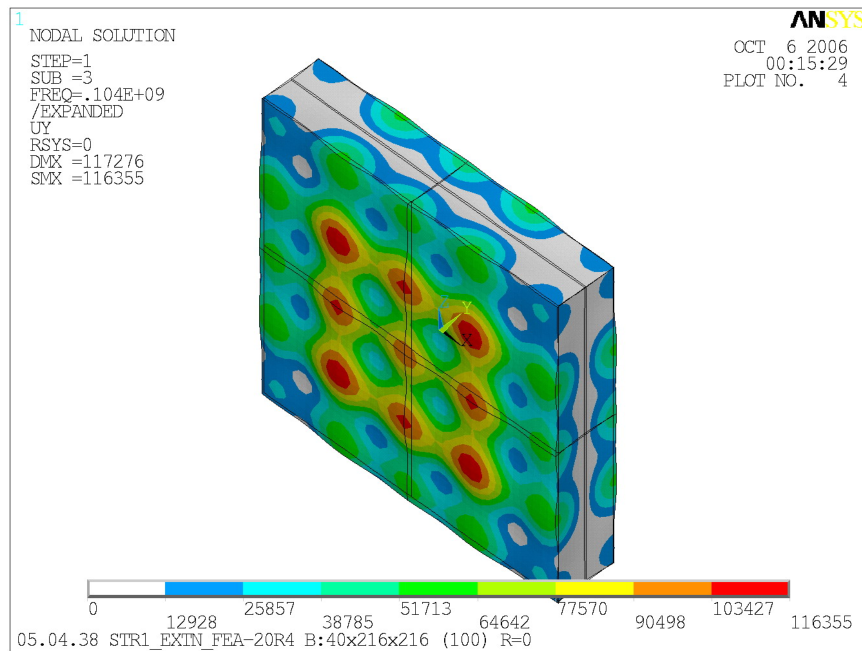

Figure 3.9 Mode shape of a thick SiBAR with all regions in phase.

3.5 Analysis and Characterization

The FEA results show that optimized thin SiBARs can be treated as a 1D device. Based on the 1D assumption, expressions for the device impedance is presented. Measured device characteristics are also presented to verify the models.

3.5.1 Dynamic Stiffness

The dynamic mass and stiffness of a one-dimensional SiBAR are given by

$$m_n = \frac{\rho AL}{2} \text{ and } k_n = \frac{n^2\pi^2 EA}{2L} \tag{3.3,3.4}$$

at either end of the resonator. L represents the length of the resonator[‡] and n is the mode number. The dynamic stiffness can also be expressed as a function of the natural frequencies.

$$k_n = n\pi^2\sqrt{E\rho}A\cdot f_n \tag{3.5}$$

Taking E=168GPa for (100) SCS in the <110> direction and ρ=2328kg/m^3, the normalized stiffness is

$$\frac{k_n}{A} \cong n\cdot f_n \cdot 1.95\times10^8 \frac{\text{N}}{\text{m}^3}\frac{1}{\text{Hz}}. \tag{3.6}$$

Therefore, the normalized stiffness is 19.5 PN/m^3 (1 PN = 10^{15} N) for a 100-MHz resonator operating in its fundamental mode.

[‡] Length L is the frequency-defining dimension and not necessarily the largest dimension.

3.5.2 Motional Resistance and Quality Factor

Recall the motional resistance of a capacitive resonator (2.1).

$$R_1 = \frac{k_{tot}}{\omega_n Q \eta^2}$$

Substituting for η, R_1 becomes

$$R_1 = \frac{k_{tot} d^4}{\omega_n Q \varepsilon^2 V_P^{\,2} A_e^{\,2}} \tag{3.7}$$

Assuming $k_{tot} \approx k_r \cdot k_n$, $A_e = A$, $A_e = wt$, and substituting for k_n/A, R_1 is expressed as

$$R_1 = \frac{k_r n\pi \sqrt{E\rho} d^4}{2Q\varepsilon^2 V_P^{\,2} wt}\,. \tag{3.8}$$

R_1 is independent of frequency and its only geometric dependencies are the width w and thickness t. As a conservative measure, devices with $t = \lambda/4$ were fabricated on low-resistivity SOI with transduction gaps between 65 and 250 nm. The 40-µm long resonators all exhibit series resonance at approximately 106 MHz.

The highest Q measured from a nominally 100-MHz SiBAR with 225-nm gaps is 90000 at 5 torr (Figure 3.10). No changes in Q were observed when the pressure was reduced to high vacuum. The impedance of the SiBAR is 3.3 kΩ with a polarization of 25 V (Figure 3.11). The quality factor is reduced to 66000 at high V_P, however.

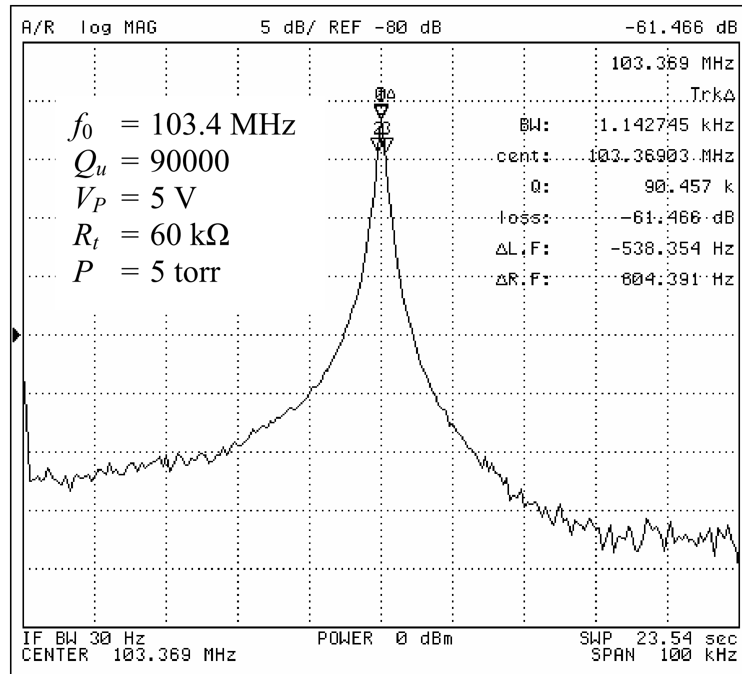

Figure 3.10 Frequency response of a 388μm×40μm×20μm SiBAR with 225-nm gaps showing an unloaded Q of 90000 with V_P=5V and P = 5 torr.

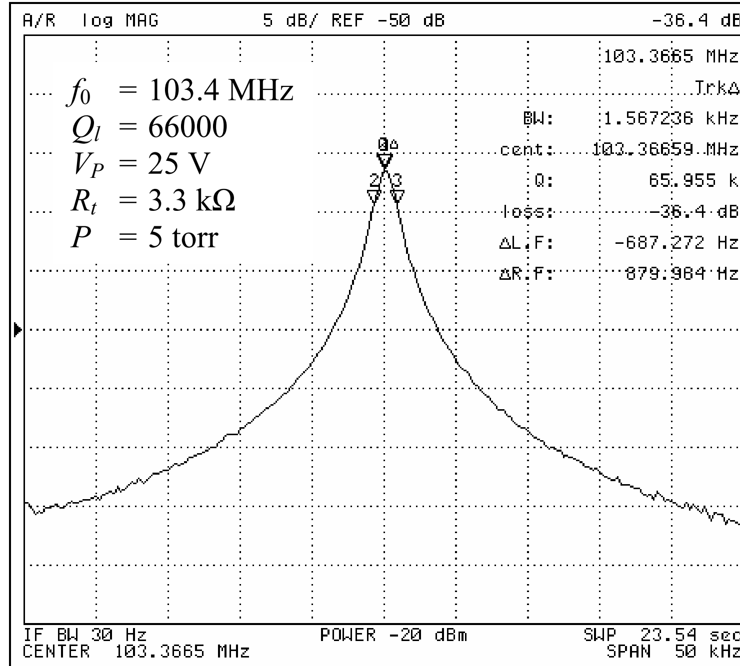

Figure 3.11 Frequency response of a 388μm×40μm×20μm SiBAR with 225-nm gaps showing an impedance of 3.3 kΩ and a loaded Q of 66000 with V_P = 25 V and P = 5 torr.

Quality factor loading has been observed in all resonators with R_1 of 10 kΩ or lower. Q_L reduces as V_P is increased (Figure 3.12). This is a result of a small-signal resistance R_{SS}. The origins of R_{SS} could possibly be the finite resistance of the resonator or electrodes or depletion in either component. In this 388-μm-wide SiBAR, R_{SS} is approximately 800 Ω.[§] When R_{SS} is added to the theoretical R_1, the predicted resistance matches the measured resistance very well (Figure 3.13). More data on Q-loading in SiBARs is shown in Figure B.1. From (3.8), wider devices are expected to have lower impedance. This is shown in the experimental data in Figure B.2.

[§] Low-resistivity (<5 mΩ-cm p-type) substrates were used in some instances and R_{SS} was reduced to a few hundred Ohm.

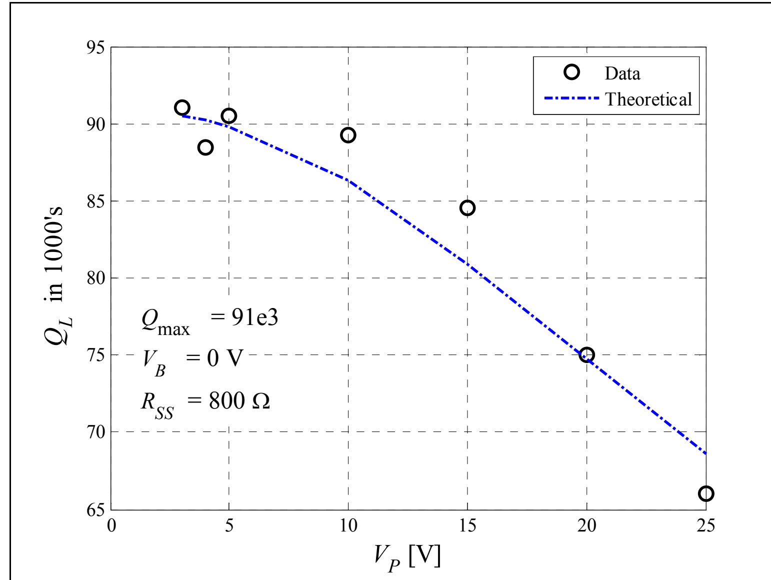

Figure 3.12 Measured and theoretical loaded Q of a 388µm×40µm×20µm 103-MHz SiBAR over a V_P range of 3 to 25 V.

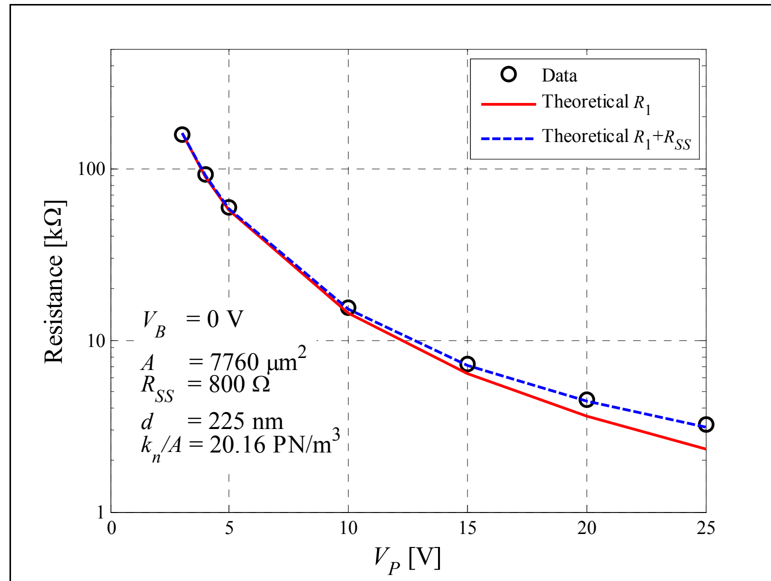

Figure 3.13 Theoretical and measured resistance of a 388µm×40µm×20µm SiBAR with 225-nm gaps at 5 torr pressure over a V_P range of 3 to 25 V.

3.5.3 Linearity

Another SiBAR was used for linearity characterization. The device is 20μm-thick, has 225-nm gaps, and has lateral dimensions of 232μm×40μm. The nominal Q is 40000 and its resistance is 8.7 kΩ when biased at 30 V (Figure 3.14). As the source power is increased from 0 dBm to +15 dBm, the resonance frequency decreases approximately 10 ppm. This is a sign of material or transduction nonlinearities. Interestingly, the Q increases and R_1 decreases for the slightly nonlinear operation. Assuming that the input power can be held relatively constant, the mechanical response at 15 dBm input is suitable for operation. Following (2.28),

$$P_{\mathrm{R}} \approx P_1 + \frac{A_V}{2} \quad [\mathrm{dB}]$$

the absorbed power is -7 dBm. With these conditions, the peak output current is 160 μA and the displacement amplitude is 16 nm (Table 3.1). As the displacement is less than one-tenth of the gap, the nonlinear response is likely the onset of elasticity nonlinearities. The energy density is 64 kJ/m^3 for these conditions, which is approximately one-third of the maximum energy density at bifurcation [44].

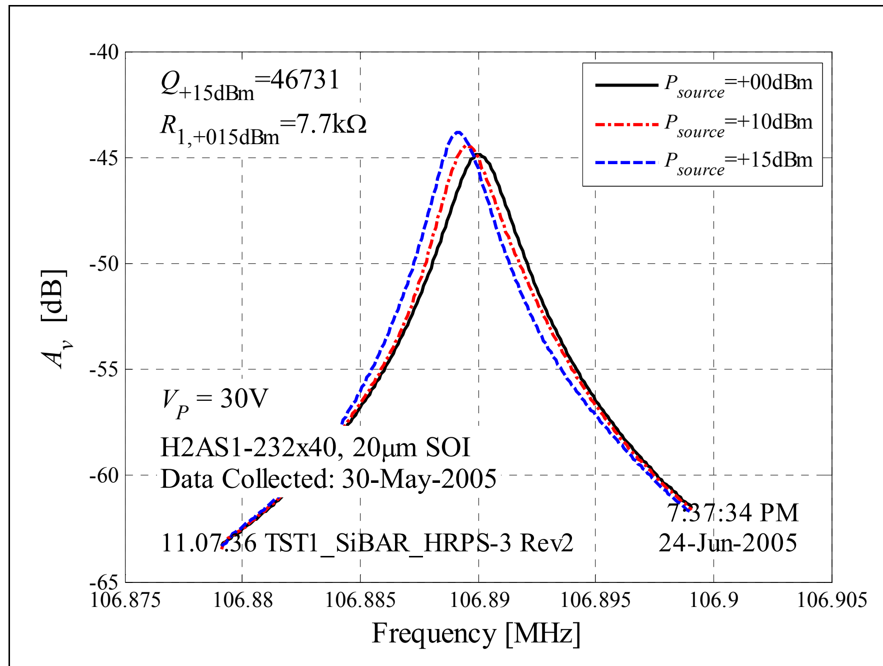

Figure 3.14 Linearity characterization of a 107-MHz SiBAR.

Table 3.1 Linearity of a 107-MHz 232µm×40µm×20µm SiBAR.

Input Power	P_1	0 dBm	15 dBm
Transmission	A_v	-45 dBm	-44 dBm
Absorbed Power	P_R	-22.5 dBm	-7 dBm
Stiffness	k_n	9.7×10^7 N/m	
Quality Factor	Q	40000*	
Motional Resistance	R_1	8 kΩ*	
Stored Energy	$W_{\max}$	0.33 nJ	12 nJ
Peak Displacement Amplitude	$u_{max,pk}$	2.6 nm	16 nm
Peak Localized Strain	S	0.02%	0.12%
Energy Density	ρ_W	1.8 kJ/m³	64 kJ/m³
Peak Output Current	$I_{2,\text{pk}}$	27 µA	160 µA

** nominal values*

3.6 Second- and Higher-Order Modes

Since SiBARs with low R_1 (<10kΩ) are susceptible to resistive loading, a solution is proposed. Even-order modes are presented to introduce asymmetry, such that charge migrates between the faces of the resonator. See Figure 3.15a. In this scheme, there is no net charge displacement in the resonator. Thus the small signal series resistance is expected to be lower. Manufacturability is another advantage of high-order modes. The fractional process bias on an nth-mode resonator is a factor of n lower, thus providing greater frequency accuracy. The increase in normalized stiffness, however, leads to greater R_1.

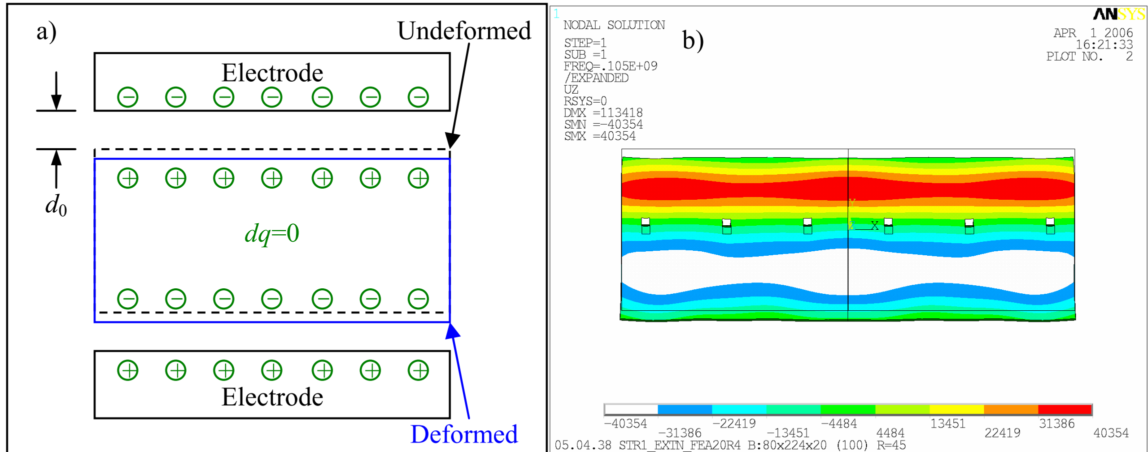

Figure 3.15 a) Small-signal charge migration and b) mode shape of a second-order SiBAR resonator.

CHAPTER 4 PIEZOELECTRIC LATERAL-MODE RESONATORS

Since bulk acoustic modes provide high frequencies with relatively large dimensions in comparison to other modes, they are attractive for extending micromechanical resonator technology to the VHF and UHF bands. The piezoelectric composite bulk acoustic resonator (CBAR) resembles a thin rectangular plate. Piezoelectric transduction is attractive since it provides greater electromechanical coupling. CBARs consist of a piezoelectric stack disposed on silicon (Figure 4.1). Similar to SiBARs, a one-dimensional (1D) model is sufficient for modeling the bulk extensional mode. The natural frequencies of a 1D system with free ends is given by

$$\omega_n = \frac{n\pi}{L}\sqrt{\frac{E_i}{\rho_m}} \tag{4.1}$$

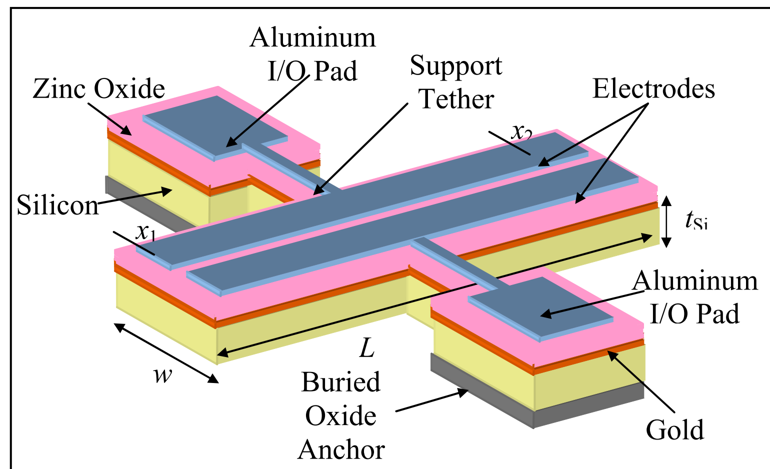

Figure 4.1 Piezoelectric-on-silicon lateral bulk acoustic micromechanical resonator.

The resonators are designed with a metal ground electrode as the third terminal to minimize C_0 and to obtain distinct zero-phase resonances. Previous attempts using low-resistivity silicon as the third electrode (*i.e.*, no metal) was ineffective for grounding [58]. Despite the possible reduction in Q from increasing layer count, measured Q values greater than 10000 will be presented. The resonators are conveniently anchored to the substrate at the mid-span node (where $x = L/2$) to minimize acoustic loss.

A finite element model was built in ANSYS. SOLID186 elements are used for the silicon structure and the patterned top electrode. SOLID191 elements are used for the composite piezoelectric stack. Ideal structural interfaces and stress-free conditions are assumed. Since the thickness of the SCS body is significantly greater than the transduction film, the SCS primarily defines the mode shape and frequency of the resonator.

4.1 Fundamental Mode

A scanning electron micrograph (SEM) of a 240μm×40μm device is shown in Figure 4.2. The form of the RLC expressions is the same as the capacitive resonator.*

$$R_1 = \frac{k_n}{\omega Q \eta_1 \eta_2}, L_1 = \frac{m_n}{\eta_1 \eta_2}, C_1 = \frac{\eta_1 \eta_2}{k_n}.$$

The difference is in η. A device having two symmetric half-width electrodes operating in length-extensional mode has coupling coefficients given by

$$|\eta| = 2 d_{31} E_f w_e \sin\left(\frac{n\pi L_\mathrm{e}}{2L}\right). \tag{4.2}$$

where d_{31} is the piezoelectric strain coefficient, E_f is the elastic modulus of the film, w_e is the electrode width, and L_e is the electrode length. Substituting for k_n and η,

$$R_1 \approx \frac{n\pi\left(t_\mathrm{Si} + t_\mathrm{f}\right)\sqrt{E_i \rho_m}}{2{d_{31}}^2{E_\mathrm{f}}^2 w Q} \frac{1}{\sin^2\left(n\pi L_\mathrm{e}/2L\right)}. \tag{4.3}$$

Similar to the SiBAR (3.8), R_1 for the CBAR is also independent of frequency. See Table C.2 for the material properties of zinc oxide, aluminum nitride, and PZT.

The fabricated resonators were wire-bonded on a PCB and characterized using Experimental Apparatus A (Figure 2.9). Typical shunt resistances of 1 to 20 MΩ were measured across the ZnO film.

* Complete analysis of the piezoelectric resonators is found in Appendix A.11.1.

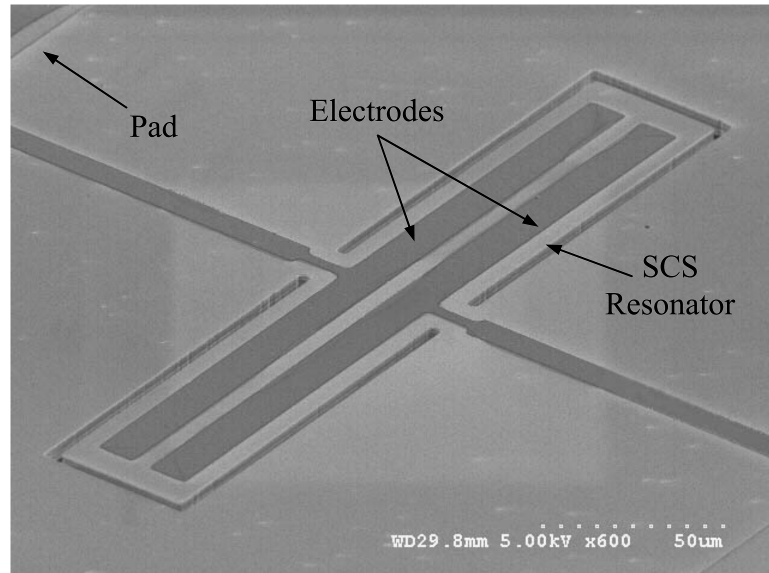

Figure 4.2 SEM of a 240μm×40μm fundamental-mode CBAR.

4.1.1 Length-Extensional Mode

The fundamental bulk mode of the 240μm×40μm resonator occurs at 15 MHz (Figure 4.3). By incorporating silicon as part of the resonator body, a Q of 11800 was measured at a pressure of 5 torr. The impedance is 1.6 kΩ. The response has a resonance peak that is 50 dB greater than the feedthrough (through a parasitic C_0 of 20 fF). In comparison to previous measurements without a gold ground plane, the feedthrough is reduced by 20-30 dB. The quality factor at atmospheric pressure for the same device is 6100. ANSYS modal analysis of the composite structure predicts a natural frequency of 15.3 MHz for this fundamental bulk mode (Figure 4.4). The simulated mode shape predicts that some out-of-plane displacement is present as a result of the asymmetric composite structure.

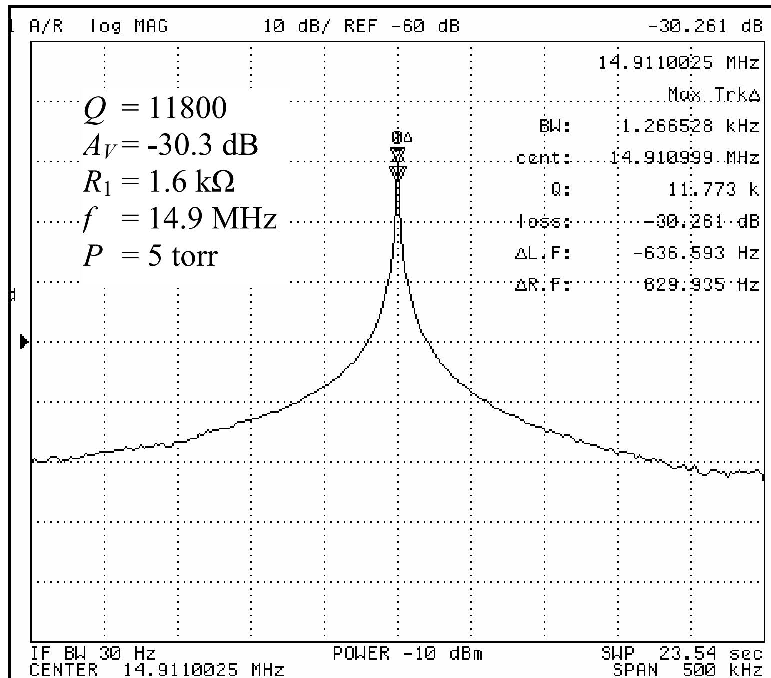

Figure 4.3 Frequency response at 15 MHz with P=5torr showing Q≈11700 and a 50 dB peak above feedthrough.

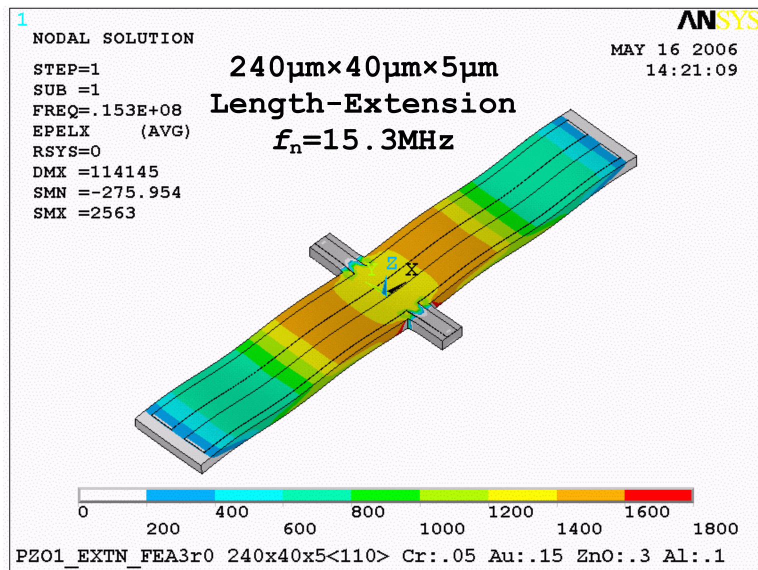

Figure 4.4 Simulated mode shape and unidirectional strain for the resonator in the 15-MHz mode.

4.1.2 Width-Extensional Mode

The implication of (4.3), that R_1 has an inverse dependence on electrode width, is proven with measurements. A width-extensional resonance at 90 MHz from the same 240μm×40μm resonator was observed (Figure 4.5) with lower R_1. The motional resistance is 500 Ω for a Q of 4100 in low vacuum for the 90-MHz mode. Since the electrode orientation has changed, the expression for η becomes

$$\eta \approx d_{31} E_f L \,. \tag{4}$$

In this case, the width is six times greater. Since Q is one-third of the Q for the 15-MHz mode, R_1 is expected to be half of the previous value (see Table 4.1).

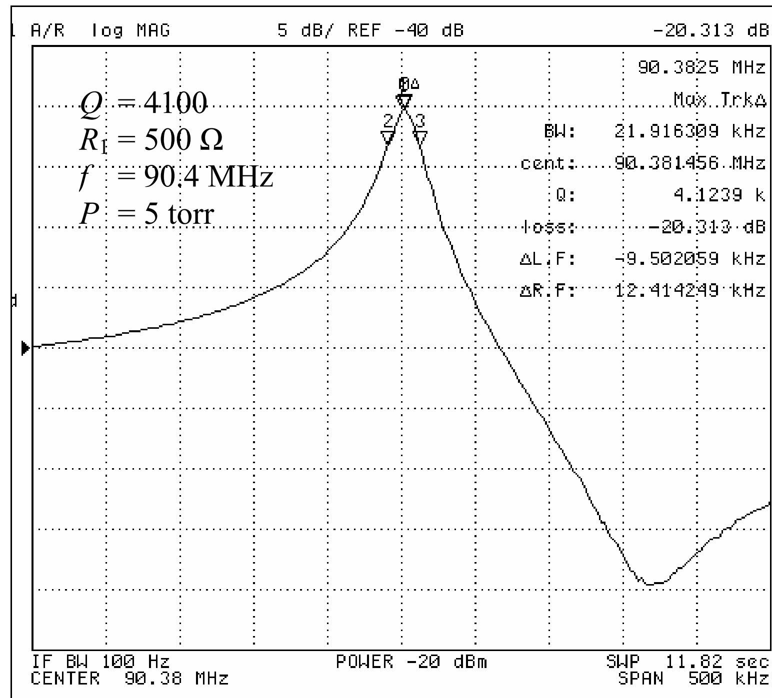

Figure 4.5 Frequency response of the 90-MHz width-extensional mode at 5 torr.

The reduced quality factor of 4100 is attributed to increased acoustic loss into the substrate. A quality factor of 3400 was also measured from the same device at atmospheric pressure. The results from modal analysis of the resonator in ANSYS (Figure 4.6) show elastic coupling between the resonator and anchors which is limiting the quality factor. Along the mid-plane of the resonator, the strain of the piezoelectric film (at the top surface) from dilation is opposing the phase of the flexural contribution. Notice that the strain in other regions has additive contribution from the flexural and extensional modes. The electrodes are disposed in the regions with additive contribution (Figure 4.7) and have lower R_1 than predicted from the 1D model (Table 4.1).

Table 4.1 Fundamental-mode CBAR analysis and measurement summary.

<table>
<tr><th colspan="3">Dimensions</th><th>ANSYS</th><th colspan="5">Measurement</th><th colspan="3">1D Model</th></tr>
<tr><th>$L \times w$ [μm]</th><th>w_e [μm]</th><th>L_e [μm]</th><th>Freq. f_0, [MHz]</th><th>Freq. f, [MHz]</th><th>Press [torr]</th><th>Q_l</th><th>A_V [dB]</th><th>R_1 [Ω]</th><th>k_n [N/m]</th><th>η [N/V] [C/m]</th><th>R_1 [Ω]</th></tr>
<tr><td rowspan="4">240×40</td><td rowspan="2">18</td><td rowspan="2">220</td><td rowspan="2">15.3</td><td rowspan="2">14.9</td><td>5</td><td>11800</td><td>-30.3</td><td>1600</td><td rowspan="2">5.4×10^5</td><td rowspan="2">2.1×10^{-5}</td><td>1100</td></tr>
<tr><td>760</td><td>6100</td><td>-36.3</td><td>3200</td><td>2200</td></tr>
<tr><td rowspan="2">220</td><td rowspan="2">18</td><td rowspan="2">91.6</td><td rowspan="2">90.4</td><td>5</td><td>4100</td><td>-20.3</td><td>500</td><td rowspan="2">2.0×10^7</td><td rowspan="2">1.2×10^{-4}</td><td>600</td></tr>
<tr><td>760</td><td>3400</td><td>-21.8</td><td>600</td><td>700</td></tr>
</table>

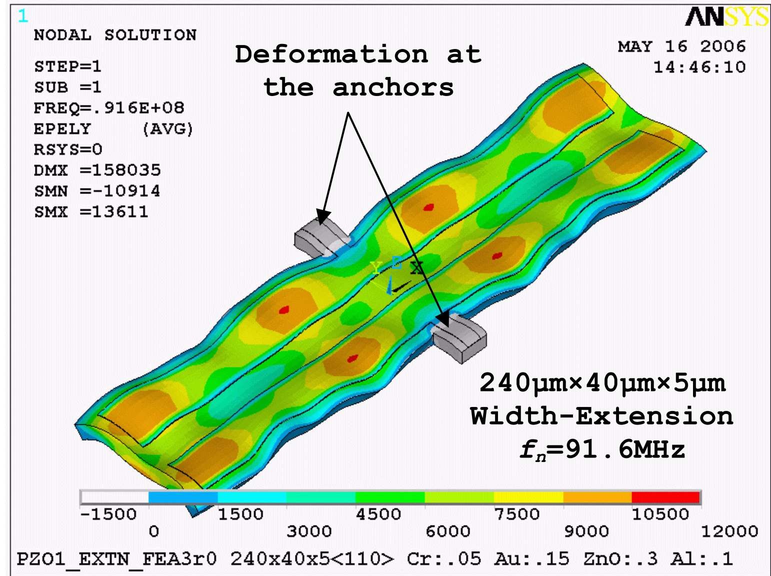

Figure 4.6 ANSYS modal analysis results for the width-extensional mode indicating a response in the anchor.

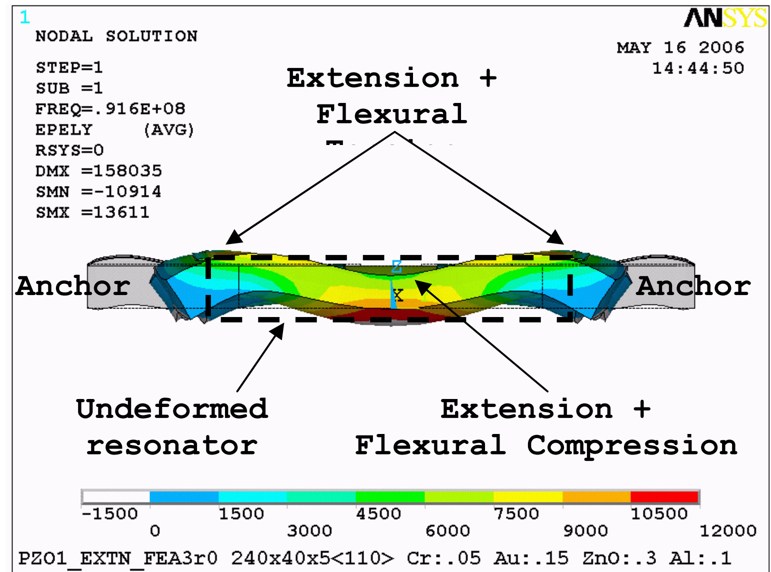

Figure 4.7 ANSYS results indicating coupling of the width-extensional mode with a flexural mode (end view). The strain at the top surface is of primarily importance.

A sweep of the frequency response from dc to 100 MHz indicates that the greatest transmission is from the 90-MHz resonance (Figure 4.8). Despite the lower Q in this mode, the transmission remains 10 dB greater than the 15-MHz resonance. Spurious modes with low Q are also present. In these resonators, the greatest Q is always measured from the bulk extensional modes, especially when operated at pressure levels above 1 torr. Since there is sufficient frequency isolation of the desired 90-MHz resonance from spurious modes and the 15-MHz mode, further suppression of these modes is possible with filtering.

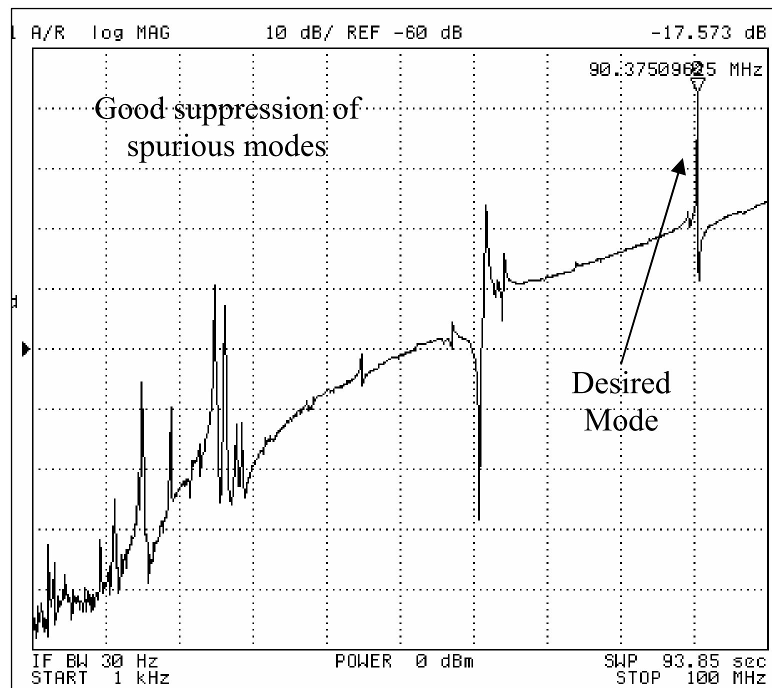

Figure 4.8 Frequency response from dc to 100 MHz showing greatest transmission from the 90-MHz mode.

4.1.3 Linearity

To characterize the linearity of the resonator, the response from varying the drive-level was observed. We define the saturation limit at the 1 dB compression point. P_R for the resistive divider is given by:

$$P_{\mathrm{R}} \approx P_1 + \frac{A_V}{2} \quad [\mathrm{dB}] \tag{2.28}$$

The 1 dB compression point in the 15-MHz mode occurs with P_1 of 0 dBm (Figure 4.9). For this condition, the resonator absorbed power is -15.5 dBm and the rms output current is 130 μA (Table 4.2). The observed rms current is approximately 50% of the predicted maximum value. The constraint is not fully understood, but is believed to be material limitations in the transduction film in combination with the mode shape. Beyond 0 dBm input power, a spring stiffening effect is observed as the nonlinear frequency response bifurcates. Devices have restored performance when the test port power is reduced.

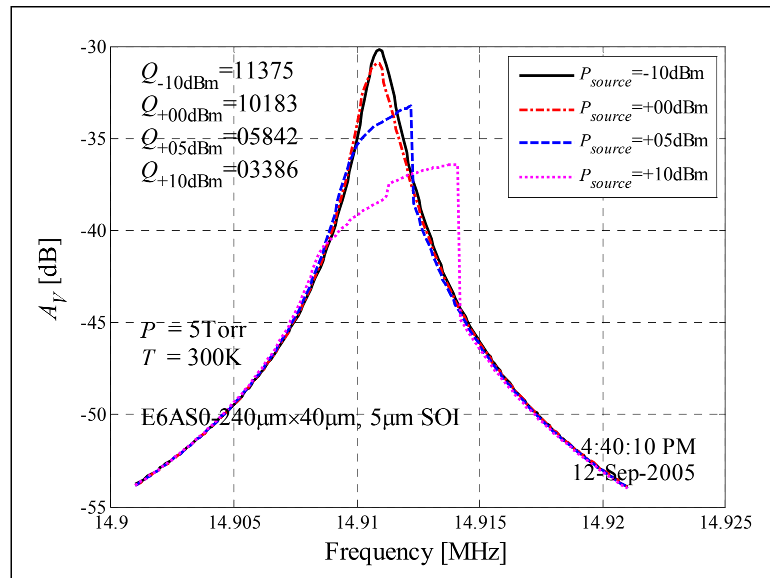

Figure 4.9 Response of the 15-MHz resonance in vacuum with various drive levels.

The 1 dB compression point of the 90-MHz mode is at P_1=10dBm and P_R=-0.5 dBm (Figure 4.10). The rms output current of 1.3 mA matches well with the predicted maximum $I_{2,max}$ of 1.5 mA. The downward shift in frequency at greater drive levels are caused by geometric and material nonlinearities in silicon. The saturation effect observed in this mode more closely matches expectations than the 15-MHz mode. The linearity measurements also exemplify the quality of the ZnO film since dielectric breakdown [59] was not observed for a 15 dBm input (in which the peak field is 6×10^6 V/m).

Table 4.2 Fundamental-mode CBAR linearity data.

Mode		15 MHz	90 MHz
$P_{1,max}$	dBm	0	10
Transmission, A_v	dB	-31	-21
$P_{R,max}$	dBm	-15.5	-0.5
Motional resistance, R_1	Ω	1600	500
Measured rms current, I_2	mA	0.13	1.3
Theoretical max. rms current, I_2	mA	0.26	1.5

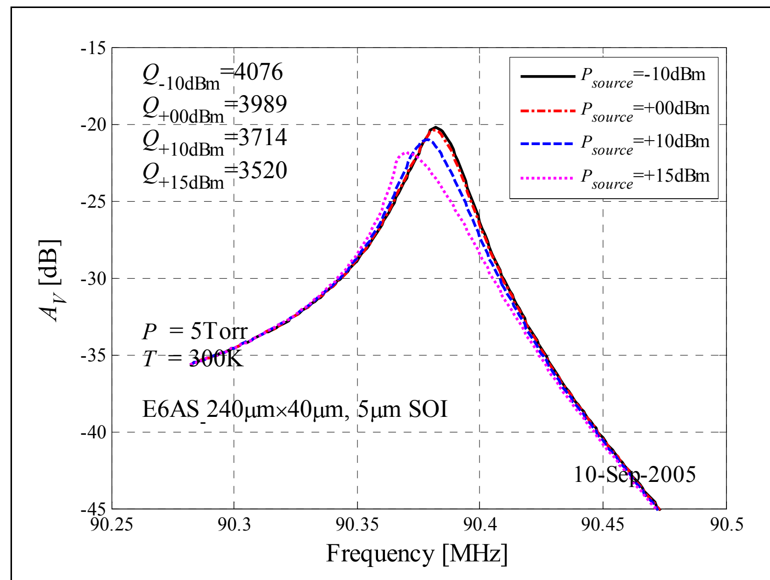

Figure 4.10 Response of the 90-MHz resonance in low vacuum with various drive levels.

4.2 High-Order Modes

High-order modes are presented for further reduction in R_1 for RF applications. For an nth-mode device, the impedance is ideally decreased by a factor of n. The structure in Figure 4.11 is a fifth-order resonator or simply a resonator with five times the electrode width. The simulated mode-shape in Figure 4.12 shows the regions with in-phase stress. Coupling efficiency is also determined by the mode shape. For an ideally-coupled resonator, the motional impedance is

$$R_1 \approx \frac{n}{n^2-1} \frac{\pi\left(t_{\mathrm{Si}}+t_{\mathrm{f}}\right)\sqrt{E_i \rho}}{2 d_{31}{}^2 E_{\mathrm{f}}{}^2 w Q} \tag{4.5}$$

for odd n, when n>1 (see Appendix A.11.2). As in the fundamental mode, impedance is determined by electrode width w and not the length. In addition to lower R_1, a high-order mode resonator provides improved dimensional control. The frequency sensitivity to lateral dimensional variations is reduced by a factor of n in an nth-order resonator.

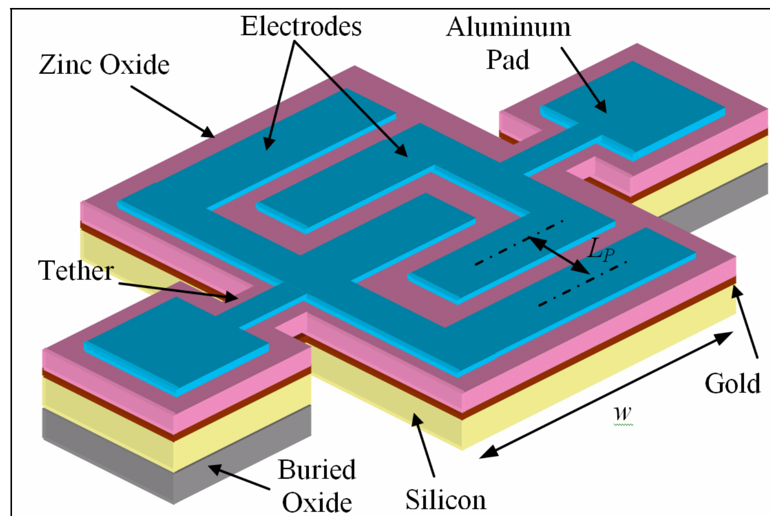

Figure 4.11 High-order composite piezoelectric-on-silicon micro-mechanical bulk acoustic resonator.

The CBAR in Figure 4.13 was fabricated with the five-mask process. It has a finger pitch of 10μm and has lateral dimensions of 90μm×160μm.

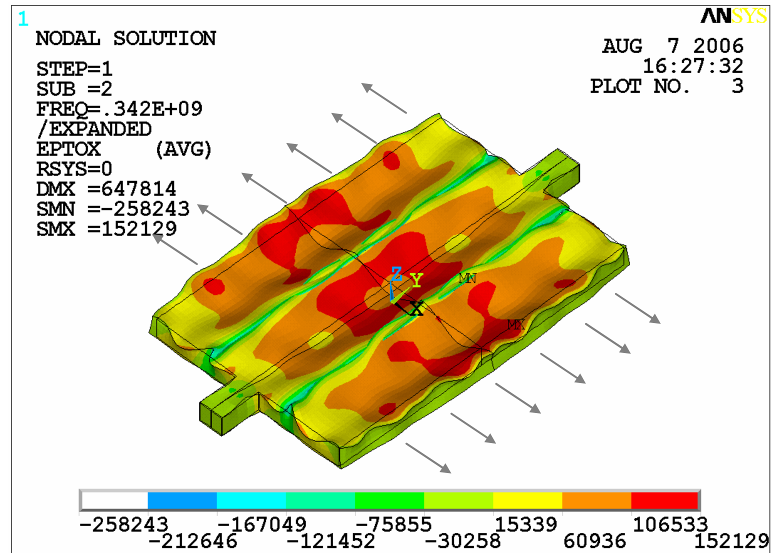

Figure 4.12 Simulated mode shape of a fifth-order ZnO-on-SCS CBAR with a finger pitch of 10 μm.

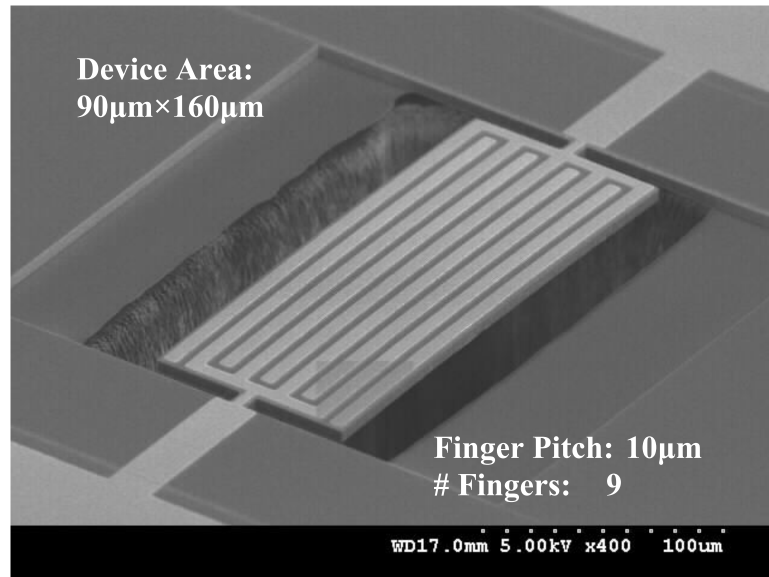

Figure 4.13 SEM of a 90μm×160μm CBAR with L_P=10μm.

The 9th-mode CBAR in Figure 4.13 has a resonance frequency of 373 MHz and exhibited an unloaded quality factor of 2000 at atmospheric pressure (Figure 4.14). Higher Q is expected at lower pressures. To measure unloaded Q, the port conversion feature of the E5071B was utilized to simulate a termination of 0.5 Ω. The insertion loss of 35 dB at resonance corresponds to 55 Ω device impedance. This is also verified by the 35 dBΩ impedance measurement (Figure 4.15). The isolation level of 30 dB is remarkable. Nonlinear responses (as observed in the fundamental mode) were not measured in these devices.†

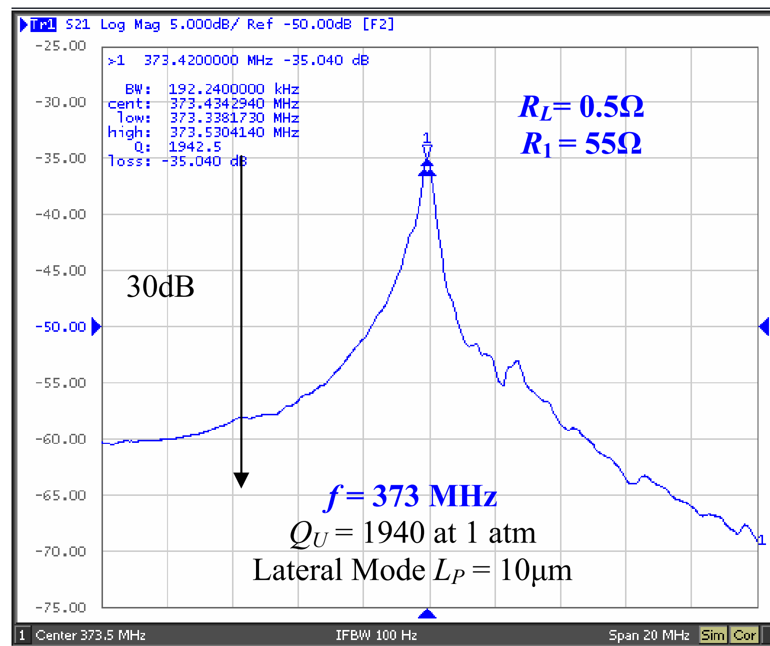

Figure 4.14 Frequency response of a ninth-order resonator with L_P=10μm at 1 atm.

† Test port power of 10 dBm was specified in the Agilent E5071B network analyzer. It was later determined that the actual test port power was 30 dB lower due to a hardware problem.

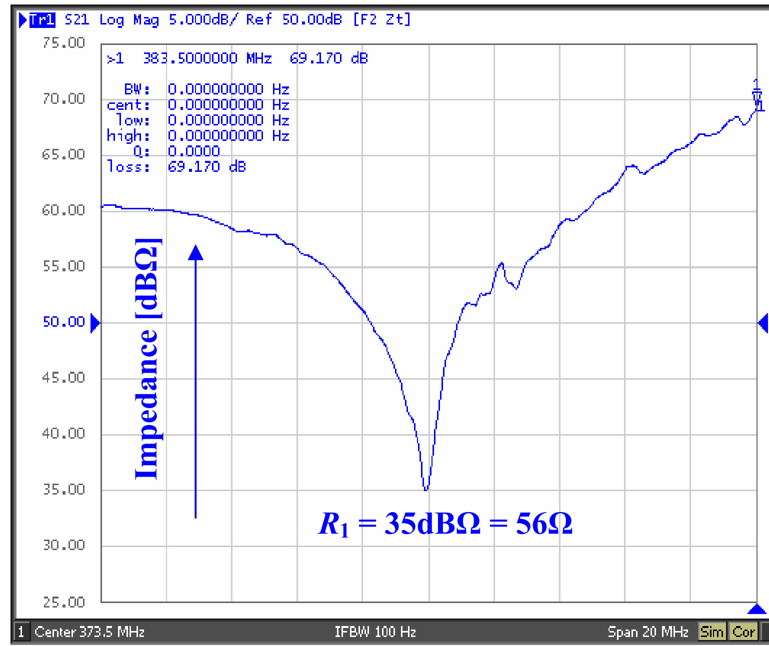

Figure 4.15 Impedance of a ninth-order resonator with L_P=10µm at 1 atm.

To enable higher-frequency resonators, the finger pitch is reduced. A 75µm×80µm CBAR with L_P=5µm is shown in Figure 4.16. Its resonance frequency is 640 MHz and its impedance is 400 Ω (Figure 4.17). The reduced Q of 740 (at atmospheric pressure) is primarily attributed to anchor losses. As the frequency and the number of electrode fingers are increased, the importance of optimizing the structure for the desired mode is escalated.

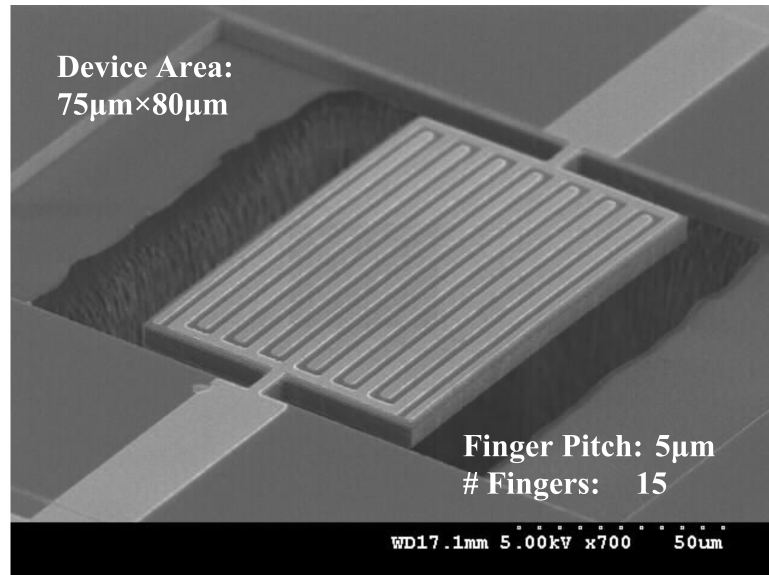

Figure 4.16 SEM of a 640-MHz CBAR (L=75µm, w=80µm).

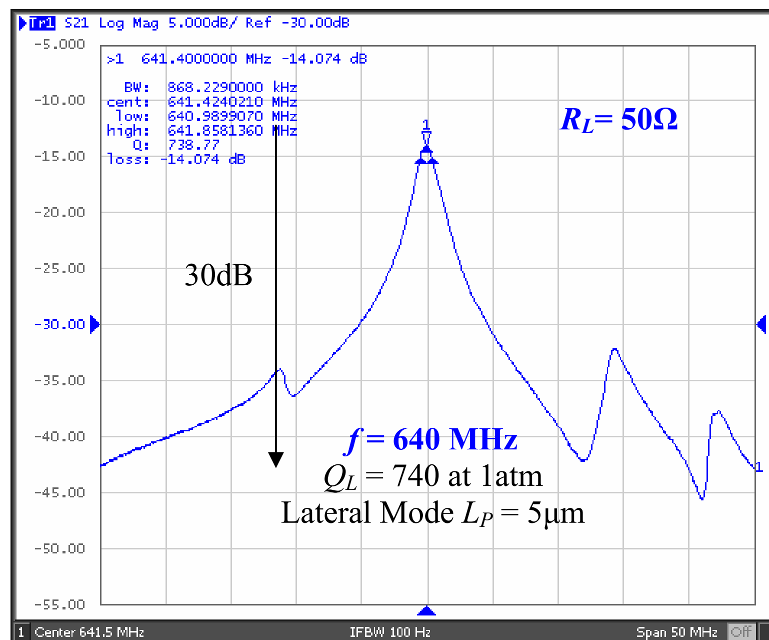

Figure 4.17 Frequency response of a 640-MHz CBAR with L_P=5µm at 1 atm.

One attractive feature of the presented work is the ability to fabricate thickness mode resonators next to the lateral CBAR. Resonators on the same substrate exhibited thickness-mode resonance at 2.5 GHz and quality factors of 1200 (Figure 4.18). Greater than 30 dB isolation is also observed in this mode. An important aspect of piezoelectric resonator design is mode isolation. Thorough analysis is required to ensure undesired extensional modes and flexural modes are suppressed.

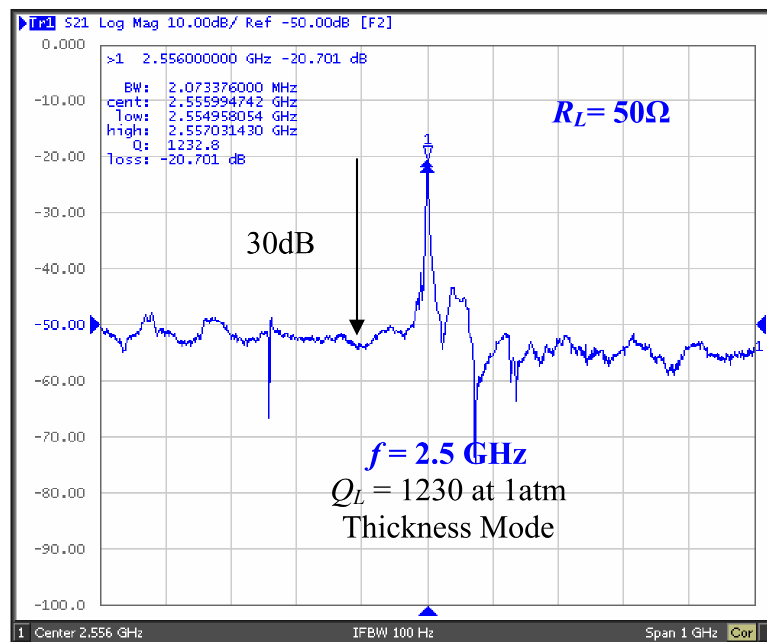

Figure 4.18 Frequency response of a thickness mode resonator fabricated on the same substrate as the CBARs.

CHAPTER 5 CAPACITIVE TUNABLE HF IBARs

The I-shaped bulk acoustic resonator (IBAR) is presented as the choice resonator for a temperature-compensated reference oscillator in the HF band. Beam resonators above 1 MHz have small electrode area and their Q is limited by anchor losses [57]. Higher-frequency bulk-mode resonators provide high Q and excellent linearity, but their electrostatic tunability is limited.

The IBAR provides tuning, high Q, low R_1, and a unique geometry enabling process compensation. Two typical techniques to increase electrostatic tuning are large V_P and small gaps. These techniques not only place additional demands on the interface circuit and fabrication process, but also increase the electrostatic stiffness nonlinearities. In the IBAR, tuning is provided through a reduced dynamic stiffness. The enabling IBAR geometry is a combination of an extensional resonator and flexural beams (Figure 5.1).

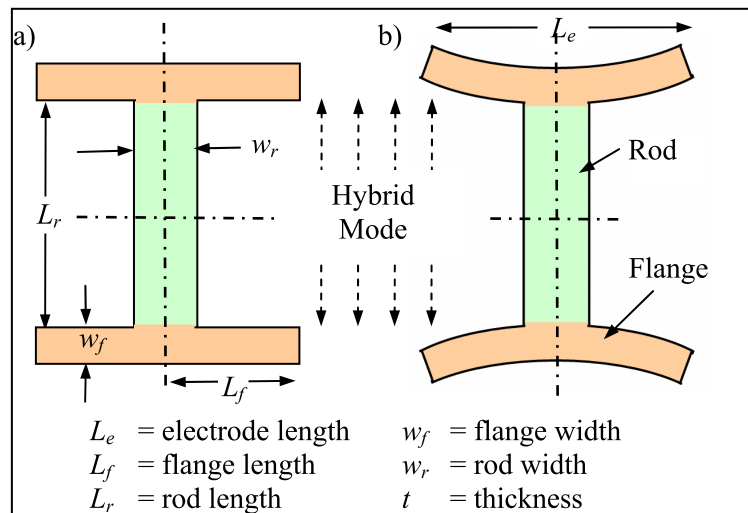

Figure 5.1 The I-shaped bulk acoustic resonator (IBAR) designed for high tunability and high Q, a) undeformed and b) in the desired mode.

5.1 Basic Modeling and Classification

The normalized stiffness, electrostatic tuning, R_1, and Q of an IBAR[*] can be predicted from a simple model (Figure 5.2). The desired mode in the IBAR has both degrees of freedom (DOF) in phase. The other mode(s) are suppressed since out-of-phase responses have poor coupling. Three classifications of IBARs are defined: the Q-enhanced (QE), compliance-enhanced (CE), and semi-compliant high-Q (CQ) designs. The first two classifications can be described using Dunkerley's equation.

$$\frac{1}{\omega_1^2} \approx \frac{1}{\omega_i^2} + \frac{1}{\omega_j^2} \tag{5.1}$$

If one DOF is substantially lower frequency, it governs the fundamental frequency of the device and the mode shape. The extreme QE and CE IBARs follow this. Mode shapes of CQ IBARs are a combination of both DOF.

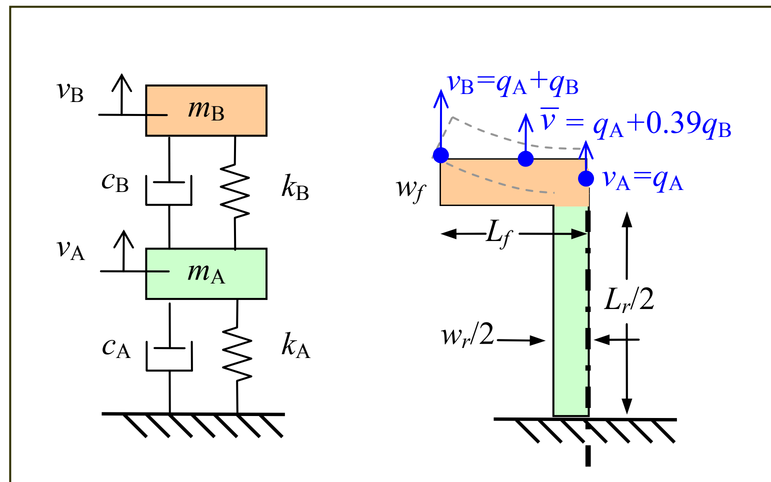

Figure 5.2 2-DOF mechanical model of an IBAR.

[*] Semantically, "IBAR" is not entirely accurate since the mode is not present in the bulk.

For geometries in which the flange acts as a rigid body (*i.e.*, $\sqrt{(k_B/m_B)} >> \omega_n$), the mode is primarily extensional and contained in the rod. If material losses are dominant, the quality factor of the resonator can be greater than the constituent components since the flange acts as an energy storage element (Appendix A.8). These are geometries are *Q*-enhanced (*Q*E) IBARs. The natural frequency of QE IBARs can be approximated as

$$\omega_n \approx \sqrt{\frac{k_A}{m_A + m_B}} \tag{5.2}$$

At the other extreme, flange flexing is predominant. In these modes, the normalized stiffness k_n/A_e is significantly lower than extensional mode resonators at the same frequency. These are compliance-enhanced (CE) IBARs. The flange operates as a flexural beam having improved linearity (since there is no spring hardening from tension) and greater *Q*. For CE IBARs,

$$\omega_n \approx \sqrt{\frac{k_B}{m_B}} \tag{5.3}$$

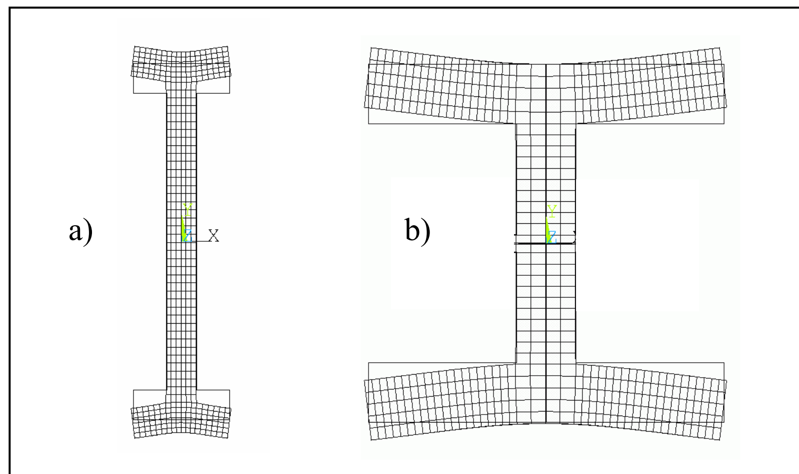

Figure 5.3 a) A *Q*-enhanced IBAR, and b) a compliance-enhanced IBAR.

5.2 Normalized Stiffness

Since the electrostatic tuning coefficient and motional impedance are dependent on the normalized dynamic stiffness, this section is devoted to its analysis. The most convenient method to describe the normalized stiffness of an IBAR is given by

$$\left(\frac{k_n}{A_m}\right)_{IBAR} = c_r^{-1}\left(\frac{k_n}{A_m}\right)_{SiBAR} \tag{5.4}$$

in which c_r is the relative compliance between the IBAR and a 1D extensional resonator. This approach is convenient since the k_n/A of a 1D resonator is proportional to the f_n and is approximately 0.195 PN/m^3/MHz. CE IBARs are essentially flexural modes and have the highest c_r of the three classifications. Figure 5.4 represents the upper bounds of c_r found through FEA for several flange thicknesses. Essentially, Figure 5.4 describes how much more tuning a CE IBAR can have compared to an extensional resonator.

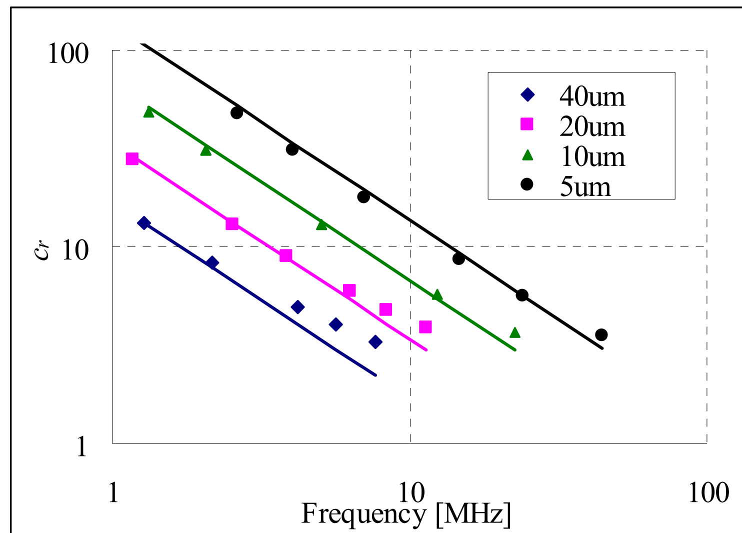

Figure 5.4 Relative compliance limit of CE IBARs with two electrodes to extensional resonators for w_f=[5,10,20,40] µm.

5.3 Multi-Section IBARs

IBARs can be mechanically connected in parallel to further reduce R_1 and improve linearity. Changes in the normalized stiffness are generally insignificant. Finite element analysis of a 6-MHz two-section IBAR predicts the mode shape in Figure 5.5. The displacement along the flange is far greater than the displacement at the end of the rod, representative of a compliance-enhanced mode.

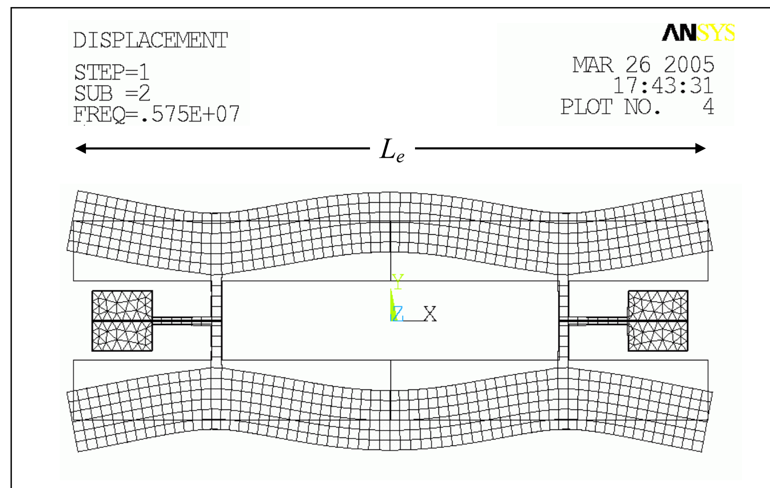

Figure 5.5 Mode shape of a two-section 6-MHz CE IBAR.

5.4 Analysis and Characterization

A two-section 6-MHz IBAR having 180-nm gaps fabricated with the HARPSS-on-SOI process is shown in Figure 5.6. The predicted frequency is 5.75 MHz. The FE model gives a k_n/A of 0.204 PN/m^3. The relative compliance is 5.5 and the predicted tuning coefficient is -7.44 ppm/V^2.

IBARs were characterized with Experimental Apparatus A (Figure 2.9). The electrodes were biased at 1 V. A Q of 103000 was measured in vacuum with a polarization voltage of 3 V (Figure 5.7). Changes in quality factor were not observable over the pressure range of 0.1 torr to 1 μtorr. The gap size of 180 nm suits the design operational voltage range of 15-25 V. The theoretical predictions and measurements are summarized in Table 5.1.

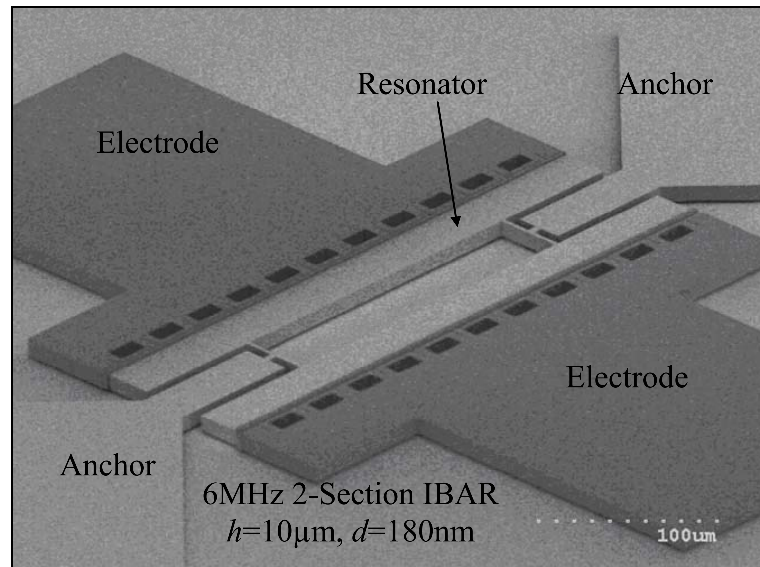

Figure 5.6 SEM of a 10-μm thick two-section IBAR with conservative 180-nm gaps fabricated using the HARPSS-on-SOI process.

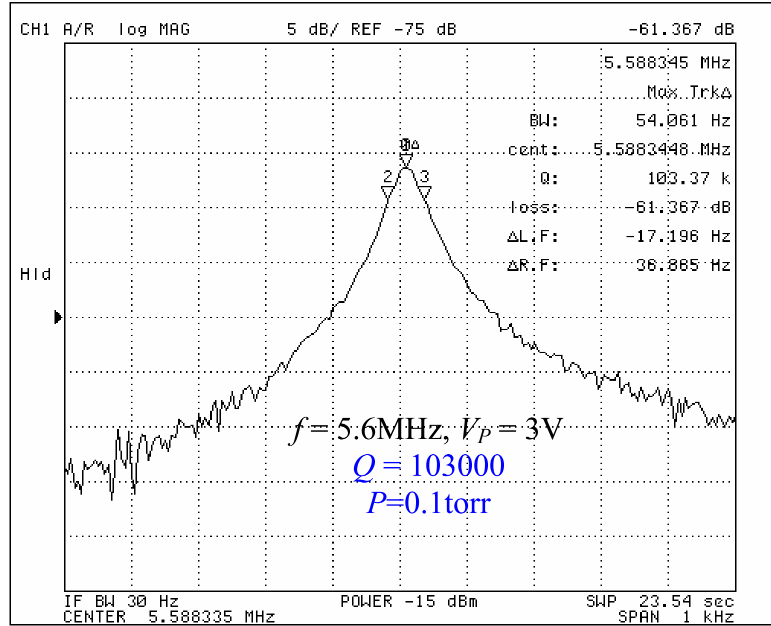

Figure 5.7 Frequency response of the 6-MHz two-section IBAR with V_P=3V and P=0.1torr.

Table 5.1 6-MHz IBAR specifications.

	Theoretical	Measured
Frequency	5.75 MHz	5.59 MHz
Unloaded Q	-	112000
k/A	0.204 PN/m^3	-
L_e, Electrode Length	320 μm	
d, gap size	180 nm	
For d = 180 nm		
- Impedance, V_P = 3 V - Impedance, V_P = 10 V - Impedance, V_P = 20 V	53 kΩ 2.6 kΩ 0.6 kΩ	58 kΩ 10.7 kΩ 6.8 kΩ
- Tuning coefficient, γ_e	-7.4 ppm/V^2	-7.9 ppm/V^2
For d = 65 nm		
- Impedance, V_P = 3 V	0.9 kΩ	-
- Tuning coefficient, γ_e	-170 ppm/V^2	-

The measured tuning, impedance, and quality factor characteristics of the IBAR are as expected. By tuning the voltage from 2 to 25 V, f_s is tuned by 4600 ppm (Figure 5.8). The measured tuning coefficient for this device is -7.9 ppm/V^2. The test impedance R_t is 6.8kΩ with V_P of 20 V, while the predicted impedance is 0.6 kΩ (Figure 5.9). A large part of R_t is a small-signal impedance R_{SS} of approximately 6.2 kΩ. In IBARs, R_{SS} and terminations reduce the loaded quality factor as R_1 is reduced (Figure 5.10).

$$Q_L = Q_U \frac{R_1}{R_1 + R_{SS} + R_S + R_L} \tag{5.5}$$

R_{SS} of 0.5-5 kΩ and the Q_L dependence on V_P has been observed in other IBARs (Appendix B.2.2). It is a result of the finite conductance of the resonator body. Since typical capacitive resonators [13,14] have R_1 larger than several kΩ, R_{SS} is not commonly observed.[†]

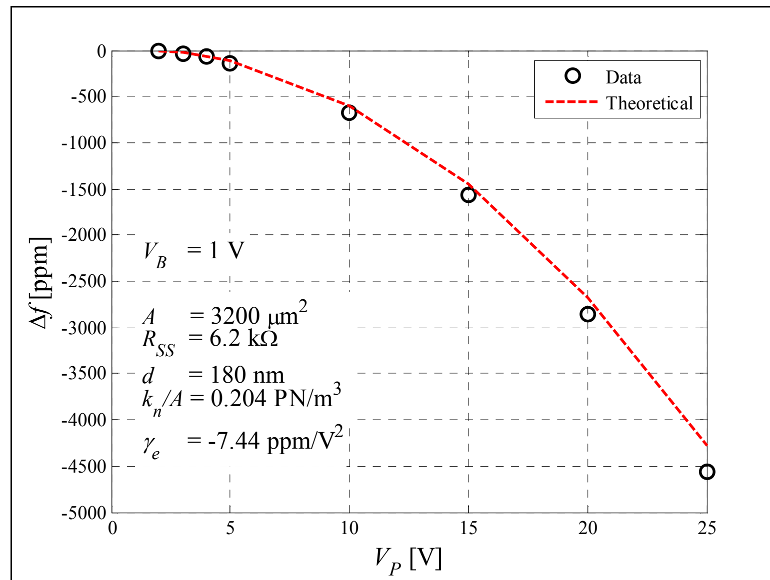

Figure 5.8 Measured and theoretical tuning characteristic of the 6-MHz IBAR over a V_P range of 2 to 25 V.

[†] The stabilized R_1+R_{SS} over a temperature compensation voltage range is advantageous for interfacing. This allowed the oscillator in Section 6.2 to operate over a large V_P range.

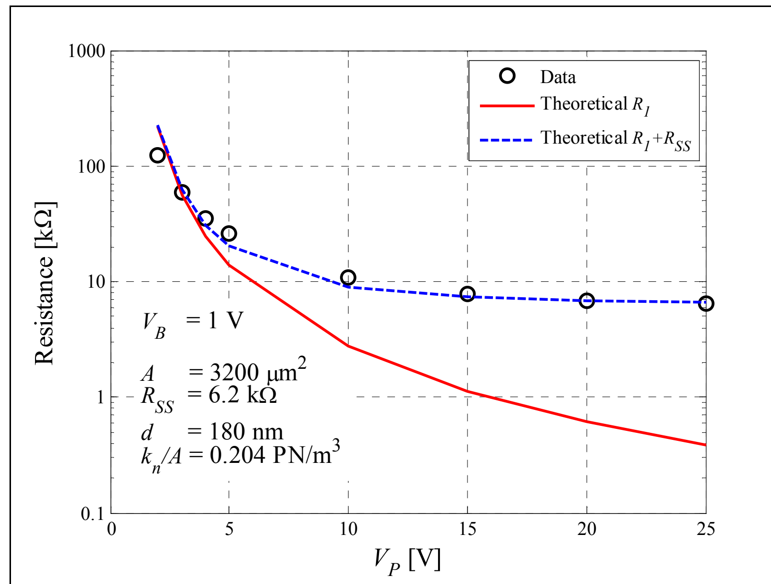

Figure 5.9 Measured and theoretical impedance of the 6-MHz IBAR over a V_P range of 2 to 25 V. The dotted line represents the predicted impedance accounting for R_{SS} of 6.2 kΩ.

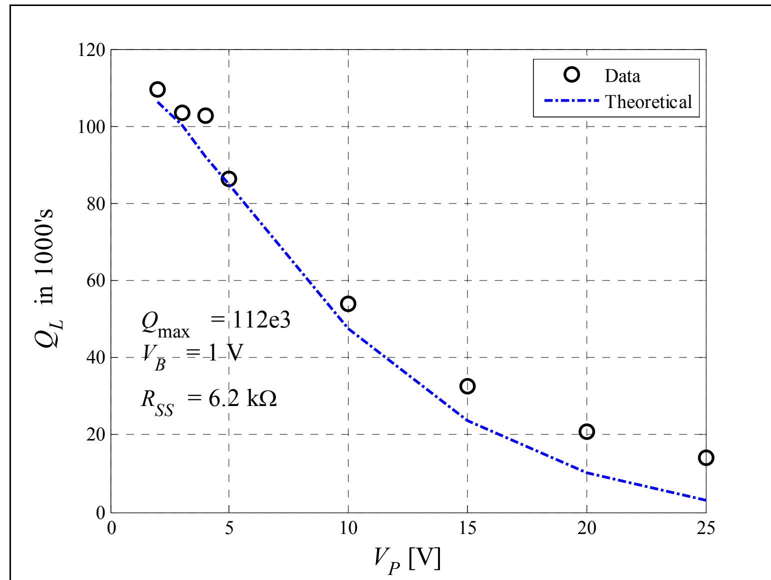

Figure 5.10 Measured and theoretical loaded Q of the 6-MHz IBAR over a V_P range of 2 to 25 V.

5.5 IBAR Design for Manufacturability

DFM for frequency accuracy is summarized for the three classifications of IBARs. Process-compensated designs for 10-MHz QE and CE IBARs are shown in Figure 5.11.‡ The frequency variation for these resonators is shown in Figure 5.12. For the QE design, the variation is [-25,0] ppm over a ±0.5 μm process bias range and has a negative curvature. The width of the rod and the thickness of the flange are 25 μm. The normalized stiffness is 0.65 PN/m^3, and the relative compliance is 3.0.

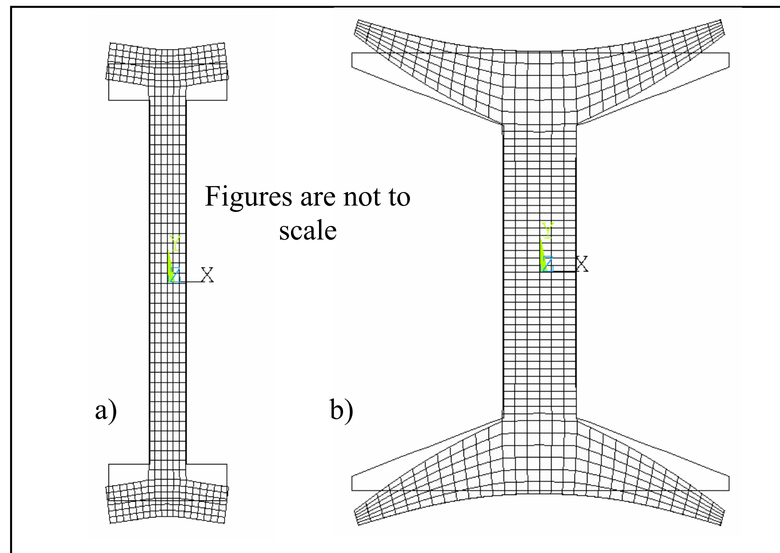

Figure 5.11 Process compensated geometries of a) a 10-MHz *Q*E IBAR and b) a 10-MHz CE IBAR.

‡ The completed analyses for the QE and CE IBARs are in Appendix A.9.

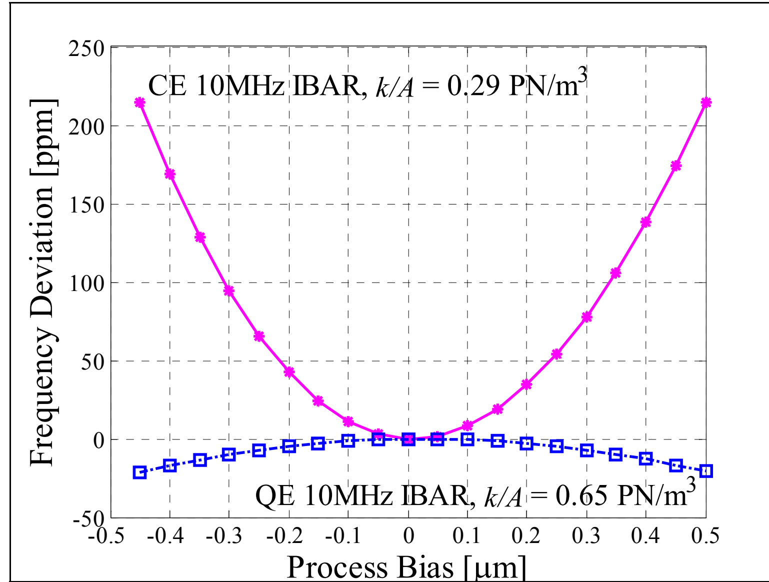

Figure 5.12 The frequency dependence of 10-MHz CE and QE process-compensated IBARs on process bias.

Recall that the natural frequency of the CE design is determined by the flange. A tapered flange is utilized for compensation. See Figure 5.11b. The 10-MHz PC CE IBAR has a normalized stiffness of 0.29 PN/m^3 and a c_r of 6.7. However, because the tip of the flange is small, the frequency variation is increased to [0,220] ppm for the bias range of ±0.5 µm. The CE design provides greater tuning at the cost of increased Δf.

Since the two previously presented IBARs are process-compensated using two different methods, combining their effect can potentially lead to a PC design with low Δf, good tunability, and Q enhancement. This concept is exercised in the geometry of Figure 5.13, in which the taper is reduced. Some extensional contribution is introduced to compensate. The new tapered 10-MHz IBAR is simulated to have less than 1 ppm Δf over the same process window (Figure 5.14).

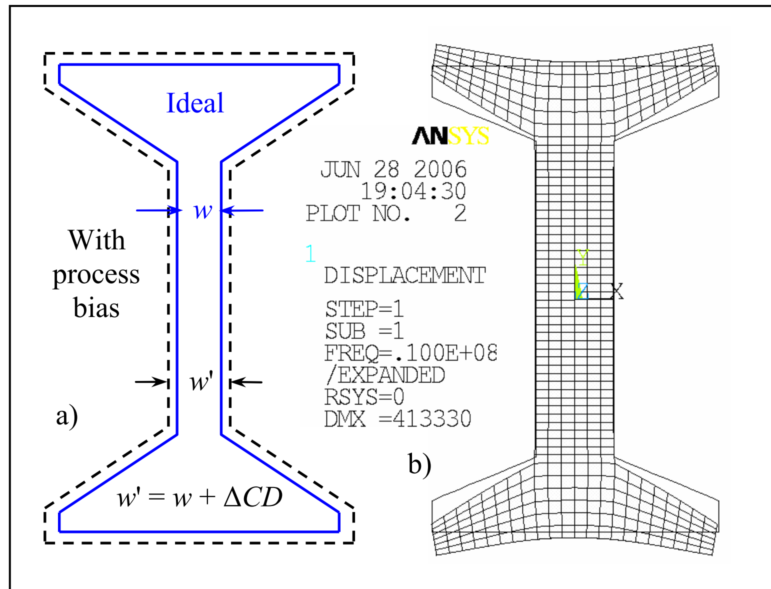

Figure 5.13 a) Process bias on a 10-MHz tapered IBAR, and b) the finite element model.

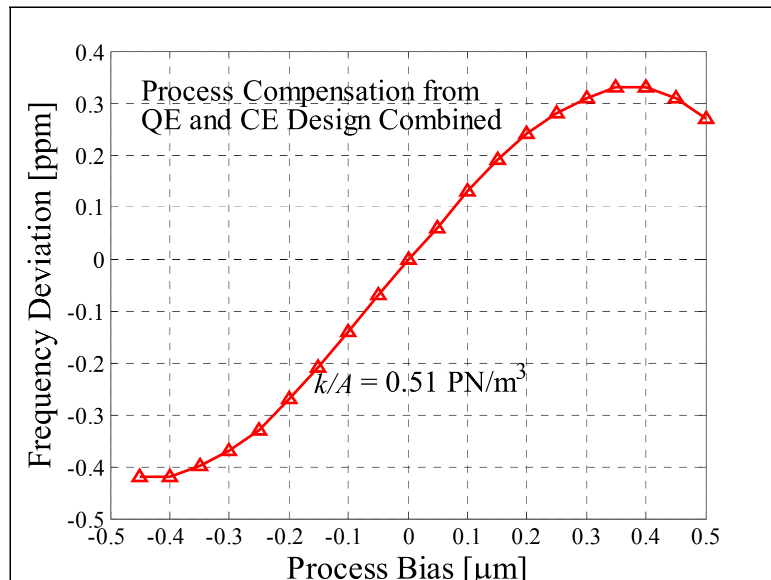

Figure 5.14 Simulated frequency deviation for [-0.5,0.5] μm process bias on an optimized tapered IBAR.

The frequency dependence on other variations was also simulated. For a thickness variation of ±1μm, the frequency variation is 46 ppm. For trench tilting of ±5° rotated along the *x*-axis and *y*-axis, the frequency variations are 160 ppm and 23 ppm, respectively. The finite element model for trench tapering is more difficult to build. Since trench tapering is symmetric and modes are substantially in the plane of the substrate, the effects may be nullified. Therefore, it is plausible that trench tapering will have similar or less effect than the asymmetric tilting.

To verify the optimized design, the dimensional variation due to process bias was replicated with e-beam lithography. Three resonators designs were drawn: a nominal 10-MHz IBAR with ideal geometry, one with -0.5 μm bias, and one with +0.5 μm bias. Devices were fabricated on a 10-μm n-type 0.002 Ω-cm SOI substrate (Figure 5.15). 500-nm capacitive gaps were dry etched in an STS DRIE tool. The frequency response from a typical IBAR (Figure 5.16) had an impressive quality factor of 170000 in low vacuum (5 torr). In high vacuum, quality factors of 250000 were measured (Figure B.15).

A handful of devices were characterized. The measured frequency variation across 41 resonators was within ±250 ppm and is dispersed (Figure 5.17). However, less than 25 ppm variation was observed in the mean frequencies of the three designs. Thus, random variations[§] contribute for most of the ±250 ppm variation and the design is indeed process compensated. Data from resonators having lower than 130000 *Q* were discarded due to cleanliness – particles on the surfaces also load the frequency.

[§] Thermal oxidation or hydrogen annealing of DRIE surfaces should reduce random variations.

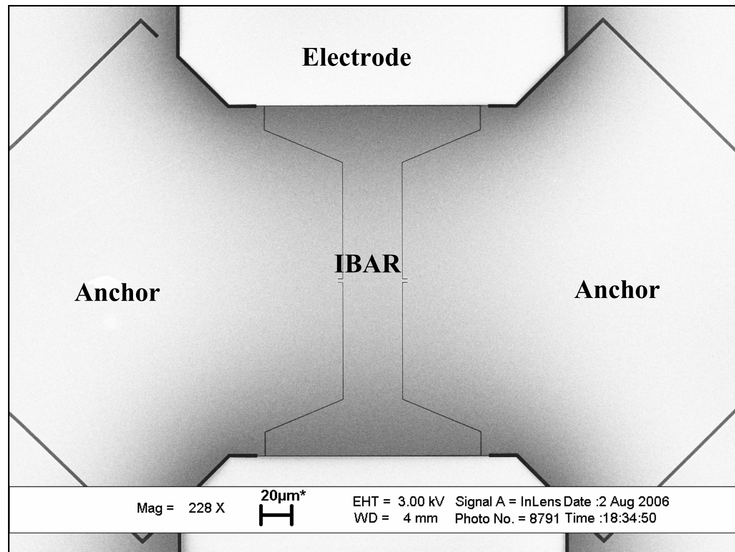

Figure 5.15 SEM of a 10-MHz optimized IBAR patterned with e-beam lithography, d=500nm (SOI thickness is 10 µm).

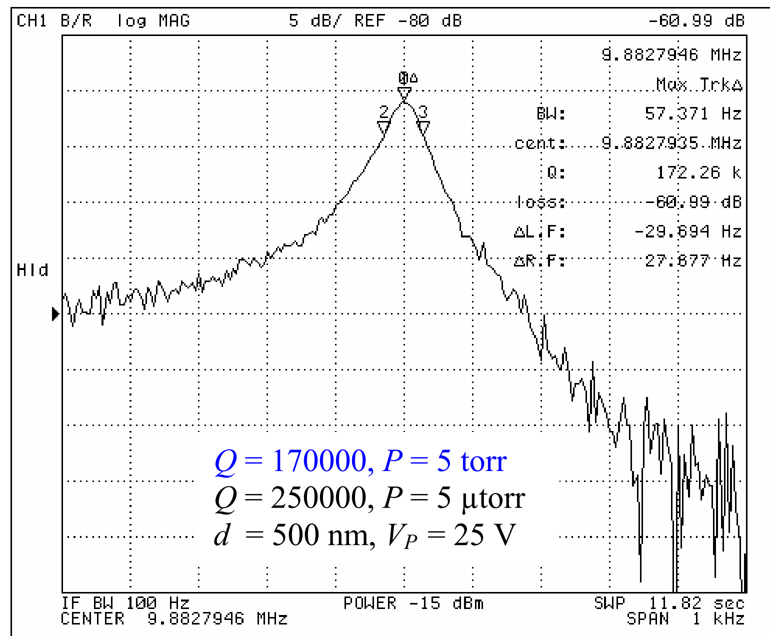

Figure 5.16 Typical frequency response of an optimized 10-MHz process-compensated IBAR in low vacuum.

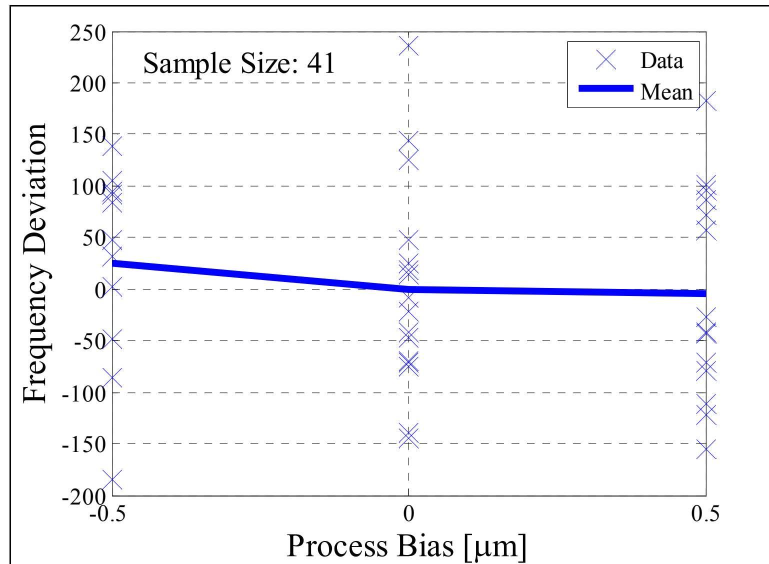

Figure 5.17 Measured frequency deviation from the ideal design and designs with skew. The deviation of the mean of each design is 25 ppm.

For comparison, the results compared to the largest possible 10-MHz resonator. An extensional-mode plate or disk resonator at 10 MHz has a primary dimension of 400 µm. The same ±0.5 µm process bias results in approximately 2500 ppm frequency variation for bulk-mode plates and disks.

Histograms of center frequency and Q are shown in Figure 5.18. The mean frequency from the 41 samples was 9.884 MHz. Inaccuracies in the material properties are the likely cause of the 1.2% frequency error. In practice, characterized substrates and precision tools to align to crystal axes would be available. Data from resonators having lower than 130000 Q were discarded due to cleanliness (since particles on the surfaces also load the frequency). Measurement data from all other resonators are reported.

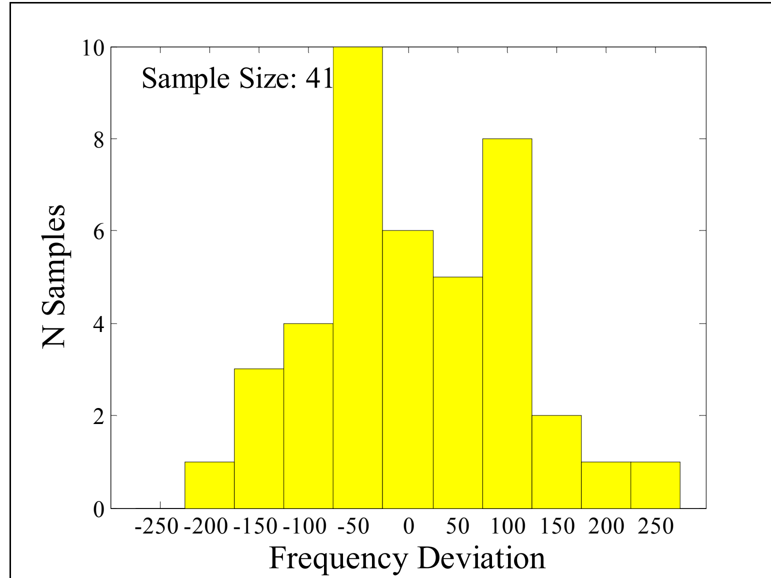

Figure 5.18 Histogram of natural frequency of the process-compensated IBARs.

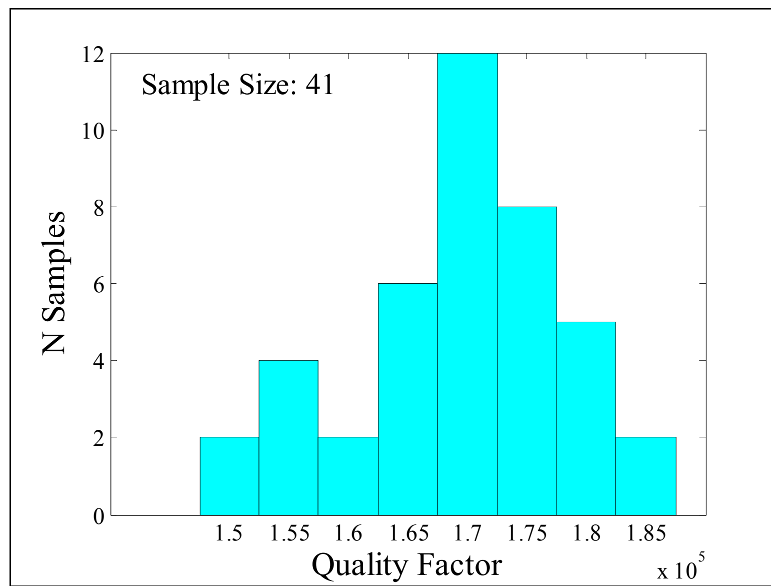

Figure 5.19 Histogram of Q of the process-compensated IBARs in low vacuum (P=5torr).

CHAPTER 6 REFERENCE OSCILLATORS

The described micromechanical resonators are best suited for oscillator applications having temperature stability requirements as tight as several ppm. Potential applications include consumer-grade timing references and some communications-grade timing references. Since temperature stability and phase noise typically determine the applicability, two different oscillators were implemented to serve as demonstrations of these metrics.*

* The work on reference oscillators was completed together with Krishnakumar Sundaresan. Dr. Sundaresan is responsible for all the circuit design.

6.1 100-MHz Temperature-Controlled SiBAR Oscillator

The SiBAR is the ideal micromechanical resonator for an ultra-low-phase-noise oscillator [60]. The *f-Q* product of SiBARs is the highest amongst the resonators investigated (Figure 1.3), enabling low close-to-carrier noise. Bulk-extensional modes in silicon can also have very large energy densities, leading to low noise floor. Since bulk-mode capacitive resonators have limited sensitivity to V_P, the voltage-tuning of C_1 is limited. However, resistive heating of the resonator can be used for tuning (Appendix B.1.3) and temperature-control[†]. The latter approach is used in the oscillator architecture in Figure 6.1.

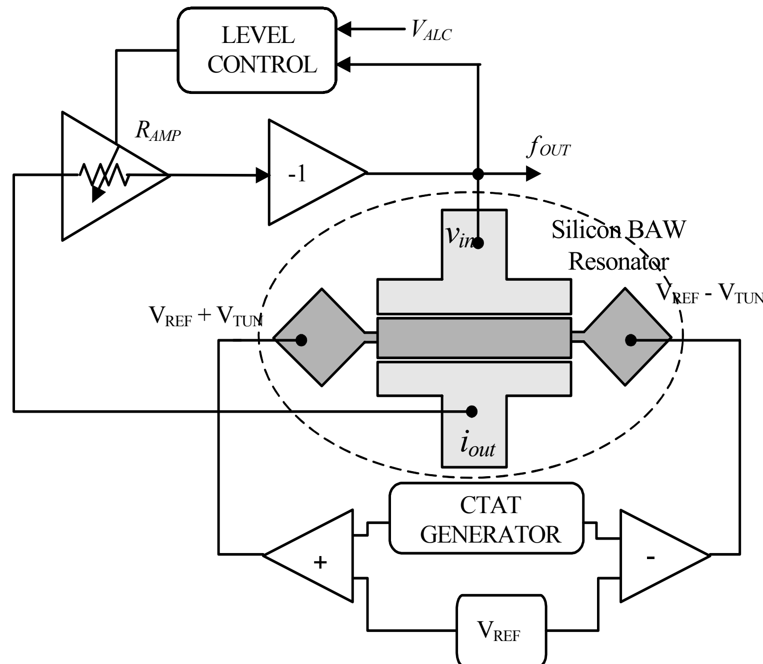

Figure 6.1 System diagram for the open-loop oven-controlled SiBAR oscillator.

[†] The required power for oven-control is expected to be significantly lower than an OCXO due to improved thermal isolation. The smaller thermal mass also has reduced warm-up time. However, to compete with an OCXO on temperature stability near 0.1 ppm, a turnover in the *f* vs *T* profile must be introduced.

The 103-MHz SiBAR in Figure 3.1 was wire-bonded to an ASIC containing the maintaining amplifier, level-control block, and temperature-control block. The SiBAR biased at the operating voltage of 25 V has an impedance of 3.3 kΩ and Q of 66000 (Figure 3.11). The temperature-controlled oscillator showed 56 ppm frequency variation over 100°C, which is a factor of 52 improvement compared to the uncompensated variation of 2980 ppm. The oscillator has a noise floor of -130 dBc/Hz beyond 100 kHz offset (Figure 6.3). At 1 kHz offset, the noise power is -108 dBc/Hz. The observation of the $1/f$, $1/f^2$, and $1/f^3$ regions is unexpected. Assuming the loaded Q is approximately 50000, the Leeson frequency is 1 kHz, below which the $1/f$ flicker should be up-converted to a $1/f^3$ region. It is likely that mechanisms relating to capacitive transduction generate $1/f^2$ and $1/f$ noise that dominate those regions. Nonetheless, the measured phase noise is a baseline for further improvement.

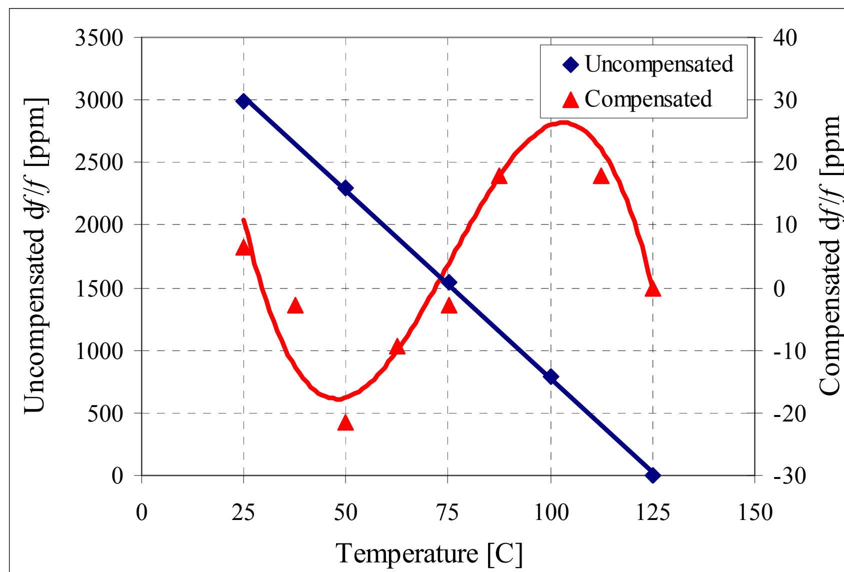

Figure 6.2 Temperature stability of a 103-MHz temperature-controlled SiBAR oscillator.

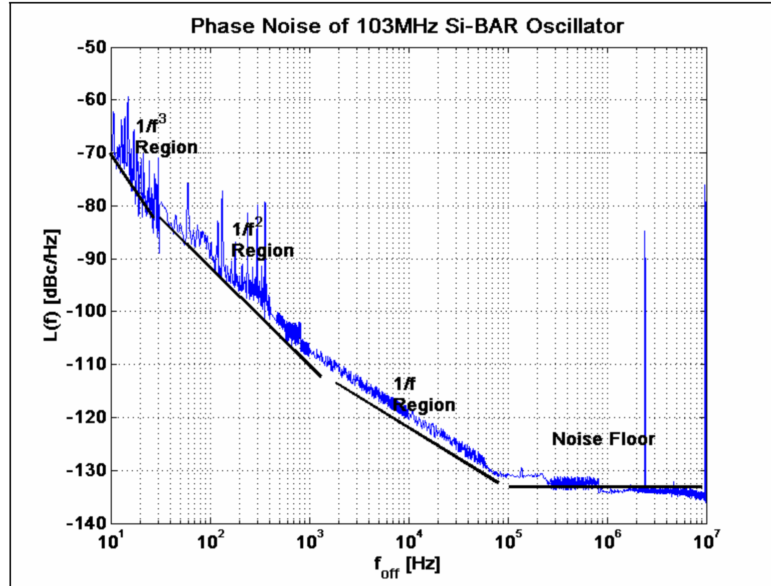

Figure 6.3 Single-sideband phase noise of a 103-MHz SiBAR oscillator.

Table 6.1 Specifications for the 103-MHz SiBAR oscillator.

Resonator Specifications	
Resonant Frequency	103 MHz
Open loop quality factor 5V bias 25V bias	 90000 66000
Motional Resistance 5V bias 25V bias	 50 kΩ 3.3 kΩ
Oscillator Specifications	
Total power consumption Sustaining amplifier Buffer Driver Temp. Comp. Circuit Temp. Comp. Buffer	 2.6 mW 19 mW 0.3 mW 170 mW
Die area (excluding test circuits)	1.1 mm^2
Temp. stability over 100°C Uncompensated variation w/ Compensation	 2980 ppm 56 ppm
Phase Noise performance 1 kHz offset Phase Noise floor	-108 dBc/Hz -136 dBc/Hz
Integrated jitter (100Hz–10MHz)	72 ppm

6.2 6-MHz Temperature-Compensated IBAR Oscillator

Electrical tuning in the IBAR provides a means to compensate the temperature coefficient of resonators. Varying the bias voltage can provide 4000 ppm frequency tuning or more (Figure B.12 and Figure 5.8). This feature is utilized in the IBAR oscillator architecture in Figure 6.4. The oscillator consists of a maintaining amplifier with inversion.[‡] Level control is used in limiting the transimpedance gain to maintain resonator operation in the linear regime. The bias generator applies a temperature-dependent V_P to compensate the intrinsic frequency dependence on temperature. Since electrical tuning is reversible, this approach has excellent potential for good retrace (*i.e.*, minimal hysteresis) in the frequency-temperature profile.

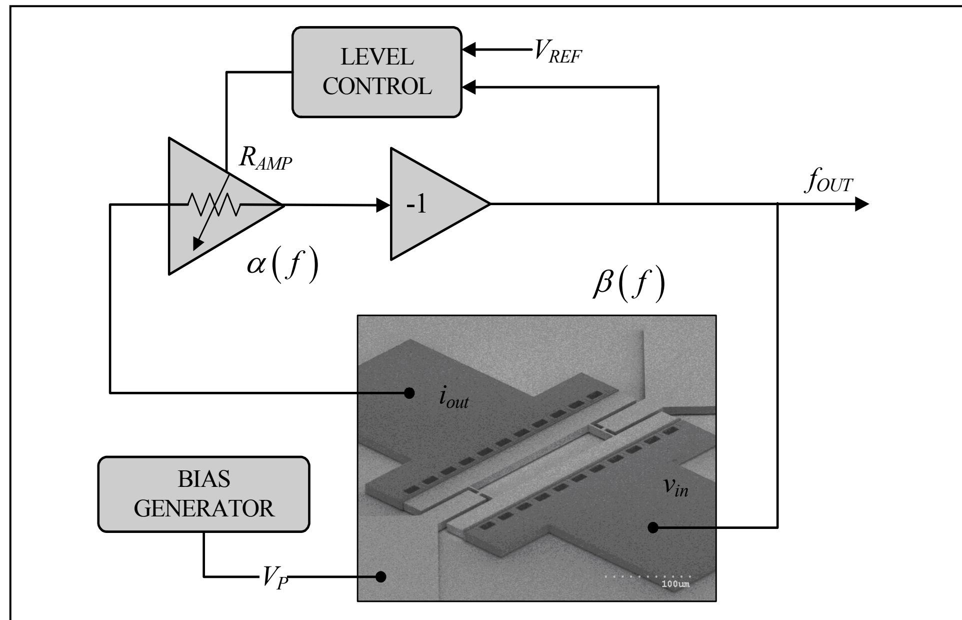

Figure 6.4 Architecture of the temperature-compensated IBAR oscillator.

[‡] Symmetric mode resonators have π phase shift that is not represented in the simplified equivalent circuit.

The intrinsic and compensated frequency-temperature profiles are shown in Figure 6.5. The natural frequency f_n has an approximate linearized slope γ_T of -28 ppm/K. The minimum V_P is applied at the maximum operating temperature, and vice versa. To maintain a constant f_r, the bias voltage follows the expression

$$V_{Pi}^{\ 2} \approx A - \frac{\gamma_T}{\gamma_e} \cdot (T - T_0) \tag{6.1}$$

in which A is used for calibration and γ_e is the electrostatic tuning coefficient. (See Appendix A.10). The IC containing all the functional blocks is discussed in [61]. A linear bias generator was also implemented for comparison purposes.

The 6-MHz IBAR in Figure 5.6 was interfaced to the IC. The measured intrinsic temperature variation is 2830 ppm over the range of 25°C to 125°C (Figure 6.6). The stability improved to 334 ppm with linear compensation and was further improved to 39 ppm with parabolic compensation.

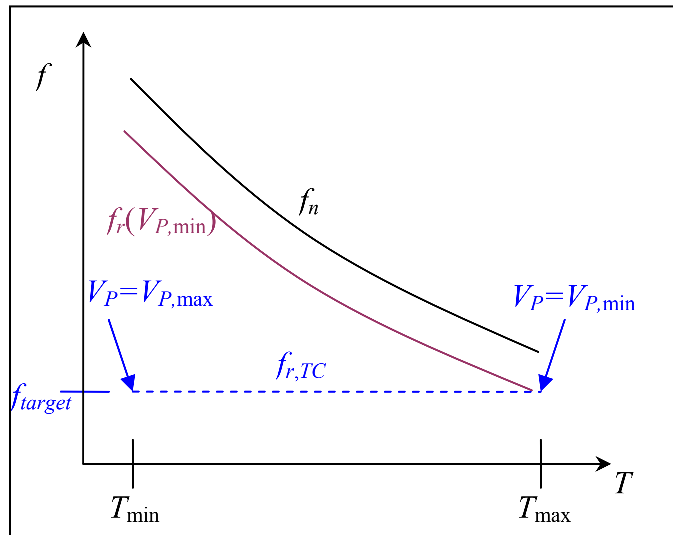

Figure 6.5 Typical temperature dependence of resonator natural frequency f_n, resonance frequency at minimum V_P, and the desired temperature-compensated characteristic.

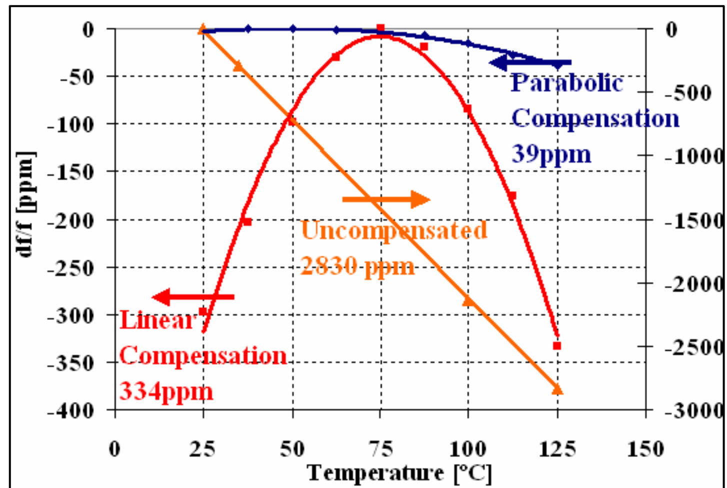

Figure 6.6 Intrinsic, linearly-compensated, and parabolically-compensated temperature stability for a 6-MHz IBAR oscillator over a range of 100°C.

Phase noise measurements (Figure 6.7) were made with an Agilent E5500 analyzer. The IBAR was biased at 3 V with an external supply to investigate the close-to-carrier noise. A low V_P was used since the quality factor in the available IBARs is minimally loaded with this condition. The phase noise is -90 dBc/Hz at 100 Hz offset and -110 dBc/Hz at 1 kHz offset. The far-from-carrier phase noise of the oscillator with ALC is -135 dBc/Hz. The effect of resonator non-linearity on phase noise has not been thoroughly studied. If larger V_P is applied to the same resonator, lower drive amplitude may be necessary to maintain linear operation. In this case, the noise floor may degrade. However, in systems that contain a PLL synthesizer for up-conversion, the far-from-carrier noise of the reference is suppressed. In such applications, resonator Q has more significance than linearity. Nonetheless, methods to further improve resonator linearity are suggested in the conclusions.

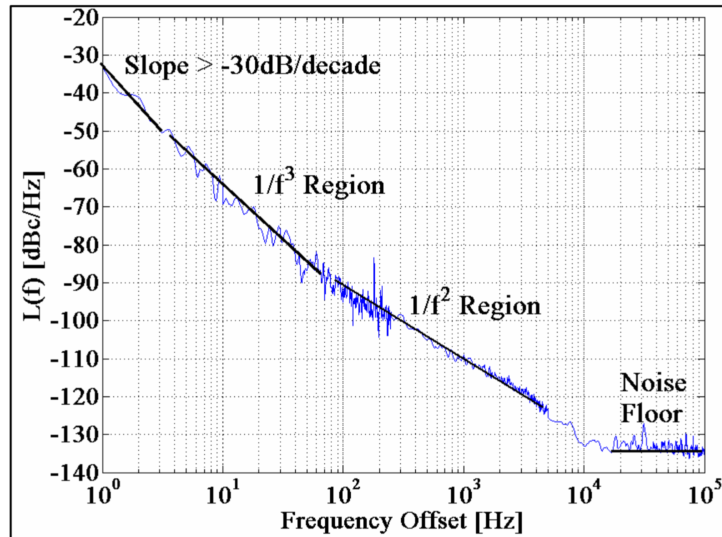

Figure 6.7 Single-sideband phase noise of the 6-MHz IBAR oscillator with a 3-V polarization voltage.

Table 6.2 Specifications of the two-chip temperature compensated IBAR oscillator.

Resonator Specifications	
Open loop quality factor 1V bias 10V bias	 112000 54000
Tuning coefficient	-7.34 ppm/V^2
Circuit Specifications	
Amplifier GBW product	175 MHz
Charge pump clock	1 MHz
Ripple filter -3dB freq.	1 kHz
Total power consumption w/ linear compensation w/ parabolic compensation	 1.8 mW 1.9 mW
Die area (for either IC)	2.25 mm^2
Oscillator Specifications	
Freq. stability over 100ºC Uncompensated w/ linear compensation w/ parabolic compensation	 2830 ppm 334 ppm 39 ppm
Phase noise performance 10Hz offset 1kHz offset Phase noise floor	 -66 dBc/Hz -112 dBc/Hz -135 dBc/Hz

CHAPTER 7 CONCLUSIONS AND DISCUSSION

The major contributions in this work are in the design and characterization of micromechanical resonators for reference oscillators. Temperature-stable oscillators at 6 and 100 MHz comprising of silicon resonators were demonstrated. Manufacturability for a micromechanical oscillator was investigated. Process compensation, the key element of the approach, was demonstrated with a 10-MHz resonator. Several resonator topologies applicable from 30 kHz to 3 GHz were identified, modeled, and characterized.

A number of conclusions can be drawn from this work. First and foremost, silicon is an excellent material for micromechanical resonators. Low impedance and high Q can be obtained in silicon resonators up to several hundred MHz. Piezoelectric transduction is advantageous for ultra-high frequencies. Large electrode area is the key design guideline for reference oscillator applications.

Many firsts were observed in this research. The 100-MHz oscillator is the highest frequency silicon-resonator oscillator. A -135 dBc/Hz noise floor was measured from the same oscillator. Temperature compensation by voltage tuning enabled 39 ppm frequency stability over 100 °C for a 6-MHz oscillator. The first micromechanical resonator (not including FBAR) with 50-Ω impedance was demonstrated. The highest f-Q product of 1×10^{13} from a silicon resonator was measured. An output current of 1.3 mA rms was measured from a piezoelectric-on-silicon resonator. Capacitive resonator impedances were reduced well below 1 kΩ and body-resistance loading of the quality factor was observed. Repeatable center frequencies and Q of 150,000 to 180,000 in low vacuum (5 torr) were measured for a DFM-optimized 10-MHz design.

7.1 Initial Frequency Accuracy

The required frequency accuracy is determined by the application. Using silicon as the substrate and considering the factors discussed in Section 2.5, ±500 ppm is a high-confidence level for a process-compensated resonator. For applications requiring ~0.1% accuracy, this approach is feasible.

The majority of applications requires 100 ppm accuracy or better. Since batch compensation can provide 1000 ppm or better repeatability, the residual inaccuracy can be trimmed using the bias voltage. To implement this in a temperature-compensated oscillator based on V_P-tuning, only 1000 ppm "tuning margin" is necessary. Thus, fractional-N PLL architectures are not necessary for temperature compensation and initial accuracy adjustment. It is predicted that low-power micromechanical oscillators will be manufactured using process compensation in combination with electrical trimming.

7.2 Future Work

In this field of micromechanical resonators, the surface is merely scratched. A few areas of research are suggested to further understand the fundamental limitations. The mechanical properties of SCS need further investigation – The effect of dopants, doping concentration, and defects on the acoustic properties, intrinsic loss, linearity limits, and long-term effects could be studied. Second, the topic of phase noise from capacitive transduction and its optimization would be interesting topics. Other beneficial research topics include the intrinsic f-Q product of silicon and other materials, temperature compensation with silicon dioxide, long-term stability of materials, and new architectures enabled by micromechanical frequency references.

More technological advances are necessary to enable low-power low-phase-noise temperature-stable reference oscillators. Further characterization to obtain optimization vectors in linearity, tuning, loaded Q, and phase noise would be very valuable. Technology will advance, and its direction will be driven by demand.

APPENDIX A. RESONATOR CHARACTERISTICS AND MODELING

A.1 Capacitive Resonator Fundamentals

Consider the capacitive resonator in Figure A.1a. The mobility of the resonator is

$$Y_{mech} = \frac{s \cdot u}{F} = \left(\frac{1}{m_n s + c_n + {k_n}/{s}} \right) \tag{A.1}$$

Electrostatic force normal to a surface is

$$F_e = \frac{\partial U}{\partial u} = \frac{1}{2} V_{i0}^{\ 2} \frac{\partial C_{ei}}{\partial u} \tag{A.2}$$

in which the voltage difference V_{i0} between the resonator and electrode i is V_P-V_{Bi}+v_{in}. V_{Bi} is the bias on electrode i and v_{in} is the excitation or "drive" voltage. Expressing the polarization between the resonator and electrode as $V_{Pi} = V_P - V_{Bi}$, F becomes

$$F_e = \frac{1}{2} \frac{\partial C_{ei}}{\partial u} \left[V_{Pi}^{\ 2} + 2 V_{Pi} v_{in} + v_{in}^{\ 2} \right] \tag{A.3}$$

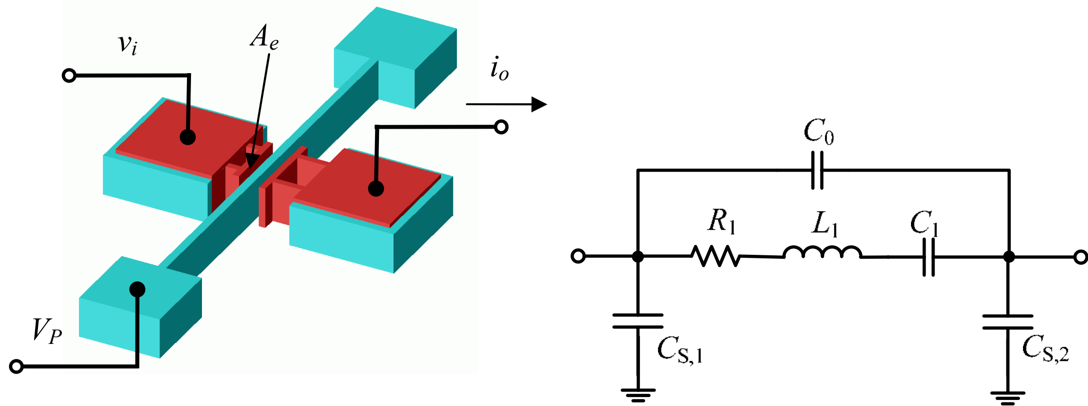

Figure A.1 Schematic of a capacitive resonator in two-port operation.

The first term in the parentheses contributes to a time-invariant force. The third term consists of a constant component and a harmonic component at twice the frequency of the applied voltage. With comparable levels of V_{Pi} and v_{in}, the resonator will be excited at twice the drive frequency. Typically $V_{Pi} >> v_{in}$, and only the second term is considered for forced vibration.

$$F_{\mathrm{e,drive}} = V_{P1} v_{in} \frac{\partial C_{e1}}{\partial u} \tag{A.4}$$

Therefore, the ratio of applied force to input voltage, which is defined as the input electromechanical coupling coefficient, is expressed as

$$\eta_1 = \frac{F_{\mathrm{e,drive}}}{v_{in}} = V_{P1} \frac{\partial C_{e1}}{\partial u}. \tag{A.5}$$

The output current from the resonator is caused by the time-varying charge on the electrode, given by,

$$I_2 = V_{P2} \frac{d}{dt} C_{e2} \tag{A.6}$$

assuming V_{P2} is held constant. The output current to velocity ratio, which is defined as the output electromechanical coupling coefficient, is expressed as

$$\eta_2 = \frac{I_2}{du/dt} = V_{P2} \frac{\partial C_{e2}}{\partial u}. \tag{A.7}$$

Considering the overall admittance of the resonator, the transfer function has the same form as the admittance of a series RLC. The electromechanical device can then be modeled by the following RLC elements:

$$R_1 = \frac{k_n}{\omega Q \eta_1 \eta_2}, L_1 = \frac{m_n}{\eta_1 \eta_2}, C_1 = \frac{\eta_1 \eta_2}{k_n} \qquad \text{(A.8,A.9,A.10)}$$

If the input and output transformers are symmetric, $\eta = \eta_1 = \eta_2$

Parallel-plate transduction, when compared to comb drives, provides improved coupling for small transduction gaps and alleviates mass loading to enable higher frequencies. The static capacitance of a parallel-plate transducer is given by

$$C = \frac{\varepsilon A_e}{d - u_y}, \tag{A.11}$$

where A_e is the area of the electrode. In (A.11), a uniform displacement u_y is assumed. Since $(1-x)^{-1} = 1 + x + x^2 + x^3 + x^4 \cdots$ holds true for $|x|<1$,

$$\left(1 - \frac{y}{d}\right)^{-1} = 1 + \frac{y}{d} + \left(\frac{y}{d}\right)^2 + \left(\frac{y}{d}\right)^3 + \left(\frac{y}{d}\right)^4 \cdots. \tag{A.12}$$

Thus, the gradient of static capacitance to displacement u_y is

$$\frac{\partial C}{\partial u_y} = \frac{\varepsilon A_e}{d^2}\left\{1 + 2\left(\frac{u_y}{d}\right) + 3\left(\frac{u_y}{d}\right)^2 + 4\left(\frac{u_y}{d}\right)^3 + \cdots\right\}. \tag{A.13}$$

The linearized capacitive electromechanical coupling coefficient simplifies to

$$\eta_i = V_{Pi}\frac{\partial C}{\partial u_y} \approx \frac{V_{Pi}\varepsilon A_e}{d^2}. \tag{A.14}$$

For increased coupling, the polarization is typically increased. Several limitations to V_P exist, including voltage generation (*i.e.*, breakdown in the interface IC), dielectric breakdown across transduction gaps, levitation, and electrostatic pull-in. The latter three phenomena are rarely observed in this work and the applicable V_P is only limited by the interface IC and linearity. The HARPSS-on-SOI process used for most of the devices in this work enables thick device for large area A_e and small gaps d.

A.2 Two-Port Capacitive Resonator

A two-port π-configuration resonator utilized as a series element typically operates in series resonance. This configuration requires three or more isolated terminals on the device (Figure A.1). Shunt capacitances between the resonator body and the input and output electrodes, $C_{S,1}$ and $C_{S,2}$, are present. The primary feature of the π-configuration is the lack of an inherent parallel capacitance C_0. A parasitic parallel capacitance exists nonetheless.

The motional resistance of the device by substituting (A.14) into (A.8) becomes

$$R_1 = \frac{k_n d^4}{\omega_n Q V_{Pi}^2 \varepsilon^2 A_e^2} . \tag{A.15}$$

The characteristic resistance of the resonator is inversely dependent on V_{Pi}^2. Since R_1 has a d^4 dependence, a small transduction gap is necessary for small R_1. Since the dynamic stiffness scales with cross-sectional area, R_1 can be rearranged to emphasize this.

$$R_1 = \left(\frac{k_n}{A_e} \right) \frac{d^4}{\omega_n Q V_{Pi}^2 \varepsilon^2 A_e} \tag{A.16}$$

Clearly, the motional resistance is inversely proportional to electrode area. The convenience in defining a normalized dynamic stiffness k_n/A_e will be evident.

A.3 Complex Capacitive Coupling

To account for 2D and 3D complex mode shapes, either the coupling coefficients or the dynamic parameters can be revised. The input and output coupling coefficients are generally defined as

$$\eta_1 = \frac{F}{v_{in}} \text{ and } \eta_2 = \frac{I_2}{sU_m} \tag{A.17, A.18}$$

where F is the modal force, v_{in} is the input voltage, I_2 is the output current, and U_m is the mechanical displacement. From these two definitions,

$$\eta = V_{i0} \frac{\partial C}{\partial u_y} \tag{A.19}$$

in which V_{i0} is the potential difference between electrode i and the resonator body, and $u_y(x,z) = U_m \cdot \hat{u}(x,z)$ is the displacement of the resonator along the electrode surface in y. The instantaneous capacitance between a uniform electrode and a resonator with a complex mode shape is

$$C = \iint \frac{\varepsilon}{d \pm u_y(x,z)} dxdz\,. \tag{A.20}$$

The input electromechanical coupling coefficient η_1 can be found from the electrostatic force. The electrostatic force on an infinitesimally small section is given by

$$dF(x,z) = \frac{1}{2} V_{10}{}^2 \frac{\varepsilon}{d^2} dxdz\,. \tag{A.21}$$

The work done, U_F, by the force is

$$U_F = F_1 \cdot u_a = \iint dF(x,z) \cdot u_y(x,z) \tag{A.22}$$

where F_1 is the modal force and u_a is the modal displacement. Thus, the modal force is

$$F_1 = \frac{1}{u_a}\frac{V_{10}{}^2\varepsilon}{2d^2}\int\int u_y(x,z)\,dxdz = \frac{\overline{u_y}}{u_a}\frac{V_{10}{}^2\varepsilon A}{2d^2} \quad \text{(A.23)}$$

in which $\overline{u_y}$ is the average displacement of the resonator along the electrode surface in y.

Since $V_{i0}=V_{Pi}+v_{in}$,

$$F_1 = \frac{\overline{u_y}}{u_a}\frac{\varepsilon A}{2d^2}\left[V_{Pi}{}^2 + 2V_{Pi}v_{in} + v_{in}{}^2\right] \quad \text{(A.24)}$$

For $V_{Pi}>>v_{in}$, and the coupling coefficient becomes

$$\eta_1 = \frac{\overline{u_y}}{u_a}\frac{V_P\varepsilon A}{d^2}. \quad \text{(A.25)}$$

This result closely resembles the coupling coefficient for a 1-DOF system.

Evaluating the output coupling coefficient

$$\eta_2 = \frac{I_2}{su_a} \quad \text{(A.26)}$$

in which the output current I_2 is given by

$$I_2 \approx V_{20}\frac{d}{dt}C_{e2} = V_{P2}\frac{du_y}{dt}\frac{\partial C_{e2}}{\partial u_y}. \quad \text{(A.27)}$$

It is assumed that the output bias is constant. The capacitance gradient is linearized to $\varepsilon A_e d^{-2}$ and the current output from an infinitesimally small element is given by

$$dI_2(x,z) \approx V_{P2}\cdot\left[su_y(x,z)\right]\cdot\left[\frac{\varepsilon}{d^2}dxdz\right]. \quad \text{(A.28)}$$

Substituting (A.28) into (A.26) and integrating,

$$\eta_2 = \frac{\overline{u_y}}{u_a}\frac{V_{P2}\varepsilon A}{d^2}. \quad \text{(A.29)}$$

By defining $u_a \equiv \overline{u_y}$, the expression for η (2.4) remains valid for complex modes.

A.4 Electrostatic Stiffness

The electrostatic force on parallel plates (A.2) is given by

$$F_e = \frac{\partial U}{\partial y} = \frac{1}{2} V^2 \frac{\partial C}{\partial y}.$$

Substituting the capacitance gradient (A.13) into (A.2), the force from electrode *i* is

$$F_{ei} = \frac{V_{i0}{}^2 \varepsilon A_e}{2d^2} \left[1 + 2\left(\frac{u}{d}\right) + 3\left(\frac{u}{d}\right)^2 + 4\left(\frac{u}{d}\right)^3 + \cdots \right] \quad \text{(A.30)}$$

in which $V_{i0}=V_P-V_{Bi}+v_{in}$. F_e contains a displacement-independent component which changes the equilibrium of the device and displacement-dependent terms. The undamped equation of motion for a resonator with two electrodes and a symmetric mode shape is

$$F_{e1} + F_{e2} = m_n{}^{'}\ddot{u} + k_n{}^{'}u \quad \text{(A.31)}$$

in which F_{e1} and F_{e2} are represented by (A.30). Substituting and rearranging,

$$F_{e1,0} + F_{e2,0} = m_n{}^{'}\ddot{u} + u\left\{ k_n{}^{'} - \frac{F_{e1,0} + F_{e2,0}}{d} \left[2 + 3\left(\frac{u}{d}\right) + 4\left(\frac{u}{d}\right)^2 + \cdots \right] \right\} \quad \text{(A.32)}$$

Assuming $V_{B1}=V_{B2}$ and $v_{in} << V_{Pi}$, the electrostatic stiffness is given by

$$k_e \approx -2\left[k_{e,0} + k_{e,1}u + k_{e,2}u^2 \right]. \quad \text{(A.33)}$$

The linear electrostatic stiffness from one electrode becomes

$$k_{ei,0} = -\frac{2F_{ei}}{d} = -\frac{V_{i0}{}^2 \varepsilon A_e}{d^3} \quad \text{(A.34)}$$

For analyzing tunability, assume $V_{Pi} \gg v_{in}$, and that the nonlinear k_e terms are negligible. The electrostatic stiffness reduces the overall stiffness of the resonator, since the electrostatic force increases as the resonator moves towards the electrode.

A.5 Characterization with a Resistive Divider Test Set

For the resistive divider configuration in Figure 2.9, expressions for the device impedance and absorbed power are found. Since transmission is measured as a ratio between port 2 and *Ref*, the transmission ratio is

$$A_V = 20\log\left|\frac{Z_L}{Z_t + Z_L}\right| \qquad \text{(A.35)}$$

in which Z_t is the impedance of the DUT. Rearranging gives

$$Z_t = Z_L\left(10^{-\frac{A_V}{20}} - 1\right). \qquad \text{(A.36)}$$

For a resonator with small C_0, the response is significantly real at the frequency of lowest impedance, and $R_t \approx Z_t$.

The linearity of the resonator in terms of absorbed power and output current are also of interest. The resistive divider test set (Figure 2.9) differs from an *s*-parameter test set. When a particular input power to the DUT is specified ($P_1 = V_1^2/50\Omega$), V_s is twice the required input voltage V_1.

$$V_s = 2\cdot\sqrt{P_1\cdot 50\Omega} \qquad \text{(A.37)}$$

At resonance, the equivalent resistance seen by the source is $R_{eq}=R_S+R_{\mathrm{Ref}}//(R_t+R_L)$, where $R_S=R_{Ref}=R_L=50\Omega$. Thus, the motional current at the resonator output I_2 is

$$I_2 = \left(\frac{V_S}{R_{eq}}\right)\frac{R_{\mathrm{Ref}}}{R_t + R_L}. \qquad \text{(A.38)}$$

Since the power absorbed in the resonator is $P_R=I_2^2R_t$, it can be shown that

$$P_R = P_1\cdot\left(\frac{50\Omega}{R_t+50\Omega}\right)\left(\frac{R_t}{R_t+50\Omega}\right)\left(\frac{R_t+100\Omega}{R_t+75\Omega}\right)^2. \qquad \text{(A.39)}$$

The product of last two terms approaches unity as R_1 increases and is negligible for R_1>200Ω. Expressing power in dB and substituting for A_V, P_R is can be simplified to

$$P_R \approx P_1 + \frac{A_V}{2} \quad [\mathrm{dB}] \tag{A.40}$$

The power absorbed and the motional current can be easily extracted from open loop characteristics and the specified input power.

A.6 Rigid-Body Resonator DFM

The classification of rigid-body resonators covers all devices with a resonating mass that vibrates as a rigid body. One application is a 32768Hz real-time clock oscillator, which also serves as a good candidate for investigating manufacturability. In low frequency structures, flexural-beam suspension is typically used. The stiffness of a beam in flexure is dependent on the beam width, w, to the third power. If beam width is defined as $w+\delta$, where δ is the process bias, the stiffness variation due to the processing bias is given by

$$\begin{aligned} \Delta k_n &= k_n' - k_n \\ &\propto \left(w+\delta\right)^3 - w^3 \end{aligned} . \quad \text{(A.41)}$$

Linearizing, $\Delta k \propto 3w^2\delta$. The fractional variation then becomes

$$\frac{\Delta k_n}{k_n} \propto \frac{3w^2\delta}{w^3} = 3\frac{\delta}{w} \quad . \quad \text{(A.42)}$$

Since beam width is critical in defining the resonator stiffness, it is the critical dimension.

For the natural frequency, $\omega=(k_n/m_n)^{1/2}$, to be insensitive to the CD variation, the fractional mass variation must equal the fractional stiffness variation. According to (A.42), the fractional mass variation must be three times the fractional CD variation.

$$\frac{\Delta M}{M} \equiv 3\frac{\delta}{w} \quad \text{(A.43)}$$

This can be easily implemented in rigid-body resonators. A grid of lines with a line-width equal to one-third of w satisfies (A.43).

A.7 Flexural Beam DFM

The objective is to determine a process-bias-insensitive flexural beam geometry that enables repeatable natural frequency. The natural frequency of a flexural beam can be solved through Rayleigh's method using its mode shape *u(x)* [62].

$$R = \omega^2 = \frac{\int_0^l EI \left\{ \frac{d^2 u}{dx^2} \right\}^2 dx}{\int_0^l \rho A(x) \{u(x)\}^2 dx} \tag{A.44}$$

In a design for manufacturability, the natural frequency remains unchanged for perturbations δ in the device dimensions. For an optimal design, the frequency sensitivity is zero.

$$\frac{\partial}{\partial \delta}\omega = \frac{1}{2\omega}\frac{\partial}{\partial \delta}\omega^2 = 0 \tag{A.45}$$

It can be shown that uniform beams do not provide sufficient features for DFM. The tapered geometry in Figure A.2 is proposed.

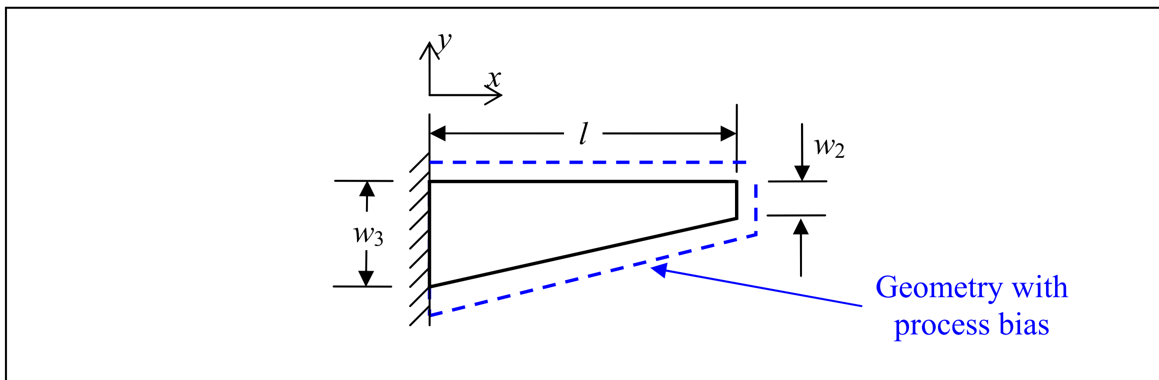

Figure A.2 Clamped-free flexural beam with a generic width-profile along the length.

The analysis continues for the clamped-free conditions. A profile in which the width varies linearly along the length is assumed.

$$w(x) = w_3 - (w_3 - w_2)\frac{x}{l}. \tag{A.46}$$

The normalized displacement of a clamped-free flexural beam can be approximated as

$$u(x) = \left(\frac{x}{l}\right)^a. \tag{A.47}$$

in which $1.4<a<2.0$ depending on the profile along the length of the beam and the proportion of flexing and shearing in the mode shape. Substituting $I=w^3t/12$ and $u(x)$ into R and simplifying,

$$\omega^2 = \frac{E\left(a^2-a\right)^2}{12\rho l^4}\frac{\left(\frac{w_3{}^3}{2a-3} - \frac{3w_3{}^2\Delta}{2a-2} + \frac{3w_3\Delta^2}{2a-1} - \frac{\Delta^3}{2a}\right)}{\frac{w_3}{2a+1} - \frac{\Delta}{2a+2}} \tag{A.48}$$

where $\Delta = w_3 - w_2$. Considering the perturbation δ, and assuming

$$\begin{aligned} w_3' &\cong w_3 + \delta \\ l' &\cong l \end{aligned} \tag{A.49}$$

the conditions for (A.45) can be solved. Simplifying,

$$\begin{aligned} &q^3\left[\frac{3(2a+1)}{2a-1} - \frac{2a+2}{2a}\right] - q^2\left[\frac{6(2a+1)}{2a-2}\right] \\ &+q\left[\frac{3(2a+2)}{2a-2} + \frac{3(2a+1)}{2a-3}\right] - \frac{2(2a+2)}{2a-3} = 0 \end{aligned} \tag{A.50}$$

where $q=\Delta/w_3$. The solutions yield a locus of values over a for which the frequency sensitivity to δ is zero. Figure A.3 represents the ratio between the width at the clamped and free ends $w_2/w_3 = 1 - q$. The solution requires that w_2 be 10–20% of w_3.

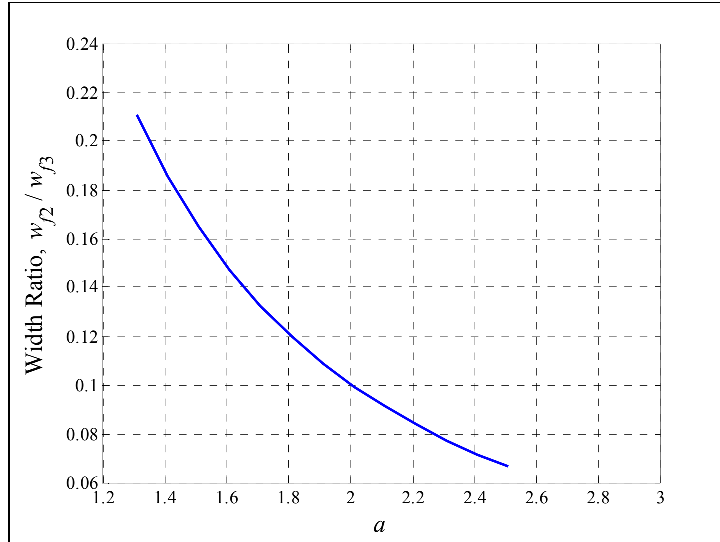

Figure A.3 The locus of w_2/w_3 that satisfies the condition of zero-sensitivity of frequency on process bias.

A.8 IBAR Modeling

A mechanical model of the IBAR is presented. The basic IBAR comprises of an extensional rod and two flexural flanges which serve as electrodes (Figure 5.1). The three categories of IBARs: the compliance-enhanced (CE), *Q*-enhanced (QE), and semi-compliant high-*Q* (CQ) design, are discussed and contrasted.

A.8.1 Lumped Mechanical Model

A simple 2-DOF system is used to analyze the resonator (Figure A.4). Symmetry is used in minimizing the model to one quarter of the geometry. The extensional rod is modeled by the mass-spring-damper system of m_r, k_r, and c_r. The flexural member is modeled with m_f, k_f, and c_f. Damping in the model is assumed to be intrinsic (*i.e.*, by material losses only, not air damping nor anchor loss) and proportional to velocity. The coupled 2-DOF system consists of the lumped parameters m_i, k_i, and c_i for i=A,B which are derived from the dynamic parameters for the constituent components. The local coordinates q_i model the local displacements of each component and v_i represent the global displacements. Clearly, there are two modes for this system. The mode of interest is always the lower frequency in-phase mode.

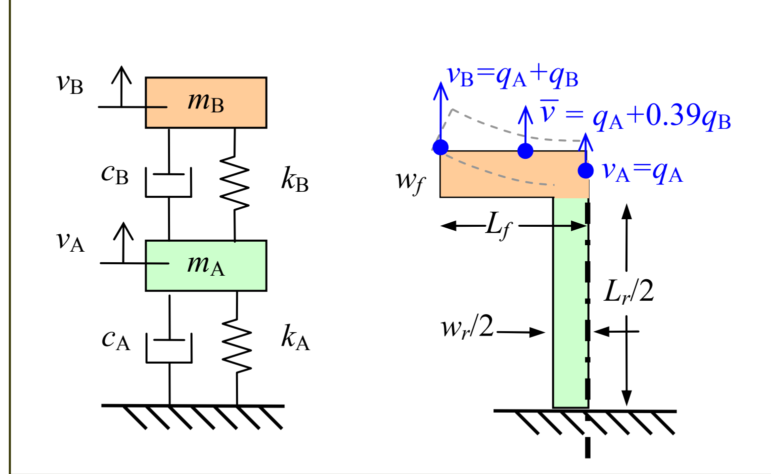

Figure A.4 Lumped 2-DOF ¼-model of the one-section IBAR.

Modeling one quarter of the rod as a clamped-free extensional component, the dynamic mass and stiffness at the free end are

$$m_r = \frac{\rho_m L_r w_r t}{8}, \quad \omega_r = \frac{n\pi v_a}{L_r}, \quad k_r = \frac{n^2\pi^2 E w_r t}{8L_r}$$

The mass and stiffness for the half-flange are modeled at the tip. Assuming the flange has only flexural contribution (*i.e.*, no shearing), its dynamic mass is

$$m_f = m_{fr} \times \rho_m L_f w_f t$$

where m_{fr}≈0.25 at the tip. Assuming the cantilever flange undergoes pure flexing,

$$\omega_f \cong \frac{w_f}{L_f^2} v_a \text{ and } k_f = \omega_f^2 \cdot m_f.$$

The system of equations that describe the IBAR in the mechanical domain are

$$\left(Ms^2 + Cs + K\right)\begin{Bmatrix} q_A \\ q_B \end{Bmatrix} = \begin{Bmatrix} F_A \\ F_B \end{Bmatrix} \tag{A.51}$$

where the mass, damping and stiffness matrices are

$$M = \begin{bmatrix} m_A & 0 \\ 0 & m_B \end{bmatrix}, \; C = \begin{bmatrix} c_A + c_B & -c_B \\ -c_B & c_B \end{bmatrix}, K = \begin{bmatrix} k_A + k_B & -k_B \\ -k_B & k_B \end{bmatrix}$$

The lumped parameters in the 2-DOF model are

$$m_B = m_f\,,\ k_B = k_f\,,\ c_B = m_f \omega_f Q_f^{-1}$$
$$m_A = m_r + \left(1 - m_{fr}\right) \rho_m L_f w_f t\,,\ k_A = k_r\,,\ c_A = m_r \omega_r Q_r^{-1}$$

Since damping in the model is assumed to be intrinsic, it is defined by the empirical $f{\cdot}Q$ product of 10^{13} for SCS (refer to Figure 3.10). The damping coefficients are expressed using the motional time constant $\tau_i = 1/(\omega_j Q_j)$ [20]. Therefore, $c_j = k_j \tau_i$ where $\tau_i \approx 16$ fs for SCS.

A.8.2 Analytic Approximations

Simple analytic approximations can be used to describe the characteristics of IBARs. Two extreme cases are considered. The stiffness can be found from

$$k_1 = \frac{2W}{\bar{v}^2} = \frac{k_A q_A{}^2 + k_B q_B{}^2}{\bar{v}^2}\,.$$

where W is the energy in the mode and $\bar{v}$ is the average displacement along the flange. Assuming the flange undergoes pure flexure,

$$\bar{v} = q_A + 0.39 q_B\,.$$

The quality factor is

$$Q_1 = \frac{2\pi W}{W_{loss}} = \frac{m_A \dot{v}_A{}^2 + m_B \dot{v}_B{}^2}{c_A \dot{q}_A q_A + c_B \dot{q}_B q_B}\,.$$

Case 1: $q_A \gg q_B$. In this case, the mode is primarily extensional and the flexural response is minimal.

$$k_1 \approx k_A\,,\ m_1 \approx m_A + m_B\,,\ Q_1 \approx \frac{\left(m_A + m_B\right)\omega_1}{c_A}$$

The quality factor is greater than the Q of the extensional member since the mass m_B acts as a lossless energy storage element. Structures having a mode that satisfies $q_A \gg q_B$ are Q-enhanced (QE) IBARs. The frequency is also loaded by m_B, however. Although Q is greater than the extensional component, the $f \cdot Q$ product remains the same.

Case 2: $q_B \gg q_A$. For this case, the flexural response is much greater than the extensional response.

$$k_1 \approx \frac{k_B}{0.39^2}, \; m_1 \approx \frac{m_B}{0.39^2}, \; Q_1 \approx \frac{m_B \omega_1}{c_B}.$$

The stiffness, Q, and natural frequency of the compliance-enhanced (CE) IBAR are solely defined by the flexural component. This occurs when $\omega_f \ll \omega_r$. It is evident from Dunkerley's equation

$$\frac{1}{\omega^2} = \sum_i \frac{1}{\omega_i^2} \tag{A.52}$$

that approximates the lowest natural frequency of a multi-degree-of-freedom system.

A.8.3 Numerical Solution

The most convenient method to solving the eigenvalue problem is through numerical means. The method of Foss [63] was used in the analysis.

$$R = \begin{bmatrix} 0_{n\times n} & M \\ M & C \end{bmatrix}, \; G = \begin{bmatrix} -M & 0_{n\times n} \\ 0_{n\times n} & K \end{bmatrix}, \; U = G^{-1} \cdot R$$

The eigen solutions for U are the complex mode shapes q and complex frequencies s. Since $s_i = \zeta_i + j\omega_i$, the Q can be found from

$$Q = \left| \frac{\omega_i}{2\varsigma_i} \right| \tag{A.53}$$

The simulated quality factor for a variety of IBARs, assuming intrinsic loss, satisfies the $f{\cdot}Q$ product condition (See Figure A.5).

In the compliance-enhanced structure, modal contribution is almost entirely from the flange. The relative compliance c_r of a resonator is defined as

$$c_r \equiv \frac{1}{k_r} \equiv \frac{\left.\left(k_n / A_e \right)_{\text{extensional}}\right|_{f_1}}{k_1 / A_e} . \tag{A.54}$$

where k_1 is the modal stiffness, A_e is the electrode area, and the normalized stiffness of the extensional mode (the numerator) is approximately 0.195 PN/m^3 per MHz. Using the numerical model, the relative compliance can be solved. The numerical c_r values are compared to the values from finite element analysis (see Figure A.6). The natural frequencies and c_r values match well for w_f= 10 μm. For w_f equal to 20 μm and 40 μm, c_r and f_n match for frequencies up to 10 MHz. At higher frequencies, shearing is present in the modes and a more elaborate model is required for accuracy. For $f_n \leq$ 10 MHz, the simple 2-DOF model is valid and accurate.

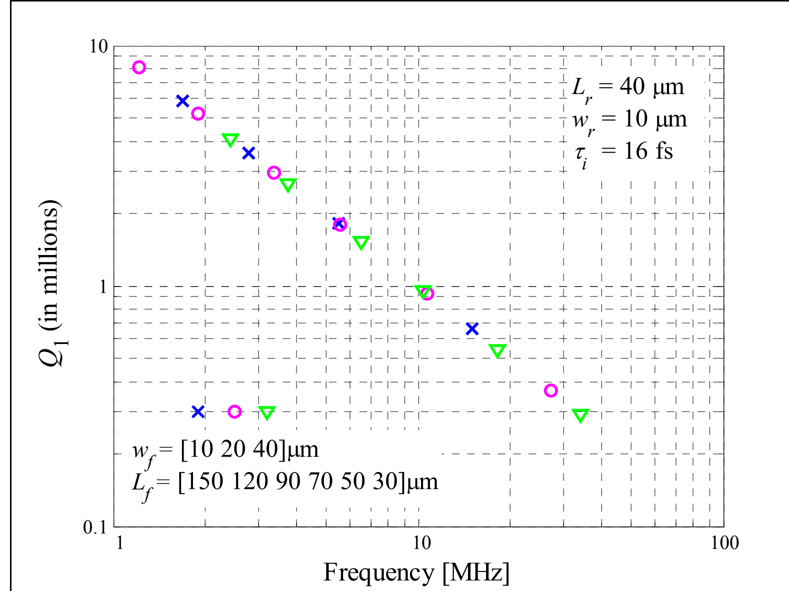

Figure A.5 Simulated Q versus frequency characteristic for IBARs with flange widths of [10,20,40] µm and flange lengths of [30,50,70,90,120,150] µm.

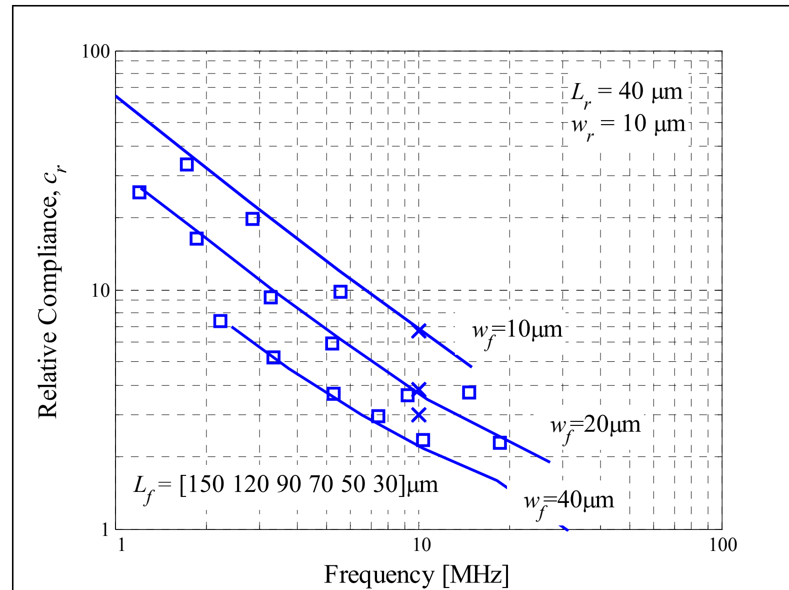

Figure A.6 Comparison between numerical results (solid line) and finite element results (□) for the relative compliance of IBARs with flange widths of [10,20,40] µm and flange lengths of [30,50,70,90,120,150] µm. Values of c_r for the DFM designs are also plotted (x).

A.9 IBAR DFM for QE and CE Designs

With the simple model and the classification of IBARs defined, the frequency variation can be addressed. The design for manufacturability for three 10-MHz resonators is presented in this section. Approximate designs are found by analytical means. Computational finite element analysis is then used for precise solutions. The characteristics of the process-compensated IBARs are summarized in Table A.1.

A.9.1 Q-Enhanced - DFM

The geometry of a QE IBAR and the dependence of its geometry on process bias is shown in Figure A.7a. Process bias is assumed to affect all features equally. Trench width CD variations result in dimensional changes of the entire structure. The effect of process bias δ on the geometry was modeled analytically and through finite element analysis (Figure A.7b). For a process-compensated design, the gradient of natural frequency on process bias is ideally zero.

Table A.1 Summary of 10-MHz process-compensated IBARs.

		CE	QE	CQ
Simulated Δf_n for δ=±0.5μm	ppm	220	25	0.6
Electrode Length, L_e	μm	129	81	139
Normalized Stiffness, k_n/A_e	PN/m^3	0.29	0.65	0.51
Relative Compliance, c_r		6.7	3.0	3.8

Using the crude 2-DOF model, the natural frequency for the first mode of a QE IBAR is

$$\omega_1 \approx \sqrt{\frac{k_A}{m_A + m_B}} \tag{A.55}$$

where

$$k_A = \frac{\pi^2 E\left(w_r + \delta\right)t}{8\left(L_r - \delta\right)},\ m_A + m_B = \rho_m t\left[\frac{\left(L_r - \delta\right)\left(w_r + \delta\right)}{8} + \left(L_f + \frac{\delta}{2}\right)\left(w_f + \delta\right)\right]$$

Assuming that $w_r = w_f$, the condition

$$\left.\frac{\partial \omega_{1,QE}}{\partial \delta} = 0\right|_{\delta=0} \tag{A.56}$$

is satisfied for $L_r/L_f = 4$. Without going into further detail, the ratio of 4 is a lower limit. If compliance of the flange is considered in the model, the ratio is greater. That is, the rod length L_r must be at least four times the half-length of the electrode.

The result is verified using finite element analysis for a 10 MHz resonator with w_r=25μm. The simulated L_f/L_r ratio is 6.1. The dimensions were obtained using the mechanical properties of SCS. The frequency variations caused by ±0.5 μm process bias were simulated to be [-25,0] ppm (Figure A.8). The FE model was meticulously meshed to ensure precision.*

* Accuracy of the model, however, requires thorough analysis on the doping- and direction-dependent material properties of silicon.

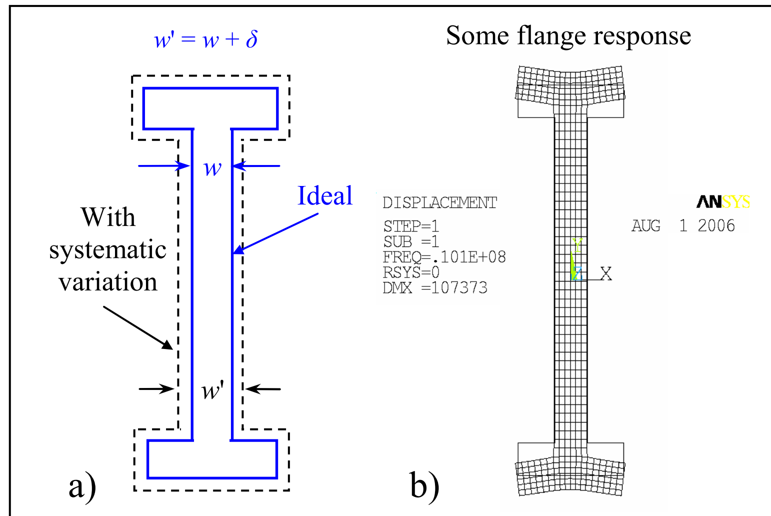

Figure A.7 a) Dimensional dependency on process bias and b) mode shape from the anisotropic finite element model of a Q-enhanced IBAR.

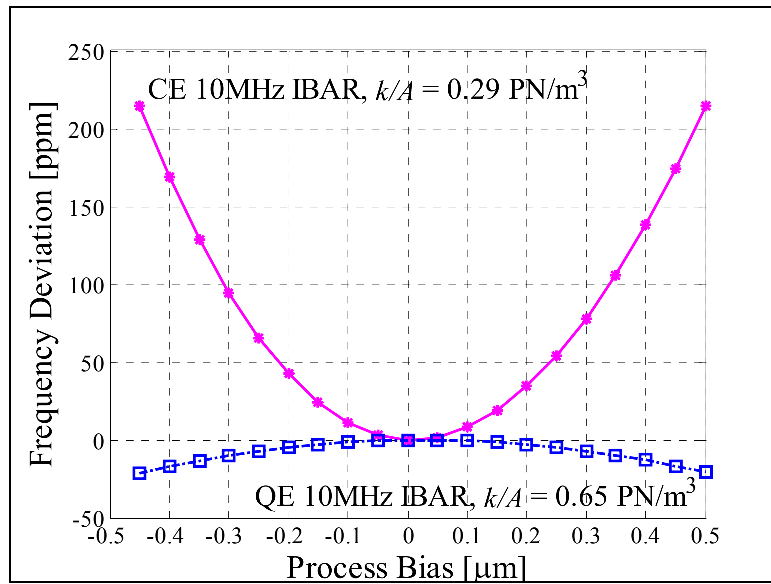

Figure A.8 Simulated f_0 variation of 10-MHz QE and CE IBARs for δ=[-0.5,0.5]µm.

A.9.2 Compliance-Enhanced – DFM

A CE IBAR has greatest contribution from the flexural component. Dunkerley's formula states that the natural frequency of the system is defined by f_1 if $f_1 << f_2$. Therefore, to compensate for processing variations in a CE IBAR, the flexural component itself must be compensated. Following Appendix A.6, tapering is necessary in a flexural beam to enable process-compensation.

A process-compensated 10-MHz CE IBAR incorporating a tapered beam is shown in Figure A.9. The variation in its natural frequency is 220 ppm for a process bias of ±0.5 μm and the curvature of the frequency sensitivity is positive (Figure A.8). The normalized stiffness is 0.29 PN/m^3. When compared to the 10-MHz QE design, the dependence of frequency on δ has increased because the flange tip (w_{f2}) is relatively small.

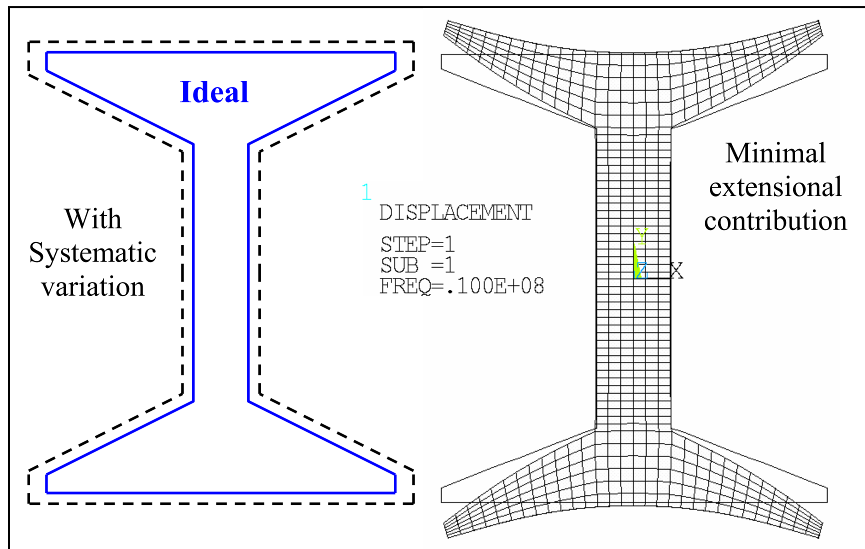

Figure A.9 a) Dimensional dependency on process bias and b) mode shape from the anisotropic finite element model of a tapered compliance-enhanced IBAR.

A.10 Electrostatic Temperature Compensation

The required electrostatic tuning coefficient γ_e and polarization voltage profile is solved in this analysis. The series resonance frequency f_s is given by

$$f_s\,(V_{Pi},T) = f_n(T) + \Delta f_e(V_{Pi}). \tag{A.57}$$

For stable f_s, electrostatic compensation requires that the shift in f_n over temperature is negated by the electrostatic tuning.

$$\Delta f_{n,T} + \Delta f_{e,\max} = 0\,. \tag{A.58}$$

The temperature-dependence of the natural frequency is expressed as

$$\frac{df_n}{dT} = f_n \cdot \gamma_T \tag{A.59}$$

The typical γ_T for a single crystal silicon resonator varies between -22 ppm/°C and -30 ppm/°C, depending of directionality, doping, and temperature. Assuming that γ_T is temperature-independent, the natural frequency is

$$f_n\left(T\right) = f_n\big|_{T=T_{ref}}\, e^{\gamma_T\left(T-T_{ref}\right)}\,. \tag{A.60}$$

A.10.1 Electrostatic Tuning Coefficient

The temperature range determines the uncompensated variation of the natural frequency.

$$\Delta f_{n,T} = f_n\left(T_{\max}\right) - f_n\left(T_{\min}\right) \tag{A.61}$$

$$\Delta f_{n,T} = f_n\big|_{T=T_{ref}} \left[e^{\gamma_T\left(T_{\max}-T_{ref}\right)} - e^{\gamma_T\left(T_{\min}-T_{ref}\right)}\right] \tag{A.62}$$

The amount of electrostatic tuning is determined by the polarization voltage range. For compensation, the lowest polarization is applied at the highest temperature, and vice versa.

$$\Delta f_{e,\max} = \Delta f_e\big|_{T=T_{\max}} - \Delta f_e\big|_{T=T_{\min}} \tag{A.63}$$

Substituting $\Delta f_e = f_n \cdot \gamma_e \cdot V_{Pi}{}^2$,

$$\Delta f_{e,\max} = f_n\left(T_{\max}\right)\gamma_e\big|_{T=T_{\max}} V_{Pi,\min}{}^2 - f_n\left(T_{\min}\right)\gamma_e\big|_{T=T_{\min}} V_{Pi,\max}{}^2 \tag{A.64}$$

Substituting for $f_n(T)$ and rearranging

$$\Delta f_{e,\max} = f_n\big|_{T=T_{ref}}\left[e^{\gamma_T\left(T_{\max}-T_{ref}\right)}\gamma_e\big|_{T=T_{\max}} V_{Pi,\min}{}^2 - e^{\gamma_T\left(T_{\min}-T_{ref}\right)}\gamma_e\big|_{T=T_{\min}} V_{Pi,\max}{}^2\right] \tag{A.65}$$

Substituting for $\Delta f_{e,\max}$ and $\Delta f_{n,T}$ into (A.58) enables a solution for γ_e. If γ_e is assumed to be constant over temperature, it can be expressed as

$$\gamma_e = \frac{\left[e^{\gamma_T\left(T_{\max}-T_{ref}\right)} - e^{\gamma_T\left(T_{\min}-T_{ref}\right)}\right]}{\left[e^{\gamma_T\left(T_{\max}-T_{ref}\right)}V_{Pi,\max}{}^2 - e^{\gamma_T\left(T_{\min}-T_{ref}\right)}V_{Pi,\min}{}^2\right]} \tag{A.66}$$

If the temperature variation is small, γ_e can be approximated by

$$\gamma_e \approx \frac{\gamma_T\left(T_{\max}-T_{\min}\right)}{\left(V_{Pi,\max}{}^2 - V_{Pi,\min}{}^2\right)}. \tag{A.67}$$

Since the γ_T and γ_e may be temperature-dependent, high-accuracy compensation schemes require a more elaborate expression for specifying γ_e. The nonlinear characteristics of the electrostatic stiffness should also be considered in applications requiring high drive-levels.

A.10.2 Polarization Voltage Profile

The V_P-profile as a function of temperature that holds f_s constant is desired. The series resonance frequency is given by

$$f_s\left(V_{Pi},T\right)=f_n\left(T\right)\left[1+\gamma_e\cdot V_{Pi}\left(T\right)^2\right] \tag{A.68}$$

Substituting for $f_n(T)$ and rearranging,

$$V_{Pi}\left(T\right)^2=\frac{1}{\gamma_e}\left(\frac{f_s}{f_n\left(T_{ref}\right)}\frac{1}{e^{\gamma_T\left(T-T_{ref}\right)}}-1\right) \tag{A.69}$$

In this case, let the reference temperature be $T_{\min}$.

$$V_{Pi}\left(T\right)^2=\frac{1}{\gamma_e}\left(\frac{f_{target}}{f_n\left(T_{\min}\right)}\frac{1}{e^{\gamma_T\left(T-T_{\min}\right)}}-1\right) \tag{A.70}$$

Since the frequency ratio is given by

$$\frac{f_s}{f_n\left(T_{\min}\right)}=1+\gamma_e\cdot V_{Pi,\max}{}^2, \tag{A.71}$$

$V_{Pi}(T)^2$ can be expressed as

$$V_{Pi}\left(T\right)^2=\frac{1}{\gamma_e}\left(\frac{1+\gamma_e\cdot V_{Pi,\max}{}^2}{e^{\gamma_T\left(T-T_{\min}\right)}}-1\right). \tag{A.72}$$

For $\gamma_T\left(T-T_{\min}\right) \ll 1$, (A.72) simplifies to

$$V_{Pi}\left(T\right)^2\approx V_{Pi,\max}{}^2-\gamma_T\left(\frac{1}{\gamma_e}+V_{Pi,\max}{}^2\right)\left(T-T_{\min}\right) \tag{A.73}$$

The expression for V_{Pi} as a function of temperature can be simplified to

$$V_{Pi}\left(T\right)^2\approx A-B\left(T-T_{\min}\right) \tag{A.74}$$

where $A\equiv V_{Pi,\max}{}^2$ and $B\equiv\gamma_T\left(\frac{1}{\gamma_e}+V_{Pi,\max}{}^2\right)$. Recall that γ_e and γ_T are both less than zero.

A.10.3 <u>*Design Center Frequency*</u>

The design natural frequency must account for the electrostatic stiffness. Since material properties are typically characterized at room temperature T_{ref}, the required design frequency at T_{ref} is solved. From (A.68),

$$f_s\left(V_{Pi},T\right)=f_n\left(T\right)\left[1+\gamma_e\cdot V_{Pi}\left(T\right)^2\right]$$

$V_{Pi,max}$ is applied at $T=T_{\min}$ and substituting for $f_n(T)$ gives

$$f_s=f_n\left(T_{ref}\right)e^{\gamma_T\left(T_{\min}-T_{ref}\right)}\left[1+\gamma_e\cdot V_{P,\max}{}^2\right]. \quad \text{(A.75)}$$

Rearranging,

$$f_n\left(T_{ref}\right)=\frac{f_s}{e^{\gamma_T\left(T_{\min}-T_{ref}\right)}\left[1+\gamma_e\cdot V_{P,\max}{}^2\right]}. \quad \text{(A.76)}$$

Using the approach for initial accuracy in Section 7.1, the tolerance on this design frequency is determined by the tuning margin. To implement tuning margin in the resonator, the specified $V_{Pi,\min}$ and $V_{Pi,\max}$ in (A.67) must be within the bounds of the voltage limits.

A.11 Piezoelectric Resonator Modeling

A.11.1 Fundamental Mode

A piezoelectric resonator can be modeled as a two-port admittance network in which the applied voltage is V_1 and output motional current is I_2 (Figure A.10). The most convenient method to finding the equivalent circuit is through the admittance.

$$Y_{21}(s,n) = \left.\frac{I_2}{V_1}\right|_{V_2=0} \tag{A.77}$$

There are three components to the admittance transfer function Y_{21}: the input transduction, the mechanical response, and the output transduction.

$$Y_{21}(s,n) = \eta_1 \cdot Y_m(s,n) \cdot \eta_2 \tag{A.78}$$

The parameters η_1 and η_2, are the input and output electro-mechanical coupling coefficients and Y_m is the mechanical mobility. In the following subsections, these three transfer functions are derived for the extensional mode along x.

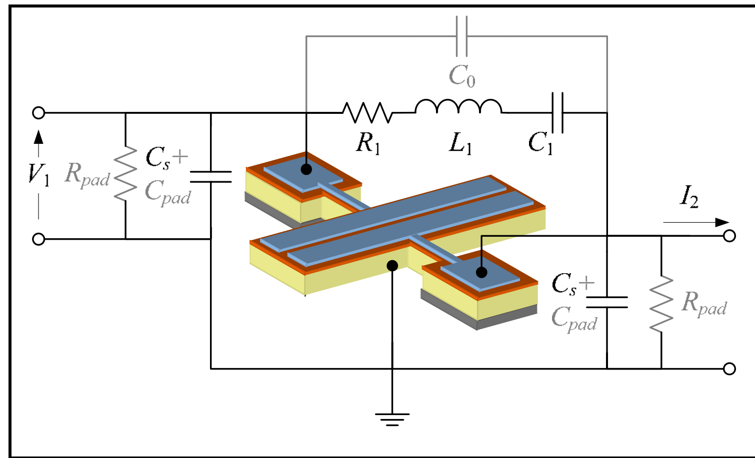

Figure A.10 Simplified model of the piezoelectric-on-silicon resonator. R_{pad}, C_{pad}, and C_0 are parasitic elements. C_s are inherent shunt capacitances.

1) Input Electromechanical Coupling: The input electromechanical coupling coefficient is defined as the ratio of induced force to input voltage.

$$\eta_1 = \frac{F_1}{V_1} \tag{A.79}$$

The modal force F_1 can be defined with respect to any point on the resonator, and x=0 is selected as the reference. The work done by the modal force is equated to the same from the surface force of the piezoelectric film to solve for F_1.

$$W = F_1 \cdot q_1 = \int_{L_{e1}} T_{\mathrm{f}} A_{\mathrm{f}} S_1(x) dx \tag{A.80}$$

In (A.47), q_1 is the modal displacement, T_{f} is the stress in the film, A_{f} is the cross sectional area of the film, and $S_1(x) = \overline{U_m} \cdot {du}/{dx}$ is the unidirectional strain. By defining the modal force at x=0, q_1 is conveniently equal to the displacement of the resonator $\overline{U_m}$ at its end.

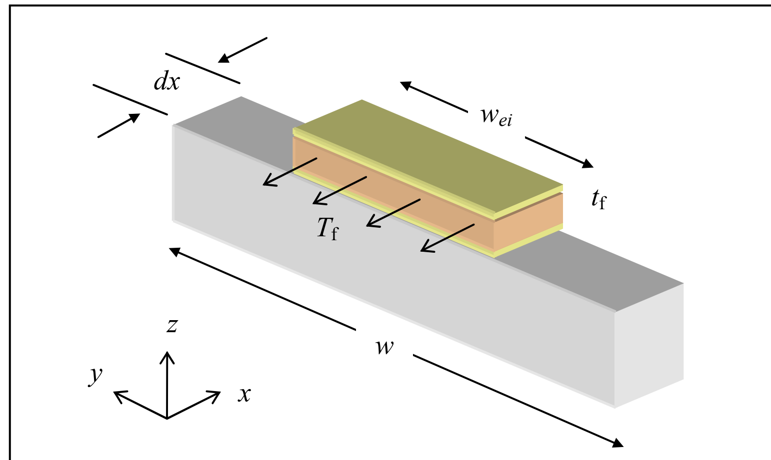

Figure A.11 Free body diagram of an infinitesimal section of the resonator perpendicular to the direction of interest.

The induced lateral stress on the film for the 1D mode is

$$T_f = T_1 = e_{31}E_3 = E_f d_{31} E_3 \tag{A.81}$$

in which E_3 is the field intensity, E_f is the elastic modulus of the film, and d_{ij} and e_{ij} are the piezoelectric strain and stress coefficients respectively. Substituting T_f and S_1 into (A.47) and rearranging for F_1 gives

$$F_1 = \frac{1}{\overline{\overline{U_m}}} \int_{L_{e1}} \left[E_f d_{31} E_3\right]\left[w_{e1} t_f\right]\left[\overline{U_m} \cdot {du}/{dx}\right] dx \tag{A.82}$$

where w_{e1} and t_f are the width of the input electrode and the thickness of the film, respectively. Simplifying and using $E_3=V_1/t_f$, F_1 simplifies to

$$F_1 = E_f d_{31} V_1 \int_{L_{e1}} w_{e1}(x) du(x) \tag{A.83}$$

For an electrode disposed over $x_1<x<x_2$, the input electromechanical coupling becomes

$$\eta_1 = d_{31} E_f w_{e1}\, u(x)\Big|_{x_1}^{x_2} \tag{A.84}$$

2) Output Electromechanical Coupling: The output coupling coefficient is the ratio of output current to velocity.

$$\eta_2 = \frac{I_2}{s\overline{\overline{U_m}}} = \frac{Q_2}{\overline{\overline{U_m}}} \tag{A.85}$$

The charge at the output Q_2 is found by integrating the induced electric displacement D_3 over the area of the output electrode. Since $d_{31}T_1=e_{3p}S_p$ for a unidirectional mode, Q_2 is expressed as

$$Q_2 = \int_{L_e}\int_{w_e} D_3 dy dx = \int_{L_e} \left(\varepsilon E_3 + d_{31} T_1\right) w_{e2}(x) dx \,. \tag{A.86}$$

E_3 at the output port is zero since V_2=0 for Y_{21}. The stress is

$$T_1(x) = E_f S_1(x) = E_f \overline{U_m} \frac{du(x)}{dx}, \tag{A.87}$$

and the electromechanical coupling at port 2 simplifies to

$$\eta_2 = d_{31} E_f w_{e2} \, u(x)\Big|_{x_1}^{x_2} \tag{A.88}$$

3) Mechanical Mobility: For a 1-DOF mechanical system, the mechanical mobility is

$$Y_m(s,n) = \frac{s\overline{U_m}}{F_1} = \left(m_n s + c_n + \frac{k_n}{s} \right)^{-1} \tag{A.89}$$

in which m_n, c_n, and k_n are the effective modal mass, damping, and stiffness, respectively. The effective mass can be found by equating the kinetic energies of the continuum and the discrete model. The stiffness and damping can then be solved using m_n, ω_n, and Q. At x=0, the mechanical parameters are given by

$$m_n = \rho_m A_x \int_L \left[u(x) \right]^2 dx = \frac{\rho_m A_x L}{2} \tag{A.90}$$

$$k_n = \omega_n^2 m_n = \frac{n^2 \pi^2 E_i A_x}{2L} \tag{A.91}$$

$$c_n = \frac{k_n}{\omega_n Q} = \frac{n\pi A_x \sqrt{E_i \rho_m}}{2Q} \tag{A.92}$$

in which $A_x \approx (t_{Si} + t_f) w$ is the area normal to x.

4) Electrical Equivalent Model: The admittance $Y_{21}(s,n)$ can now be formulated in terms of the geometry and material properties.

$$Y_{21}(s,n) = \eta_1 \cdot Y_m(s,n) \cdot \eta_2 = \frac{\eta_1 \eta_2}{m_n s + c_n + {}^{k_n}\!/_{s}} \tag{A.93}$$

This transfer function has the same form as the admittance of a series RLC, and the equivalent parameters are:

$$R_1 = \frac{c_n}{\eta_1\eta_2}, L_1 = \frac{m_n}{\eta_1\eta_2}, C_1 = \frac{\eta_1\eta_2}{k_n}. \quad \text{(A.94,A.95,A.96)}$$

The electrical equivalent model for a symmetric resonator (in which η_1=η_2) including parasitic elements is shown in Figure A.10.

5) Symmetric Half-Width Electrodes: For a resonator with symmetric electrodes (w_e=w_{e1}=w_{e2}), the input and output electromechanical coupling coefficients are equivalent. For electrodes centered at $x = L/2$ with a length of L_e bound by $(0,L)$, the following expression is obtained for the coupling coefficients when n is odd:

$$|\eta| = 2d_{31}E_f w_e \sin\left(\frac{n\pi L_e}{2L}\right) \quad \text{(A.97)}$$

Substituting into (A.94),

$$R_1 \approx \frac{n\pi\left(t_{Si}+t_f\right)\sqrt{E_i\rho_m}}{2d_{31}{}^2E_f{}^2wQ}\frac{1}{\sin^2\left(n\pi L_e/2L\right)} \quad \text{(A.98)}$$

assuming $w_e \approx w/2$. This expression is particularly interesting because R_1 is independent of frequency.

A.11.2 High-Order Modes

The multiple-electrode high-order mode is proposed for high-frequency application (Figure 4.11). In this configuration, electrode regions with equal phase are electrically connected. From (A.84), the electromechanical coupling coefficients are

$$\eta_1 \approx N_1\left(2d_{31}E_f w\right), \ \ \eta_2 \approx N_2\left(2d_{31}E_f w\right) \qquad \text{(A.99,A.100)}$$

where N_1 and N_2 are the number of electrode regions for the input and output electrodes respectively. It is assumed that electrodes cover the full width w and the majority of the area of each "section". For an odd mode number n (*i.e.*, odd number of electrodes),

$$N_1 = (n+1)/2\,, \ \ N_2 = (n-1)/2 \qquad \text{(A.101,A.102)}$$

Therefore, the product of the η_1 and η_2 is:given by

$$\eta_1\eta_2 = \left(n^2-1\right)\left(d_{31}E_f w\right)^2. \qquad \text{(A.103)}$$

Recall that η^2 for the fundamental mode is $\left(d_{31}E_f w\right)^2$. Since the dynamic mass and stiffness are also increased by a factor of n, the motional impedance is reduced by a factor of $n/(n^2\text{-}1)$. Therefore, the impedance of the high-order mode resonator is given by

$$R_1 \approx \frac{n}{n^2-1}\frac{\pi\left(t_{\text{Si}}+t_{\text{f}}\right)\sqrt{E_i\rho_m}}{2{d_{31}}^2{E_{\text{f}}}^2 wQ} \qquad \text{(A.104)}$$

for odd n. For even n, R_1 is given by

$$R_1 \approx \frac{1}{n}\frac{\pi\left(t_{\text{Si}}+t_{\text{f}}\right)\sqrt{E_i\rho_m}}{2{d_{31}}^2{E_{\text{f}}}^2 wQ}\,. \qquad \text{(A.105)}$$

APPENDIX B. SUPPORTING DATA

B.1 SiBAR Measurements

B.1.1 SiBAR Q and Impedance

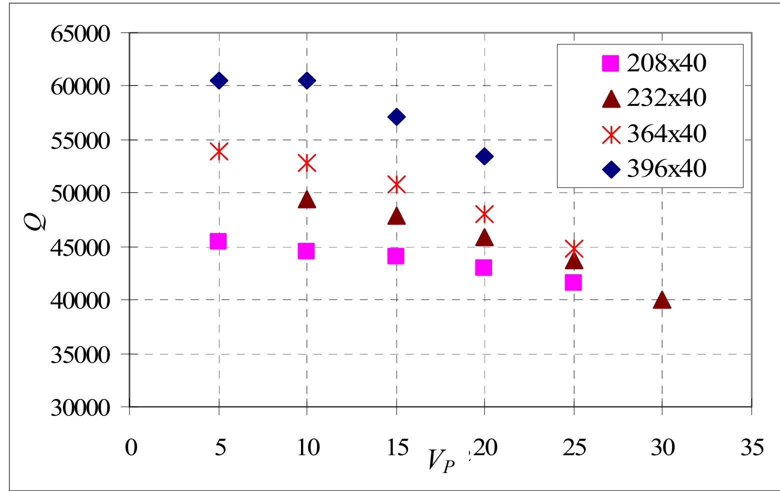

Figure B.1 Q dependence on V_P for several 100-MHz SiBARs in low vacuum.

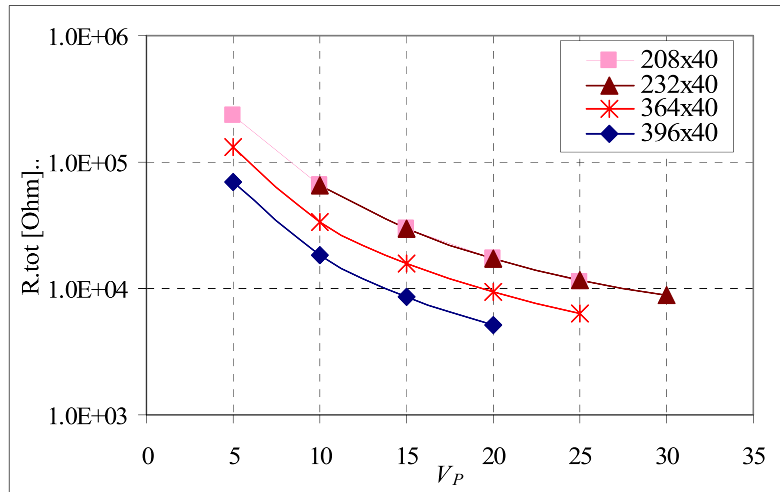

Figure B.2 Measured impedance vs. V_P and resonator width for SiBARs with 225-nm gaps.

B.1.2 SiBAR Electrostatic Tuning

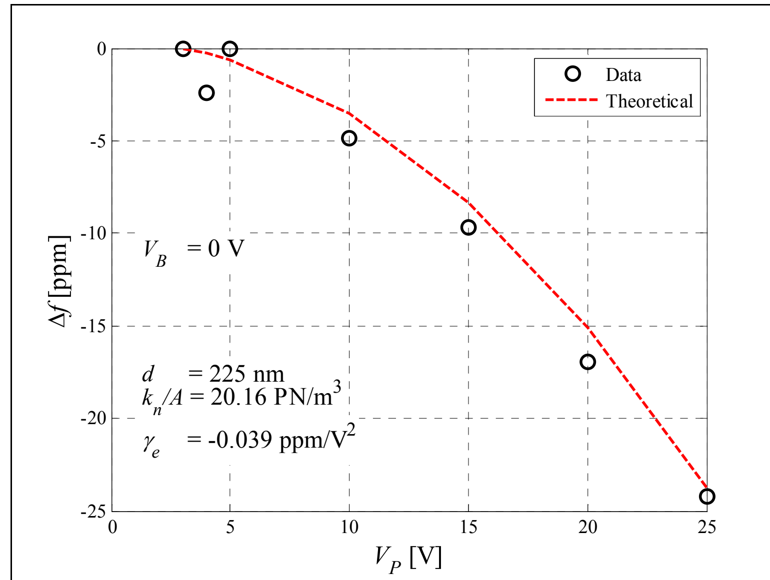

Figure B.3 Measured and theoretical tuning characteristic of the 103-MHz IBAR with 225-nm gaps over a V_P range of 3 to 25 V.

B.1.3 Frequency Tuning by Resistive Heating

Tuning of the center frequency was performed by passing current through the two anchors of a SiBAR (Figure B.4). One percent tuning was achieved with 250 mW on an unpackaged resonator in a room-temperature ambient. The power requirement is expected to be significantly lower for a packaged and thermally-isolated resonator.

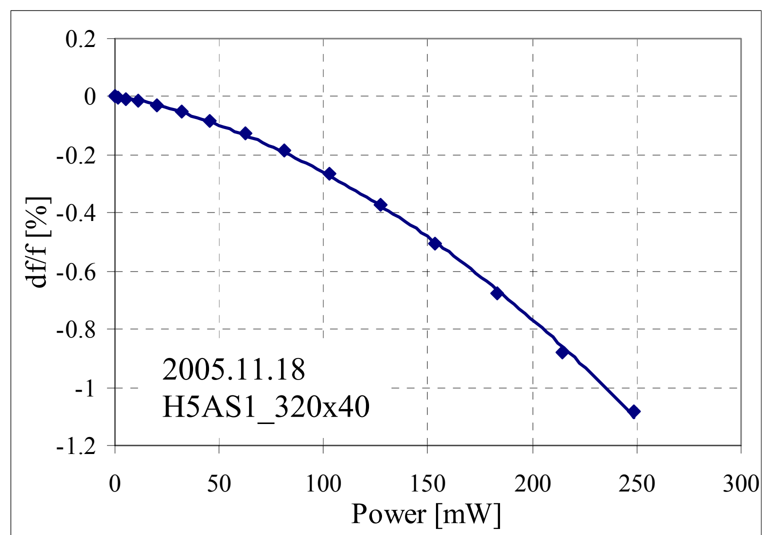

Figure B.4 Center frequency tuning by resistive heating of a SiBAR.

B.2 IBAR Measurements

B.2.1 Highest-Q and Lowest Impedance CE IBAR

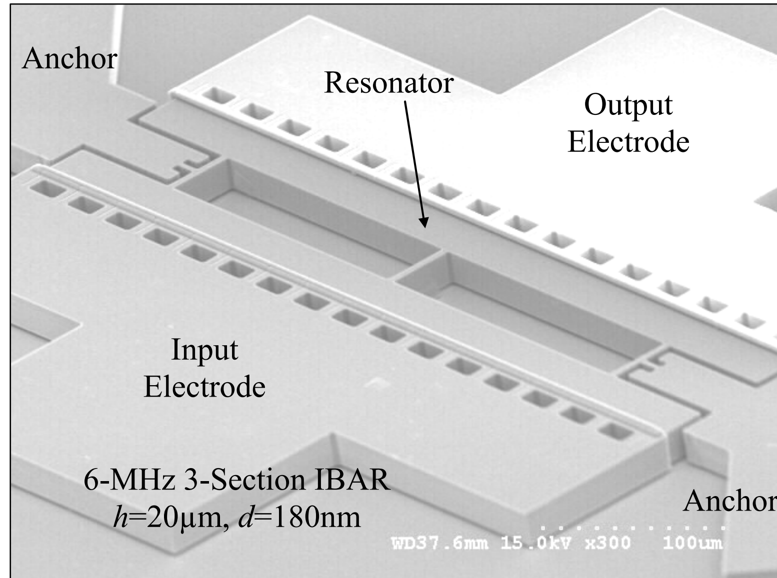

Figure B.5 SEM of a 20-µm thick HARPSS-on-SOI 6-MHz 3-section IBAR, d=180nm.

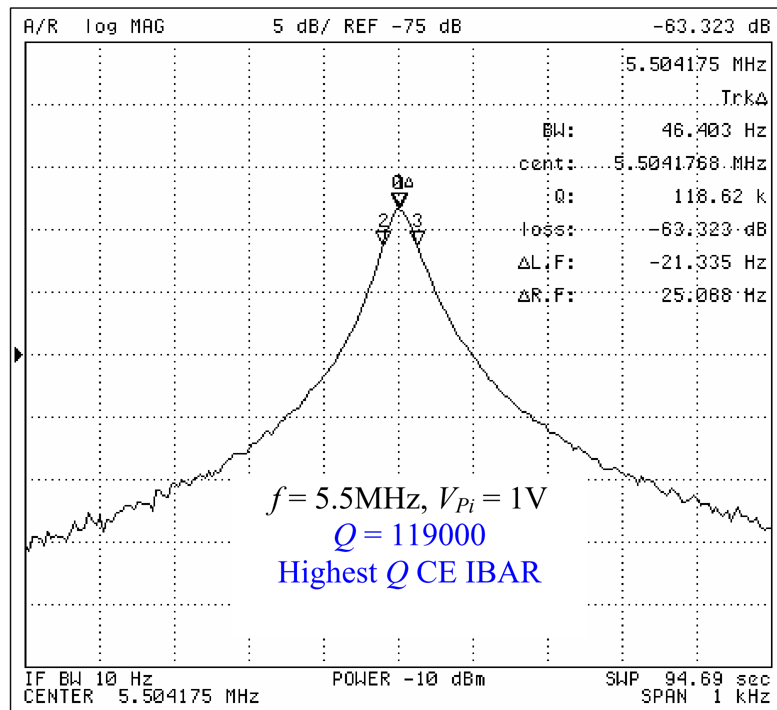

Figure B.6 Measured Q of 119000 from the 6-MHz three-section IBAR in vacuum.

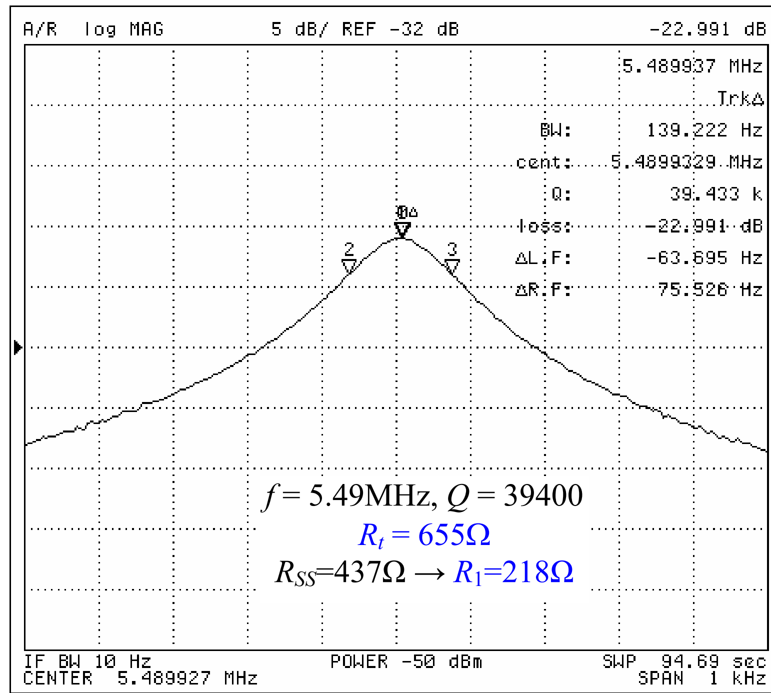

Figure B.7 Lowest measured impedance of 655 Ω (R_1=218Ω) from the 6-MHz three-section IBAR (V_{Pi}=18V).

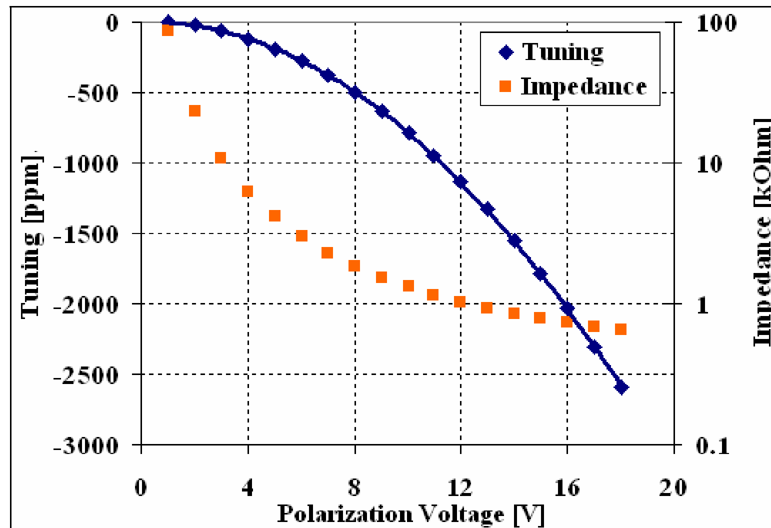

Figure B.8 Measured impedance and tuning characteristic of the 6-MHz three-section IBAR with 180-nm gaps.

B.2.2 IBAR Tuning and Q-Loading

A number of IBARs were measured for their tuning, impedance, and Q characteristics. The data reported below support the predicted parabolic tuning, the existence of R_{SS}, and the Q dependence on V_P. From Figure B.9, IBARs at 5 MHz with 270-nm gaps have approximately -4 ppm/V^2 tuning. IBARs from the same batch with 3-MHz f_s have approximately -10 ppm/V^2 tuning. From the modeling, $(k_n/A)_{\mathrm{SiBAR}}$ and c_r^{-1} are both proportional to frequency. Thus, the difference in γ_e for the 3-MHz and 5-MHz devices should be a factor of $(5/3)^2$, or 2.8, which closely matches the data.

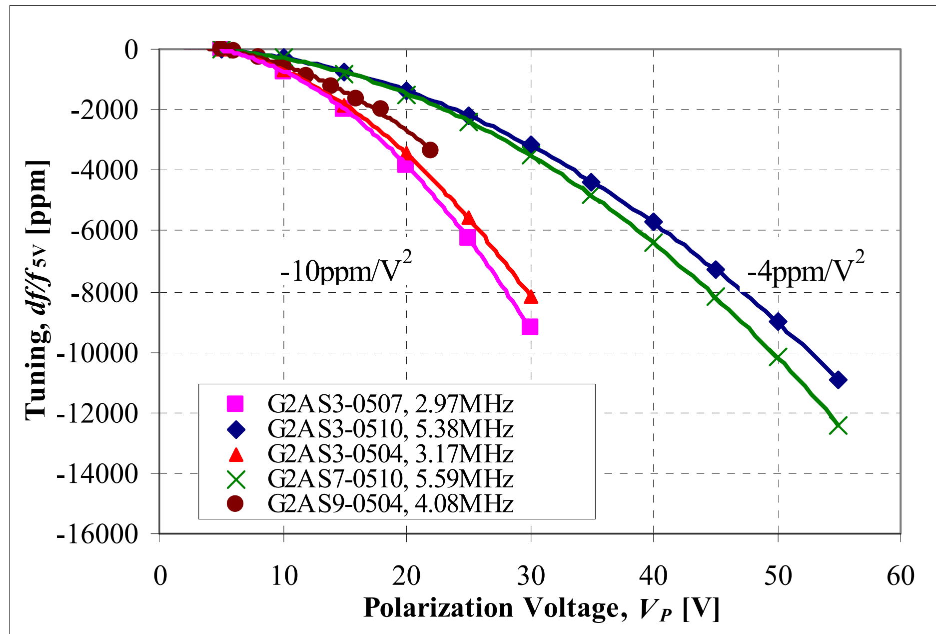

Figure B.9 Measured tuning characteristic of IBARs with 270-nm gaps.

The existence of R_{SS} is proven with more measurements. The measured impedance from several IBARs contains a constant (V_P-independent) component of 1 to 4 kΩ (Figure B.10). These R_{SS} give theoretical Q_L that match measurements (Figure B.11).

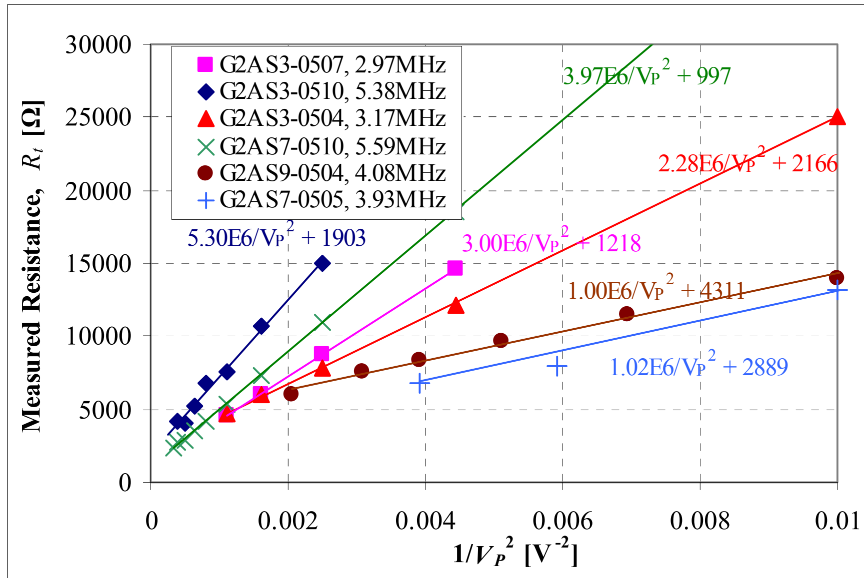

Figure B.10 Measured impedance dependence on V_P, showing existence of R_{SS} in IBARs.

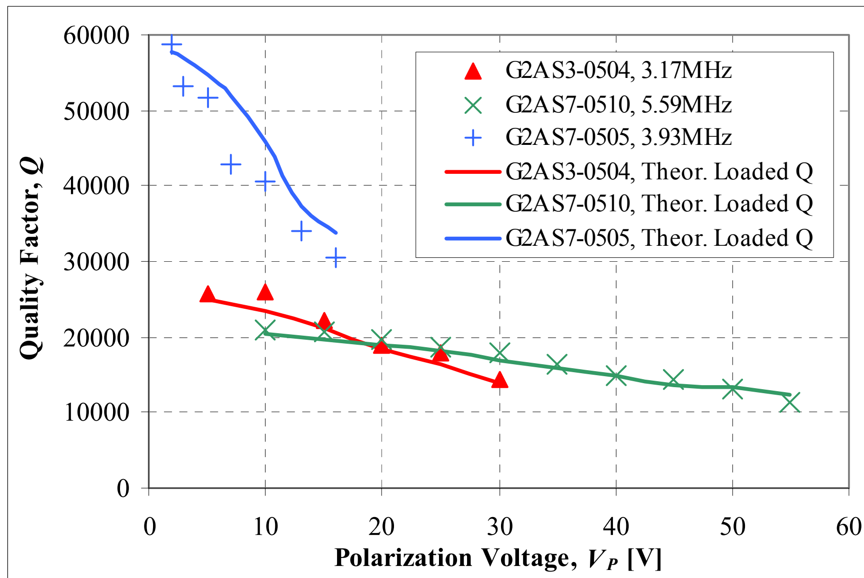

Figure B.11 Measured quality factor dependence on V_P in IBARs.

B.2.3 Highest-Tunability IBAR

IBARs with 65-nm gaps were fabricated to demonstrate low-voltage operation and high tunability. Over 3000 ppm of tuning was observed for a polarization voltage range of 2 to 4 V.

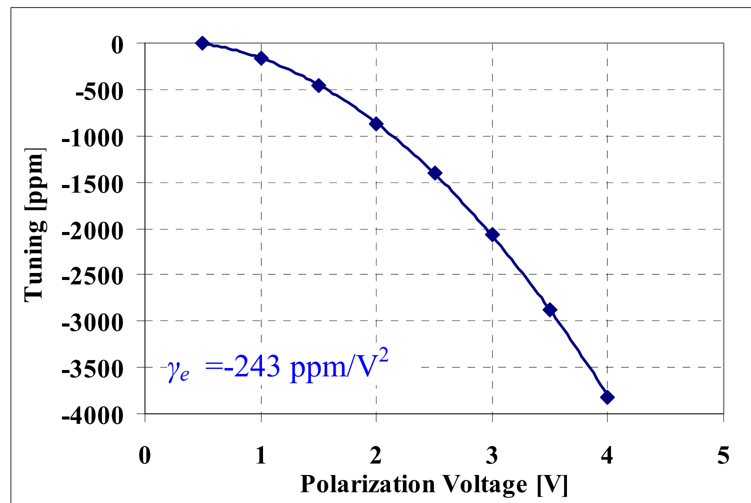

Figure B.12 Tuning characteristic of a 10-MHz IBAR with 65-nm gaps over a voltage range of 1 to 4 V.

B.2.4 <u>20-MHz IBARs</u>

IBARs with higher center frequencies were also fabricated. A 20-MHz IBAR with 65-nm gaps had a γ_e of -20.7 ppm/V^2 and sufficient tuning for temperature compensation below 15 V.

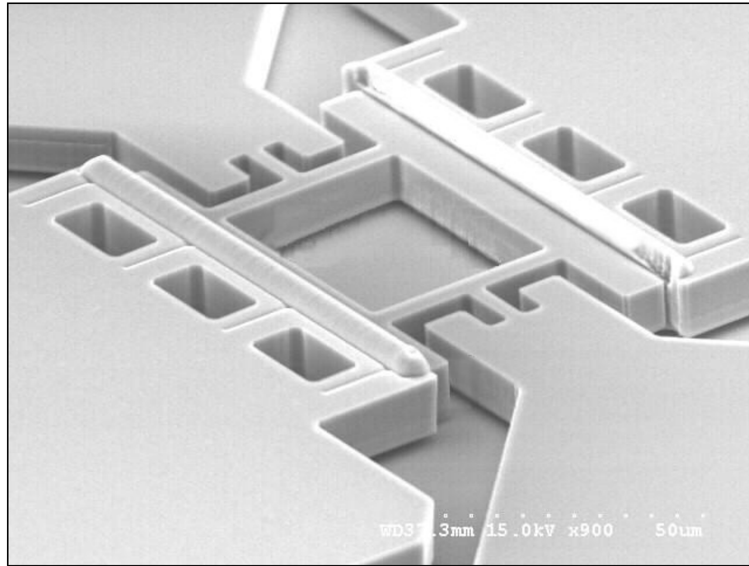

Figure B.13 SEM of a 20-MHz 10-µm-thick IBAR with 65-nm gaps.

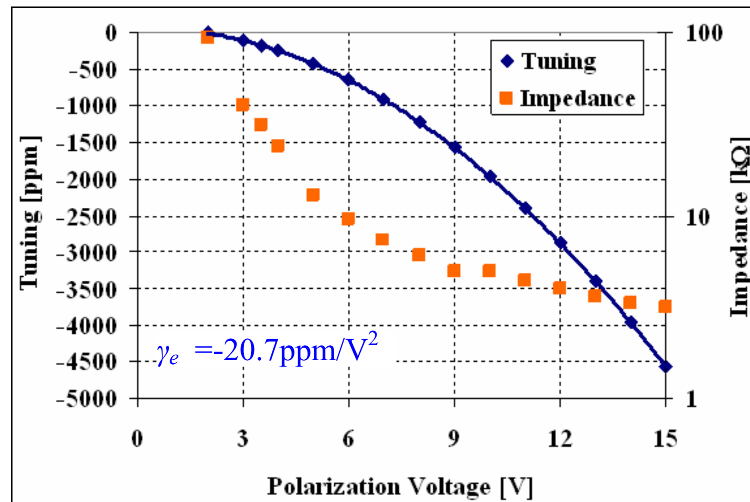

Figure B.14 Impedance and tuning of a 20-MHz IBAR with 65-nm gaps.

B.2.5 Highest-Q IBAR

The highest Q measured from a 10-MHz QE IBAR in high vacuum is 253,000 (Figure B.15).

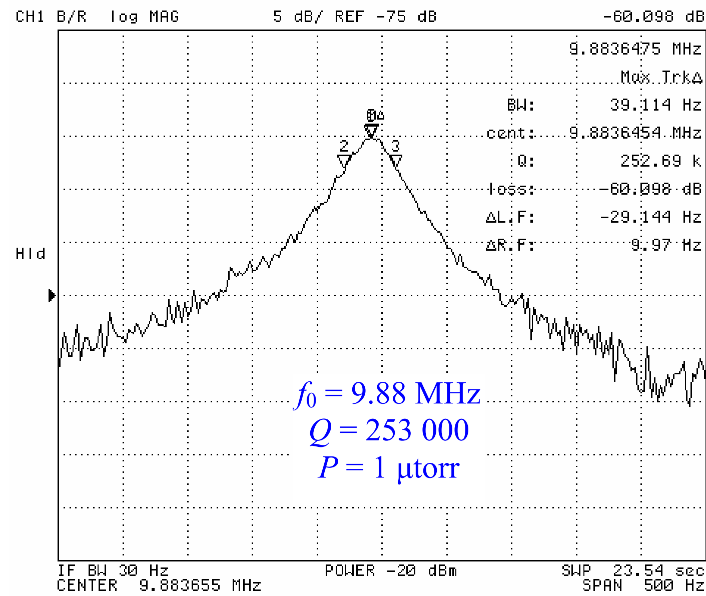

Figure B.15 Highest Q measured from a QE IBAR.

B.3 Rigid Body Resonators

Parallel-plate and comb-drive resonators for real-time clock application were designed following the DFM condition in Appendix A.6. A comb-drive resonator fabricated in 20-μm low-resistivity SOI with 1.5-μm gaps is shown in Figure B.16. The frequency response from a parallel-plate variant has a *Q* of 36000 in vacuum (Figure B.17).

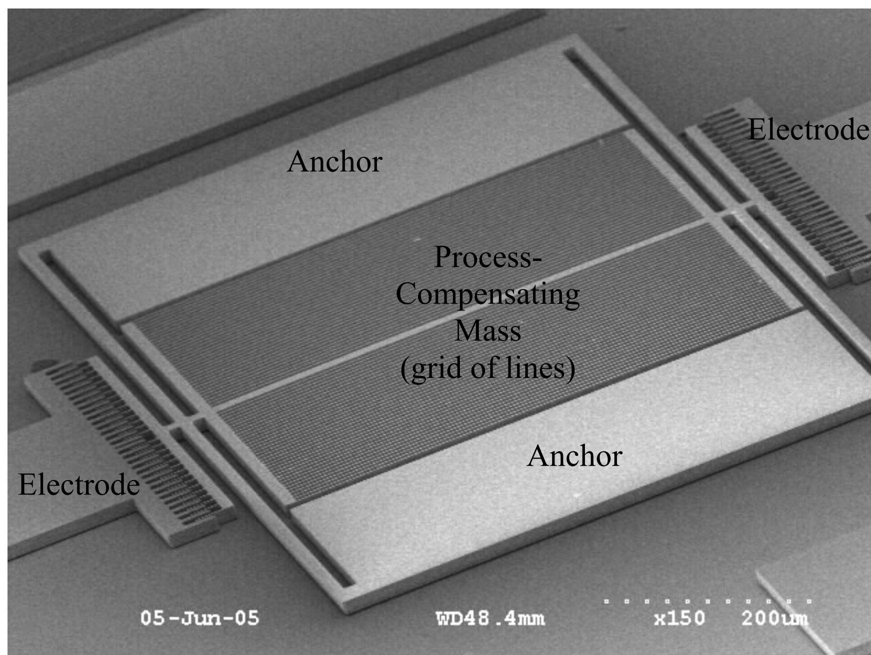

Figure B.16 SEM of an SOI rigid-body resonator designed for low-power temperature-compensated real-time clock application.

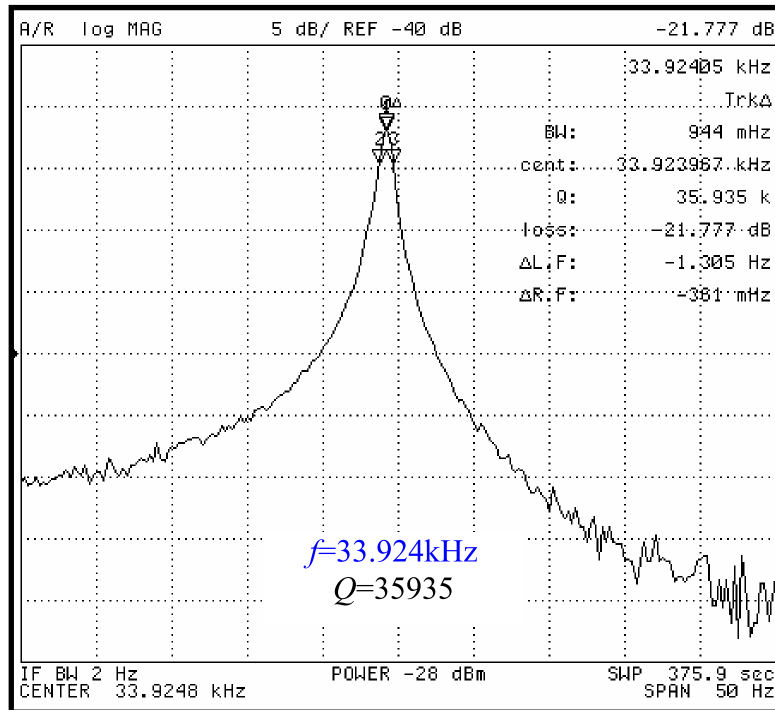

Figure B.17 Measured response from a rigid-body parallel-plate resonator in vacuum.

APPENDIX C. MATERIAL PROPERTIES

Table C.1 Properties of silicon, Al, Au, and Cr at 298K.

		Silicon (pure)	Silicon ρ_e=2e19/cm^3	Al	Au	Cr
Mass Density [kg/m^3]	ρ_m	2330		2700	19300	7200
Elastic Moduli [GPa],[52]	E_i	129.4-186.5		~62	~80	~140
	C_{11}	165.64	163.94	-	-	-
	C_{12}	63.94	64.77	-	-	-
	C_{44}	79.51	79.19	-	-	-
Poisson Ratio	ν_i	0.25-0.31		~0.3	~0.3	~0.3
Motional Time Constant [ps]	τ_i	0.016		-	-	-

Table C.2 Properties of piezoelectric films at 298K.

		ZnO [64]	PZT	AlN [65]
Mass Density, [kg/m^3]	ρ_m	5676	7600	3260
Elastic Modulus [GPa]	E_f	123	53	330
Poisson Ratio	ν_i	0.18-0.36	0.25–0.31	~0.24
Piezoelectric Strain Coefficient [pC/N]	d_{31}	-4.7	-130	-1.8 [66]
Relative Permittivity	ε_r	9–11	400–1900	8–10
Elec. Resistivity [Ω·cm]	ρ_e	10^8–10^9	10^7–10^9	10^{10}–10^{14}
Motional Time Constant [ps], Ref. [20]	τ_i	0.045	11–900	0.032

REFERENCES

[1] C. T.-C. Nguyen, "MEMS Technology for Timing and Frequency Control," *IEEE Trans. Ultrason. Ferroelectr. Freq. Control*, vol. 54, pp. 251-270, Feb. 2007.

[2] H. C. Nathanson, W. E. Newell, R. A. Wickstrom, and J. R. Davis Jr., "The resonant gate transistor," *IEEE Trans. Electron Devices*, vol. ED-14, pp. 117-133, Mar. 1967.

[3] K. Petersen, "Silicon as a mechanical material," *Proc. IEEE*, vol. 70, pp. 420-457, May 1982.

[4] R. T. Howe and R. S. Muller, "Resonant-microbridge vapor sensor," *IEEE Trans. Electron Devices*, vol. 33, pp.499-506, Apr. 1986.

[5] W. C. Tang, T.-C. H. Nguyen, and R. T. Howe, "Laterally driven polysilicon resonant microstructures," in *Proc. IEEE MEMS Conf. 1989*, Feb. 20-22 1989, pp. 53-59.

[6] C. T.-C. Nguyen and R. T. Howe, "An integrated CMOS micromechanical resonator high-*Q* oscillator," *J. Solid-State Circuits*, vol. 34, pp. 440-455, Apr. 1999.

[7] H. A. C. Tilmans and R. Legtenberg, "Electrostatically driven vacuum-encapsulated polysilicon resonators - Part II. theory and performance," *Sensors and Actuators A*, vol. 45, pp. 67-84, Oct. 1994.

[8] M. E. Frerking, *Crystal Oscillator Design and Temperature Compensation*, Van Nostrand Reinhold: New York, 1978.

[9] V. E. Bottom, *Introduction to Quartz Crystal Unit Design*, Van Nostrand Reinhold: New York, 1982.

[10] A. M. Hynes, H. Ashraf, J. K. Bhardwaj, J. Hopkins, I. Johnston, and J. N. Shepherd, "Recent advances in silicon etching for MEMS using the ASE™ process," *Sensors and Actuators A*, vol. 74, pp. 13-17, Apr. 1999.

[11] K. A. Shaw, Z. L. Zhang, and N. C. MacDonald, "SCREAM I: A single mask, single-crystal silicon, reactive etching process for microelectromechanical structures," *Sensors and Actuators A*, vol. 40, pp. 63-70, Jan. 1994.

[12] C. T.-C. Nguyen, "Micromechanical Signal Processors," Ph.D. dissertation, Dept. Electrical Engineering and Computer Sciences, University of California at Berkeley, December 1994.

[13] K. Wang, A.-C. Wong, and C. T.-C. Nguyen, "VHF free-free beam high-Q micromechanical resonators," *J. Microelectromech. Syst*, vol.9, pp. 347-360, Sep. 2000.

[14] J. R. Clark, W.-T. Hsu, and C. T.-C. Nguyen, "High-Q VHF micromechanical contour-mode disk resonators," in *Tech. Dig. IEEE Int. Electron Devices Meeting 2000 (IEDM)*, San Francisco, CA , Dec. 11-13, 2000 , pp. 493-496.

[15] F. Ayazi and K. Najafi, "High aspect ratio combined poly and single-crystal silicon (HARPSS) MEMS technology," *J. Microelectromech. Syst.*, vol. 9, pp. 288-294, Sep. 2000.

[16] D. L. DeVoe, "Piezoelectric thin film micromechanical beam resonators," *Sensors and Actuators A*, vol. 88, pp. 263-272, Jan. 2001.

[17] D. B. Leeson, "A simple model of feedback oscillator noise spectrum," *Proc. IEEE,* vol. 54, no. 2, pp. 329-330, Feb. 1966.

[18] T. H. Lee and A. Hajimiri, "Oscillator phase noise: a tutorial," *J. Solid-State Circuits*, vol. 35, pp. 326-336, Mar. 2000.

[19] E. Rubiola and V. Giordano, "On the 1/f frequency noise in ultra-stable quartz oscillators," *Trans. Ultrason. Ferroelectro. Freq. Control*, vol. 54, pp. 15-22, Jan. 2007.

[20] A. Ballato and J. G. Gualtieri, "Advances in high-Q piezoelectric resonator materials and devices," *Trans. Ultrason. Ferroelectr. Freq. Control*, vol. 41, pp. 834-844, Nov. 1994.

[21] Y. Jimbo and K. Itao, Energy loss of a cantilever vibrator, *J. Horological Institute of Japan*, vol. 47, pp. 1-15, 1968.

[22] Z. Hao, A. Erbil and F. Ayazi, "An analytical model for support loss in micromachined beam resonators," *Sensors and Actuators A*, vol. 109, pp. 156-164, Dec. 2003.

[23] D. S. Bindel, E. Quevy, T. Koyama, S. Govindjee, J. W. Demmel, and R. T. Howe, "Anchor loss simulation in resonators," in *Proc. IEEE 2005 MEMS Conf*, Miami FL, Jan. 30 – Feb. 3, 2005, pp. 133-136.

[24] C. Zener, "Internal friction in solids - part I. theory of internal friction in reeds," *Physical Review*, pp. 230-235, Aug. 1937.

[25] T. V. Roszhart, "The effect of thermoelastic internal friction on the Q of micromachined silicon resonators," in *Tech. Dig. IEEE 1990 Solid-State Sensor and Actuator Workshop*, Hilton Head Island SC, Jun. 4-7, 1990, pp. 13-16.

[26] R. Abdolvand, H. Johari, G. K. Ho, A. Erbil, and F. Ayazi, "Quality factor in trench-refilled polysilicon beam resonators," *J. Microelectromech. Syst.*, vol. 15, pp. 471-478, Jun. 2006.

[27] R. Lifshitz, and M. L. Roukes, "Thermoelastic damping in micro- and nanomechanical systems," *Physical Review B*, vol. 61, pp. 5600-5609, Feb. 2000.

[28] F. R. Blom, S. Bouwstra, M. Elwenspoek, and J. H. J. Fluitman, "Dependence of the quality factor of micromachined silicon resonators on pressure and geometry", *J. Vac. Science and Tech. B*, vol. 10 (1), pp. 19-26, Jan. 1992.

[29] J. B. Starr, "Squeeze-film damping in solid-state accelerometers," in *Tech. Dig. IEEE 1990 Solid-State Sensor and Actuator Workshop*, Hilton Head Island SC, Jun. 4-7, 1990, pp. 44-47.

[30] K. Y. Yasumura et al., "Quality factors in micron- and submicron-thick cantilevers", *J. Microelectromech Syst.*, vol. 9, pp. 117-125, Mar. 2000.

[31] J. Yan, T. Ono, and M. Esashi, "Energy dissipation in submicrometer thick single-crystal silicon cantilevers," *J. Microelectromech. Syst.*, vol. 11, pp. 775-783, Dec. 2002.

[32] R. E. Mihailovic and N.C. MacDonald, "Dissipation measurements of vacuum-operated single-crystal silicon microresonator", *Sensors and Actuators A*, vol. 50, pp. 199-207, Sep. 1995.

[33] D. W. Carr, S. Evoy, L. Sekaric, H. G. Craighead, and J. M. Parpia, "Measurement of mechanical resonance and losses in nanometer scale silicon wires," *Appl. Phys. Lett*, vol. 75, pp. 920-922, Aug. 1999.

[34] R. Hull, *Properties of Crystalline Silicon*. London: INSPEC, 1999, pp. 83.

[35] H. J. McSkimin, "Measurement of elastic constants at low temperature by means of ultrasonic waves data for silicon and germanium single crystals and for fused silica", *J. Appl. Phys.*, vol. 24, pp. 988-997, Aug. 1953.

[36] C. Bourgeouis, E. Steinsland, N. Blanc, and N. F. De Rooij, "Design of resonators for the determination of the temperature coefficients of elastic constants of moncrystalline silicon," in *Tech. Dig. 1997 IEEE Intl. Frequency Control Symp.*, Orlando FL, May 28-30, 1997, pp. 791-799.

[37] G. K. Ho, J. K.-C. Perng, and F. Ayazi, "Process compensated micromechanical resonators" in *Proc. MEMS 2007 Conf.*, Kobe Japan, Jan. 21-25, 2006, pp. 183-186.

[38] S. Pourkamali, G. K. Ho, and F. Ayazi, "Low-impedance VHF and UHF capacitive silicon bulk acoustic wave resonators—part I: concept and fabrication," *Trans. Electron Devices*, vol. 54, pp. 2017-2023, Aug. 2007.

[39] G. K. Ho, K. Sundaresan, S. Pourkamali, and F. Ayazi, "Temperature compensated IBAR reference oscillators," in *Proc. MEMS 2006 Conf.*, Istanbul Turkey, Jan. 22-26, 2006, pp. 910-913.

[40] G. K. Ho, R. Abdolvand, and F. Ayazi, "High-order composite bulk acoustic resonators," in *Proc. MEMS 2007 Conf.*, Kobe Japan, Jan. 21-25, 2006, pp. 791-794.

[41] G. K. Ho, R. Abdolvand, S. Humad, A. Sivapurapu, and F. Ayazi, "Piezoelectric-on-silicon lateral bulk acoustic wave micromechanical resonators," *J. Microelectromech. Syst.*, vol. 17, pp. 512-520, Apr. 2008.

[42] R. T. Howe, "Resonant Microsensors," in *Tech. Dig. 4th Int. Conf. on Solid-Sate Sensors and Actuators (Transducers 87)*, Tokyo, Japan, June 2-5 1987, pp. 843-848.

[43] V. Kaajakari, T. Mattila, A. Lipsanen, and A. Oja, "Nonlinear mechanical effects in silicon longitudinal mode beam resonators," *Sensors and Actuators A,* vol. 120, pp. 64-70, 2005.

[44] V. Kaajakari, T. Mattila, A. Oja, and H. Seppa, "Nonlinear limits for single-crystal silicon microresonators," *J. Microelectromech. Syst.*, vol. 13, pp. 715-724, Oct. 2004.

[45] W.-T. Hsu and A. R. Brown, "Frequency trimming for MEMS resonator oscillators," in *Tech. Dig. 2007 IEEE Frequency Control Symp*., May 29 - June 1, 2007, Geneva CH, pp. 1088-1091.

[46] M. A. Abdelmoneum, M. M. Demirci, Y.-W. Lin, and C. T.-C. Nguyen, "Location-dependent frequency tuning of vibrating micromechanical resonators via laser trimming," *in Tech. Dig. 2004 IEEE Int'l UFFC Joint 50th Anniv. Conf*, pp. 272-279.

[47] K. Wang and C. T.-C. Nguyen, "Frequency trimming and Q-factor enhancement of micromechanical resonators via localized filament annealing," in *Tech. Dig. 1997 Int'l Conf. Solid-State Sensors and Actuators (Transducers 1997)*, June 16-19, 1997, Chicago, pp. 109-112.

[48] D. Joachim and L. Lin, "Characterization of selective polysilicon deposition for MEMS resonator tuning," *J. Microelectromech. Syst.*, vol. 12, pp. 193-200, Apr. 2003.

[49] M. Lutz, *et al.*, "MEMS oscillators for high volume commercial applications," in *Tech. Dig. 14th Int'l Conf. on Solid-State Sensors, Actuators, and Microsystems, (Transducers '07)*, Lyon France, June 10-14, 2007, pp. 49-52.

[50] W.-T. Hsu, A. R. Brown, and K. R. Cioffi, "A programmable MEMS FSK transmitter," in *Tech. Dig. 2006 IEEE Int'l Solid-State Circuits Conf. (ISSCC 2006)*," San Francisco CA, Feb. 6-9, 2006, pp. 16.2.

[51] R. Abdolvand and F. Ayazi, “A gap reduction and manufacturing technique for thick oxide mask layers with multiple-size sub-μm openings,” *IEEE J. Microelectromech. Syst*, vol.15, pp. 1139-1144, Oct. 2006.

[52] J. J. Hall, “Electronic effects in the elastic constants of n-type silicon,” *Phys. Rev.*, vol. 161, pp. 756-761, Sep. 1967.

[53] J. J. Wortman and R. A. Evans, “Young’s modulus, shear modulus, and Poisson’s ratio in silicon and germanium,” *J. Appl. Phys.*, vol. 36, pp. 153-156, Jan. 1965.

[54] K. M. Lakin, J. S. Wang, and A. R. Landin, “Aluminum nitride thin film and composite bulk wave resonators,” in *Proc. 1982 Frequency Control Symp.*, Philadelphia PA, Jun. 2-4, 1982, pp. 517-524.

[55] R. Ruby and P. Merchant, “Micromachined thin film bulk acoustic resonators,” in *Proc. 1994 IEEE Int’l Freq. Control Symp*., Boston MA, Jun. 1-3, 1994, pp. 135-138.

[56] K. M. Lakin, “Thin film resonator technology,” *IEEE Trans. Ultrason. Ferroelectr. Freq. Control*, vol. 52, pp. 707-716, May 2005.

[57] S. Pourkamali, A. Hashimura, R. Abdolvand, G. Ho, A. Erbil, and F. Ayazi, "High-Q single crystal silicon HARPSS capacitive beam resonators with sub-micron transduction gaps," *J. Microelectromech. Syst.*, vol. 12, pp. 487-496, Aug. 2003.

[58] S. Humad, R. Abdolvand, G. K. Ho, G. Piazza, and F. Ayazi, “High frequency micromechanical piezo-on-silicon block resonators,” in *Tech. Dig. 2003 Int’l Electron Devices Mtg. (IEDM 2003)*, Washington DC, Dec. 8-10, 2003, pp. 39.3.1-39.3.4.

[59] S. Li, J. Li, F. Liu, M. A. Alim, and G. Chen, “The dimensional effect of breakdown field in ZnO varistors,” *J. Phys. D: Appl. Phys.*, vol. 35, pp. 1884-1888, Aug. 2002.

[60] K. Sundaresan, G. K. Ho, S. Pourkamali, and F. Ayazi, “A Low Phase Noise 100MHz Silicon BAW Reference Oscillator,” in *Proc. Custom Integrated Circuits Conf. 2006 (CICC 2006)*, San Jose CA, Sep. 10-13, 2006, pp. 841-844.

[61] K. Sundaresan, G. K. Ho, S. Pourkamali, and F. Ayazi, “Electronically temperature compensated silicon bulk acoustic resonator reference oscillators,” *J. Solid-State Circuits*, vol. 42, pp. 1425-1434, Jun. 2007.

[62] S. S. Rao, *Mechanical Vibrations 3E*, Reading, MA: Addison-Wesley, 1995, pp. 545.

[63] K. A. Foss, “Co-ordinates which uncouple the equations of motion of damped linear dynamic systems,” *J. Appl. Mech.*, vol. 25, pp. 361-364, Mar. 1958.

[64] M. J. Madou, *Fundamentals of Microfabrication 2E*, Boca Raton, FL: CRC Press, 2002, pp. 560.

[65] K. Tsubouchi, K. Sugai, and N. Mikoshiba, “AlN material constants evaluation and SAW properties on AlN/Al203 and AlN/Si,” *Proc. IEEE Ultrason. Symp.*, Chicago IL, Oct. 14-16, 1981, pp. 375-380.

[66] H. Morkoc, R. Cingolani, F. Della Sala, A. Dicarlo, P. Lugli, B. Gil, "Polarization effects in nitride semiconductor heterostructures," *Int. J. High Speed Electronics and Sys. (IJHSES)*, vol. 10, pp. 25-37, Jan. 2000.